

UCSF

UC San Francisco Electronic Theses and Dissertations

Title

Utilizing the Zebrafish Model to Investigate Asymmetric Cell Division of Radial Glia Neural Stem Cells during Forebrain Development.

Permalink

<https://escholarship.org/uc/item/90q4x671>

Author

Garcia, Jason Quirino

Publication Date

2024

Supplemental Material

<https://escholarship.org/uc/item/90q4x671#supplemental>

Peer reviewed|Thesis/dissertation

Utilizing the Zebrafish Model to Investigate Asymmetric Cell Division of Radial Glia Neural Stem Cells during Forebrain Development.

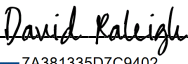
by
Jason Garcia

DISSERTATION
Submitted in partial satisfaction of the requirements for degree of
DOCTOR OF PHILOSOPHY

in
Cell Biology

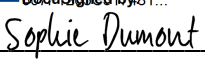
in the
GRADUATE DIVISION
of the
UNIVERSITY OF CALIFORNIA, SAN FRANCISCO

Approved:

DocuSigned by:

7A381335D7C9402... David Raleigh
Chair

DocuSigned by:

Su Guo

DocuSigned by:

8305715E0D454DC... Sophie Dumont

Committee Members

Dedicated to

Garcia family – Temo, Richard, Tracy, Justin, Hallie and Grandma Eva

White Family – Grandpa Les and Grandma Diane

Sheetrone Family – Hirrum, Joie, James, and Jack

Wacker Family – Hallie, Kayce Cruz, and Dave

Jensen Family – Sonia, William, Ying, Miles, Melissa, and Grandmother Mary

Thank you for the endless love and support.

Acknowledgements

On the path to completing my PhD, I was fortunate enough to have a support system filled with incredible individuals who supported, encouraged, and guided me. None of this would be possible without the following people:

First and foremost, I want to extend my deepest gratitude to my dissertation advisor, Dr. Su Guo. Su played a pivotal role in shaping my journey as a scientist. Her unwavering dedication to problem-solving and organizational skills greatly contributed to my ability to think critically about my thesis project. During my time under Su's guidance, I absorbed valuable lessons, such as the importance of focusing on one task at a time and seeing it through to completion, rather than spreading myself too thin. Her mentorship instilled in me a habit of scrutinizing scientific inquiries with a discerning eye. I am immensely grateful for Su's accessibility and willingness to provide input whenever I required guidance, particularly during the latter stages of my PhD. Her genuine enthusiasm for scientific exploration, coupled with her exceptional mentorship, served as a constant source of motivation, propelling me forward in my PhD journey.

I would like to thank my thesis committee: Dr. David Raleigh and Dr. Sophie Dumont, for their immense support regarding research direction, navigating PhD, and career development. Thank you for believing in me. Additionally, I'd like to thank Toni Hurley, the Tetrad program coordinator, and Dr. Kari Harrington, microscopy specialist, for all the support.

Throughout my tenure in the Guo lab, I've witnessed lab members come and go, yet one constant remains: the collaborative and encouraging atmosphere fostered by all. I am sincerely grateful to each member of the Guo lab, as I couldn't have envisioned pursuing my PhD

elsewhere. I extend special gratitude to Dr. Xiang Zhao, one of my initial mentors in the lab. He introduced me to the fascinating realm of zebrafish biology and guided me through the intricacies of conducting live imaging in developing forebrain. Additionally, I express my appreciation to Dr. Mahendra Wagle, Dr. Vincent Mouilleau, Dr. Mathieu Daynac, and Dr. Jiale Xu for their invaluable contributions and support. Moreover, grateful for my time in Dr. Dave Morgans lab and working closely with Dr. Henry Ng.

My support system was instrumental in providing me the motivation to move forward even during the most challenging of obstacles. An enormous thank you to all my family and friends in San Francisco/Bay area, Southern California Area, Laramie, Wyoming, and New York. Tracy, Richard, Temo, Hallie, Justin, Wendy, Dave, Kayce, Eva, Diane, Les, Hirrum, Joie, James, Jack, Brooke, Troy, Katie, Antonio, Rick, Elaine, Sonia, Bocchi, Bill, Ying, Miles, Mary, Melissa, Ava, Vince, Shayna, Greg, Scott, Emma, Lynn, Monica, Aleksa, Louise, Faith, Christina, Ruben, Jaretta, Mark, Lincoln, Kennedy, Chase, Jamie, Grant, Ryan, Tim, Eric, Nicole, Kevin, and Emily.

Lastly, I would never have even made it to through grad school without the love and support from my best friend, Sonia Mary Jensen. I could not have done this PhD without her. Thank you for being there with me during the ups and downs. I love you. "Till there was you".

Contributions

Some chapters contain previously published material. In some cases, this material has been altered and does not necessarily reflect its published form.

Basis for Chapter 1:

“Polarized endosome dynamics engage cytosolic Par-3 and dynein during asymmetric division”
Xiang Zhao, Jason Q. Garcia, Kai Tong, Xingye Chen, Bin Yang, Qi Li, Zhipeng Dai, Xiaoyu Shi,
Ian B. Seiple, Bo Huang, and Su Guo. *Science Advance* 2021. DOI: 10.1126/sciadv.abg1244

Basis for Chapter 2:

“Phosphorylation by Aurora Kinase A is Critical for the Cytoplasmic Presence and Cortical Asymmetry of Par-3 and Neural Progenitor Fate” Jason Q. Garcia, Vincent Mouilleau, Henry Ng, Xiang Zhao, Dave O. Morgan, and Su Guo. (2024).

Basis of Chapter 3:

“Creating Inclusive Research Laboratory Environments: Findings from the DE-SILO Intervention” Melanie Jeske, Jason Garcia, Veronica Davé, Jessleen Kanwal, D’Anne Duncan. *Science Culture* (2024).

"It's Not About Whether I Can. I Have To Do It."

-Megumi Fushiguro, Jujutsu Kaisen

"You Have No Choice But To Go on Living."

-Tanjiro Kamado, Demon slayer

"Set Your Heart Ablaze"

-Kyojuro Rengok, Demon Slayer

"Failing doesn't give you a reason to give up, as long as you believe."

- Naruto Uzumaki, Naurto Shippuden

Utilizing the Zebrafish Model to Investigate Asymmetric Cell Division of Radial Glia Neural Stem Cells during Forebrain Development.

Jason Quirino Garcia

ABSTRACT

In the developing vertebrate brain, Radial Glia Progenitor (RGP), the principal neural stem cells, undergo symmetric and asymmetric cell division (ACD), giving rise to both RGPs (self-renewal) and differentiated cell types (e.g., neurons, oligodendrocytes, and astrocytes) that will ultimately form the central nervous system. Perturbations of RGP divisions will result in neurodevelopmental disorders and brain tumors. Understanding the basic biology of RGP divisions will potentially have a significant impact on understanding brain development and may provide insights into treatments for developmental disorders or brain tumors.

During ACD, the mother cell must establish the proper axis of polarity with respect to asymmetrically localized cell fate determinants. These processes are regulated by the evolutionarily conserved Partition defective protein (Par) complexes. The Par complexes have been extensively characterized in invertebrates, but much remains to be understood in vertebrates, especially in the context of RGP ACD.

Previous studies in invertebrates and vertebrates have demonstrated that Par-3 is essential for regulating ACD by localizing asymmetrically along the division axis. Par-3 has long been thought to function exclusively at the cell cortex. Recent findings have led us to investigate the role of Par-3 during ACD in RGPs. Therefore, one approach to gain insights into this question is the utilization of zebrafish (*Danio rerio*), a powerful model organism used in biological research. Proteins of interest can be easily targeted by both pharmacological agents and genetic alterations within zebrafish, allowing for examination of complex phenotypes

resulting from desired perturbations. Unlike mammalian models, development is relatively fast, and breeding produces a large amount of progeny, allowing for quick generation progression and large sample sizes. Also, unlike mammals, development occurs externally, and the brain is transparent, allowing for accessible and clear visualization of neurodevelopment, neuronal activity, and fluorescent markers of interest throughout the whole brain. These attributes make zebrafish an excellent model for studying the *in vivo* the process of RGP's undergoing ACD in the developing forebrain. In this dissertation, we explore how polarity plays a role during ACD in RGP's.

In Chapter 1, we delve into Par-3's role in regulating polarity along the cell cortex in RGP's, influencing Notch activity in daughter cell nuclei. We explore techniques, such as the antibody uptake assay and *in vivo* time-lapse imaging in zebrafish, revealing the dynamics of internalized Notch ligand DeltaD during RGP ACD. Our findings uncover the role of cytoplasmic Par-3 in localizing intracellular determinants.

Next, in Chapter 2, we delve deeper into the role of Par-3 during active neurogenesis, particularly in ACD in RGP's. Using various techniques including *in vivo* time-lapse imaging, biochemical assays, and pharmacological studies, we investigate the interplay between cortical and cytoplasmic Par-3. Our focus is on understanding how Aurora Kinase A (AurkA) phosphorylation of Par-3 influences ACD in RGP's. Our findings highlight AurkA's role in regulating Par-3 dynamics between the cytoplasm and cortex during mitotic RGP's, ultimately impacting neural progenitor fate.

In chapter 3, we pivot away from lab bench research and discuss a diversity, equity, and inclusion (DEI) project, DE-SILO (Diversity, Equity, and Sociology training in Laboratory Organizations), that I worked on with Dr. Melaine Jeske. We designed a course module that was tailored for laboratory meetings at academic institutions. Our aim was to intersect DEI topics and facilitate discussions in the context of lab meetings. Therefore, by designing core

curriculum modules and community building modules, it would assist our “facilitators” (individuals tasked with leading DE-SILO modules at respective institutions) in leading discussions within in their lab. We piloted our project at four universities: UCSF, CalTech, University of Washington, and University of Washington, Saint Louis.

In conclusion, this dissertation sheds light on the intricate processes of RGP during ACD in the developing vertebrate brain. By elucidating the role of Par-3 in regulating polarity and Notch activity during ACD, we contribute to a deeper understanding of regulation of cell polarity. Our findings underscore the significance of proper RGP divisions for normal brain development and highlight the potential implications for addressing neurodevelopmental disorders and brain tumors. Through our investigations using zebrafish as a model organism, we uncover novel insights into the dynamic interplay between cortical and cytoplasmic Par-3 localization, orchestrated by AurkA-mediated phosphorylation. This regulatory mechanism governs the fate of neural progenitors, offering new avenues for therapeutic exploration. Furthermore, our commitment to DEI is evident in our DE-SILO project, which aims to foster inclusive environments within academic laboratory settings. By integrating DEI principles into laboratory meetings, we promote meaningful discussions and cultivate a more equitable scientific community. In essence, this dissertation not only advances our understanding of fundamental neurobiological processes but also underscores the importance of inclusivity in scientific research and academia.

Table of Contents

CHAPTER 1: Polarized endosome dynamics engage cytoplasmic Par-3 that recruits

dynein during asymmetric cell division	1
1.1 ABSTRACT	2
1.2 INTRODUCTION	2
1.3 RESULTS	4
1.3.1 <i>in vivo time-lapse imaging reveals polarized dynamics of notch ligand-containing endosomes in horizontally dividing RGPs</i>	4
1.3.2 <i>notch ligand-containing endosomes preferentially segregate to the posterior (subsequently basal) notchhi daughter</i>	6
1.3.3 <i>Par-3 and dynein are essential for polarized dynamics of dld endosome.....</i>	8
1.3.4 <i>Par-3 and Dld endosomes are preferentially co-segregated to the posterior daughter following RGP division</i>	11
1.3.5 <i>Cytoplasmic Par-3 decorates Dld endosomes and is required to recruit Dlic1</i>	13
1.4 DISCUSSION.....	15
1.5 MATERIALS and METHODS.....	17
1.5.1 <i>Experimental Design.....</i>	17
1.5.2 <i>Zebrafish strains and maintenance.....</i>	17
1.5.3 <i>Morpholinos</i>	17
1.5.4 <i>Pharmacology.....</i>	18
1.5.5. <i>DNA plasmids and complementary DNA preparation.....</i>	18
1.5.6. <i>mRNA synthesis and microinjections.....</i>	19
1.5.7. <i>Anti-Dld antibody uptake assay</i>	19
1.5.8. <i>Brain ventricle-targeted electroporation of plasmid DNAs</i>	20
1.5.9. <i>Antibodies, western blotting, and immunocytochemistry</i>	21
1.5.10. <i>Time-lapse in vivo imaging</i>	23

1.5.11. Label retention expansion microscopy.....	24
1.5.12. Image analyses.....	25
1.5.14. Measurement of asymmetry index.....	27
1.5.15. Colocalization.....	28
1.6 ACKNOWLEDGMENTS	29
1.7 FIGURES	30
1.8 SUPPLEMENTAL MATERIALS.....	39
1.9 REFERENCES	52
CHAPTER 2: Phosphorylation by Aurora Kinase A Facilitates the Cortical-Cytoplasmic	
Dynamics of Par-3 in Asymmetric Division of Radial Glia Progenitors	63
2.1 ABSTRACT.....	64
2.2 INTRODUCTION	64
2.3 RESULTS	67
2.3.1 <i>In vivo time-lapse imaging detects the cytoplasmic Par-3 in mitotic RGP.</i>	67
2.3.2 <i>Systemic expression of Par-3^{S954A} dominantly interferes with embryonic brain development.</i> .	68
2.3.3 <i>Sparsely expressed Par-3^{S954A} displays decreased cytoplasmic presence in mitotic RGPs.</i> ...	69
2.3.4 <i>Sparsely expressed Par-3^{S954A} is defective in anteroposterior cortical asymmetry, and dominantly interferes with Dld endosome formation and polarized dynamics in mitotic RGPs.</i>	70
2.3.5 <i>Systemic expression of Par-3^{S954A} dominantly interferes with progenitor-neuron fate specification in the developing forebrain.</i>	70
2.3.6 <i>Aurora Kinase A phosphorylates Par-3 at Ser-954 in vitro</i>	71
2.3.7 <i>In vivo time-lapse imaging reveals a transient interaction between AurkA and cortical Par-3 that biases the directionality of Par-3 cortical asymmetry in mitotic RGPs.</i>	72
2.3.8 <i>Inhibition of AurkA activity disrupts cell cycle progression in mitotic RGPs.</i>	73
2.3.9 <i>Over-expression of Aurora Kinase A increases cytoplasmic Par-3 presence and disrupts Par-3 cortical asymmetry</i>	73
2.4 DISCUSSION.....	75

2.6 MATERIALS AND METHODS	77
2.6.1 <i>Experimental design</i>	77
2.6.2 <i>Zebrafish strains and maintenance</i>	77
2.6.3 <i>Morpholinos</i>	78
2.6.4 <i>DNA plasmids and complementary DNA preparation</i>	78
2.6.5 <i>mRNA synthesis and microinjection</i>	79
2.6.6 <i>Anti-Dld antibody uptake assay</i>	79
2.6.7 <i>Pharmacology</i>	80
2.6.8 <i>Antibodies, Western blotting, and immunocytochemistry</i>	80
2.6.9 <i>In vitro–translated proteins and In vitro Immunoprecipitation</i>	81
2.6.10 <i>In vitro–translated proteins and In vitro Immunoprecipitation</i>	81
2.6.11 <i>In Vitro Kinase Assay</i>	82
2.6.12 <i>Time-lapse in vivo imaging</i>	82
2.6.13 <i>Image analyses</i>	83
2.6.14 <i>Quantification and statistical analysis</i>	83
2.6.15 <i>Measurement of asymmetry index</i>	84
2.7 ACKNOWLEDGEMENTS	85
2.8 FIGURES	86
2.9 SUPPLEMENTAL FIGURES	99
2.8 REFERENCES	107

CHAPTER 3: Creating Inclusive Research Laboratory Environments: Findings from the DE-SILO Intervention.....	114
3.1 INTRODUCTION	115
3.2 THE DE-SILO PROJECT: MATERIALS AND METHODS.....	118
3.3 IMPLEMENTATION SETTING	120
3.4 LESSONS LEARNED THROUGH IMPLEMENTATION.....	121
3.4.1 <i>Lab leadership shapes the environment and sets the tone.</i>	121

3.4.2 Routine engagement is key for sustained practice	124
3.3.3 Meaningful equity and inclusion requires, equitably distributed labor.....	125
3.4 CONCLUDING REMARKS AND FUTURE CONSIDERATIONS	128
3.5 TABLES	130
3.6 REFERENCES	133
CHAPTER 4: Conclusions, Perspectives, and Future Directions	136
4.1 CONCLUSIONS, PERSPECTIVES, AND FUTURE DIRECTIONS.....	137

List of Figures

Figure 1.1 Measurement of asymmetry index.	27
Figure 1.2 Polarized dynamics of notch ligand-containing endosome during RGP division.	30
Figure 1.3 Dld endosomes are preferentially segregated into the Notch ^{hi} daughter following RGP division.	32
Figure 1.4 Dld endosome asymmetry is dependent on Par-3 and the dynein motor-machinery.	34
Figure 1.5 Preferential segregation of Par-3 and internalized Dld to the posterior daughter following horizontal RGP division.	35
Figure 1.6 Cytosolic Par-3 together with Dlic1 decorates Dld endosomes.	37
Figure S1.1 In vivo antibody uptake assay labels endocytosed notch ligand Dld without affecting cell division patterns and embryonic development.	40
Figure S1.2 In vivo time-lapse sequences of images show the dynamics of Dld endosomes in 6 additional mitotic RGPs.	42
Figure S1.3 Spatial distributions of imaged telophase RGPs in the embryonic forebrain.	43
Figure S1.4 Mib and Dld endosomes preferentially segregate into different daughter cells in 3 additional mitotic RGPs.	44
Figure S1.5 An Example of Paired Daughter Cell with Symmetric Dld and Her4.1-RFP Dynamics.	45
Figure S1.6 Rescue of Par-3 and Dlic1 Morphant Phenotypes by Par-3-GFP and Dlic1 mRNAs Respectively.	46
Figure S1.7 The Dlic1 Isoform is expressed in mitotic RGPs and can be effectively knocked down using morpholinos antisense oligonucleotides.	48
Figure S1.8 Validation of Anti-Par-3 Antibody and Immunofluorescence Labeling (IF).	50
Figure S1.9 Endogenous Par-3 and Dlic1 Associate with Dld Endosomes in mitotic RGPs.	51

Figure 2.1 Measurement of asymmetry index.	84
Figure 2.2 In vivo time lapse Imaging reveals cytoplasmic Par-3 in mitotic RGPs.	86
Figure 2.3 Par-3 ^{Ser954} Phospho-Incapable mutant reveals a dominate negative affect during brain development and cytoplasmic Par-3 localization in RGPs.	88
Figure 2.4 Par-3 Phospho-Incapable mutants demonstrate a disruption of Par-3 and Dld asymmetry during RGPs ACD.	90
Figure 2.5 Par-3 ^{S954A} dominantly interferes with progenitor cell fate during..... active neurogenesis.	92
Figure 2.6 Aurora Kinase A directly phosphorylates Par-3 at Ser-954.	94
Figure 2.7 In vivo time lapse Imaging reveals cytoplasmic Par-3 in mitotic RGPs.	95
Figure 2.8 Over-expression of AurkA result an increase of Cytoplasmic Par-3 during RGPs ACD.	97
Figure S2.1 Phenotypic scoring rubric and time lapse images of Par-3 phospho-incapable mutants.	99
Figure S2.2 Schematic of Calculating Relative Cytoplasmic-Cortical Par-3 expression during RGPs ACD.	101
Figure S2.3 Par-3 Morphant results in reduction of Dld Expression.	102
Figure S2.4 Aurora Kinase A directly phosphorylates Par3 at Ser-954.	103
Figure S2.5 In vivo time-lapse imaging reveal AurkA in mitotic RGPs.	104
Figure S2.6 1uM inhibition of AurkA during RGP ACD prevents cell cycle progression.....	105
Figure S2.7 Normalization and validation of Over-expression of AurkA.	106

List of Tables

Table 3.5.1 Modules	130
Table 3.5.2 Lab Characteristics	131

CHAPTER 1: Polarized endosome dynamics engage cytoplasmic Par-3 that recruits dynein during asymmetric cell division

1.1 ABSTRACT

In the developing embryos, the cortical polarity regulator Par-3 is critical for establishing Notch signaling asymmetry between daughter cells during asymmetric cell division (ACD). How cortically localized Par-3 establishes asymmetric Notch activity in the nucleus is not understood. Here, using *in vivo* time-lapse imaging of mitotic radial glia progenitors in the developing zebrafish forebrain, we uncover that during horizontal ACD along the anteroposterior embryonic axis, endosomes containing the Notch ligand DeltaD (Dld) move toward the cleavage plane and preferentially segregate into the posterior (subsequently basal) Notch^{hi} daughter. This asymmetric segregation requires the activity of Par-3 and dynein motor complex. Using label retention expansion microscopy, we further detect Par-3 in the cytosol colocalizing the dynein light intermediate chain 1 (Dlic1) onto Dld endosomes. Par-3, Dlic1, and Dld are associated in protein complexes *in vivo*. Our data reveal an unanticipated mechanism by which cytoplasmic Par-3 directly polarizes Notch signaling components during ACD.

1.2 INTRODUCTION

Progenitor cells need to properly balance self-renewal and differentiation. Asymmetric cell division (ACD) is an important means to impart these distinct potentials to different daughter cells. Defects in ACD are associated with diseases such as cancer and developmental disorders (1–4). Therefore, elucidating the mechanisms that regulate ACD is not only fundamental for understanding basic biology but also critical for elucidating disease etiology and devising therapeutic strategies. In metazoans, partitioning-defective (Par) protein complexes, originally found in *Caenorhabditis elegans* (5–7), are evolutionarily conserved regulators of cell polarity and ACD (8–12). Among them, Par-3 (also called PARD3, Bazooka) has been studied

in the context of neural progenitor self-renewal and differentiation from *Drosophila* to mammals (13–22). During ACD in both invertebrate and vertebrate neural progenitors, Par-3 displays asymmetric cortical localization and is required to establish, between daughter cells, the asymmetric activity of Notch signaling (Notch^{hi} versus Notch^{lo}) (20, 23–28), a key regulator of cell fate decisions (29, 30). Despite these advances, it is not known how Par-3, thought to regulate polarity exclusively through its oligomeric scaffolding properties at the cortex (31), leads to differential Notch activity in the nuclei of daughter cells. Here, we addressed this question in the context of radial glia progenitors (RGPs) of the developing zebrafish forebrain. RGPs are the principal vertebrate neural stem cells (32, 33). During active neurogenesis in the developing zebrafish forebrain, most of the RGPs undergo ACD (20). Using an antibody uptake assay (34) coupled with in vivo time-lapse imaging, we visualized the dynamics of internalized Notch ligand DeltaD (Dld) during RGP ACD. Internalized Dld was not observed in the mind bomb (*mib*) mutant that disrupts an evolutionarily conserved E3 ubiquitin ligase essential for Notch ligand endocytosis (35), suggesting that internalized Dld represents Dld endosomes. Despite the heterogeneity of RGP division modes, we observed a consistent convergent movement of Dld endosomes toward the emerging cleavage plane followed by preferential segregation into the posterior (subsequently basal) Notch^{hi} daughter. Such polarized endosome segregation was critically dependent on the activity of par-3 and dynein motor complex. Furthermore, using label retention expansion microscopy (LR-ExM), a newly developed methodology that overcomes the limitation of signal loss associated with traditional ExM (36), we unexpectedly detected cytoplasmic Par-3 that colocalized and was required to mediate the association of dynein light intermediate chain 1 (Dlic1) with Dld endosomes. In vivo coimmunoprecipitation showed that Par-3, Dld, and Dlic1 formed protein complexes. Together, our findings have uncovered cytoplasmic Par-3 and a direct role it has in localizing intracellular determinants.

1.3 RESULTS

Several methods and technologies can be used to create a library of individuals with random or targeted genetic or epigenetic variations. Some of these methodologies have been broadly used in zebrafish, whereas others have so far only been feasible in cell cultures or invertebrate genetic model organisms and may be potentially applicable to zebrafish.

1.3.1 in vivo time-lapse imaging reveals polarized dynamics of notch ligand-containing endosomes in horizontally dividing RGPs

As shown previously, in the developing zebrafish forebrain, most of the RGPs undergo ACD to generate an apical differentiating daughter with low Notch activity and a basal self-renewing daughter with high Notch activity (20). To understand how such Notch signaling asymmetry arises, we visualized internalized Notch ligand Dld using an antibody uptake assay (34) and in vivo time-lapse imaging. Intriguingly, only punctate cytoplasmic labeling was observed (Fig. 1A); no Dld was accumulated on the plasma membrane of mitotic RGPs. In the *mib* mutant, which disrupts a conserved ubiquitin E3 ligase essential for Notch ligand endocytosis (35), the punctate cytoplasmic labeling of Dld was, however, lost; fluorescence was instead largely concentrated on the plasma membrane (fig. S1A). These data indicate that the punctately labeled structures are internalized Dld in endosomes (in short, Dld endosomes). They also suggest that, in mitotic RGPs, Dld undergoes active endocytosis to be predominantly distributed in endocytic vesicles. We also evaluated whether this labeling method affected embryonic development or RGP cell division modes. The developing forebrain RGPs at this developmental stage predominantly undergo horizontal division (with the division axis parallel to the ventricular surface). No substantial differences in embryonic morphology and RGP division modes were

observed between control and Dld antibody-injected embryos (fig. S1, B to D). To observe in vivo Dld endosome dynamics during RGP divisions, we performed time-lapse imaging using 24– to 30–hours postfertilization (hpf) Tg[ef1a-MyrTdTomato] embryos (marking cell membranes): The centrosomes were labeled by microinjection of GFP-centrin mRNA at one- to four-cell stages, followed by Dld antibody injection into the forebrain ventricle at 22 hpf. The cell cycle stage of dividing RGPs was determined using Tg[ef1a-MyrTdTomato; ef1a-H2BmRFP] embryos, which marked both the cell membrane and nucleus, enabling a correlation between cell shape and DNA patterns (Fig. 1B; time 0 represents anaphase when incoming cleavage furrows become first visible). During imaging, both the apico-basal (Ap-Ba) and the anteroposterior (A-P) axes of RGPs were tracked. As shown in fig. S1 (C and D), most of the RGPs divided horizontally along the anteroposterior (A-P) embryonic axis. These horizontally dividing RGPs were therefore the focus of this study (therefore referred to as RGPs unless otherwise specified). By analyzing these dynamic videos (see movie S1), we made several intriguing observations (Fig. 1, B and C, and fig. S2). Dld endosomes were distributed throughout the cytosol during prophase to prometaphase. During metaphase, most Dld endosomes appeared to be subcortical. By anaphase, however, most Dld endosomes congregated toward the future cleavage plane and subsequently were unequally partitioned into the posterior daughter after division. Using asymmetry indices with a threshold of $|0.2|$ as previously described (25, 27), we quantitatively analyzed the distribution of internalized Dld in 88 RGPs at the telophase stage when two daughter cells were clearly discernible. The results showed that most (60.2%) of the RGPs asymmetrically partitioned Dld endosomes into the posterior daughter. Some RGPs with symmetric or anteriorly enriched Dld endosomes were also observed (Fig. 1D; see Materials and Methods for the quantification of asymmetry index), likely reflecting the heterogeneity of in vivo RGP behavior or alternatively representing, in part, the noise in the system due to mosaic Dld labeling. These observed RGPs, whether

symmetrically or asymmetrically partitioned Dld endosomes, were distributed around the forebrain ventricle in an inter-mingled manner (fig. S3). We next performed automated tracking analysis of 19 RGPs, which were captured throughout their entire mitotic cell cycle (from prophase to telophase) and, moreover, with consistent tracking of Dld endosomes in all frames. Tracking of more than 300 Dld endosomes from all 19 cells throughout the RGP mitotic cycle (45 time points) allowed us to visualize the progressive enrichment of endosomes toward the posterior daughter [Fig. 1E (E1) and movie S2]. Such enrichment could be due to directional endosome movement toward the posterior, their selective degradation at the anterior, or both. The presence of supernumerary labeled Dld endosomes made it challenging to unambiguously discern individual endosome's trajectories. Intriguingly, because of the mosaic nature of our Dld-labeling method, some RGPs contained only a single labeled Dld endosome. This enabled us to clearly track the movement of individual endosomes. We observed that the Dld endosome first moved toward the cleavage plane, followed by a directed maneuver toward the posterior side [Fig. 1E (E2 and E3) and movies S3 to S6]. Together, these data uncover polarized dynamics of Dld endosomes during horizontal RGP division and show that Dld endosomes are asymmetrically segregated into the posterior daughter in most of the RGP divisions.

1.3.2 notch ligand-containing endosomes preferentially segregate to the posterior (subsequently basal) notchhi daughter

We next asked what the possible outcome of the daughter that received a higher amount of Dld endosomes is: Will it be Notchhi or Notchlo? Previous studies have shown that Notchhi versus Notchlo is an outcome of ACD and can be used as a proxy for self-renewing versus differentiating potential in daughter cells of embryonic RGP ACD (20, 26, 27). On the basis of a previous study using the *Drosophila* sensory organ precursor (SOP) system, which has un-

covered the copresence of Delta and Notch in the same endosomes (23), we wondered whether the daughter with higher amount of Dld would also have higher amount of Notch activity (i.e., Notch^{hi}) (Fig. 2A). Because of the lack of an anti-Notch antibody that works in zebrafish, we took three different approaches to address this question. First, most RGPs that we imaged in the developing zebrafish neurogenic forebrain undergo horizontal divisions along the A-P axis (fig. S1, C and D). Shortly after division, daughter cells begin interkinetic nuclear migration and adopt differential position along the apicobasal (Ap-Ba) axis. The basal daughter is previously shown to be Notch^{hi} (Fig. 2B, left) (20). We therefore determined the relationship between the A-P daughter position immediately following RGP mitosis and the Ap-Ba daughter position shortly thereafter. Among 42 pairs of daughter cells with observable differences in their position along the Ap-Ba axis, most (67%) had more Dld in the posterior daughter that initiated an earlier basal migration (Fig. 2B, right). These results suggest that Dld endosomes are preferentially segregated to the posterior daughter, which later becomes the basal Notch^{hi} daughter. The second approach to discern the relationship between Dld endosome segregation and Notch activity involved analysis of the E3 ubiquitin ligase Mib, which is asymmetrically segregated to the apical-differentiating daughter following RGP ACD in zebrafish (20). Similar observations are also reported in the chick neural progenitors (37). By simultaneously tracking Dld endosomes and Mib distribution in 25 RGPs, we found that they were largely segregated into different daughter cells (Fig. 2C, fig. S4, and movie S7): 64% RGPs had anteriorly enriched Mib while posteriorly enriched Dld (Fig. 2D). Note that Mib–green fluorescent protein (GFP) showed anterior enrichment early on during the cell cycle, when Dld distribution appeared random. While this observation implied a potential asymmetric endocytosis, it does not appear to contribute to Dld asymmetry as internalized Dld appeared randomly distributed in RGPs during prometaphase. Together, this observation supports the notion that Dld endosomes preferentially segregate to the posterior-then-basal Notch^{hi} daughter and away from the Mib-high apical

daughter. Last, we performed in vivo clonal time-lapse imaging of internalized Dld in Tg[her4.1-dRFP] embryos, which express the Notch activity reporter (her4.1-dRFP) in RGPs. Because this reporter line does not label forebrain RGPs well (38), we performed the analysis in the developing anterior hindbrain as we have done previously (20). For clonal labeling of RGPs, GFP-containing DNA constructs were delivered via brain ventricle-targeted electroporation (39). Dld antibody was then microinjected into the brain ventricle to label internalized Dld. Three-color time-lapse imaging was subsequently carried out to simultaneously visualize RGP lineage (via sparse GFP labeling), internalized Dld (Atto647), and Notch activity (her4.1-dRFP). Eight RGPs were analyzed: In six of eight RGPs, her4.1-dRFP asymmetry was evident in daughter cells around 1 hour after anaphase. In these RGPs, Dld endosomes were found to be enriched in the daughter cell that had more her4.1-dRFP signal. By tracing the distribution of Dld endosomes throughout the cell cycle, one could see that Dld endosomes became progressively enriched toward the posterior followed by segregation into the posterior daughter, which later assumed a more basal position and with higher dRFP fluorescence (i.e., higher Notch activity) (Fig. 2, E and F, and movie S8). In two of eight RGP lineages, her4.1-dRFP appeared symmetric in daughter cells, which also bore no asymmetry of Dld endosomes (Fig. 2F and fig. S5). Together, our findings suggest that the daughter cell receiving more Dld endosomes are Notchhi, thereby supporting the notion that Dld endosomes might contain both the ligand and receptor and hence can be considered as Notch signaling endosomes.

1.3.3 Par-3 and dynein are essential for polarized dynamics of dld endosome

Par-3, an evolutionarily conserved cell polarity regulator that is asymmetrically distributed on the cell cortex (40), plays a critical role in establishing Notch signaling asymmetry in daughter cells of RGP ACD (20), but the underlying mechanisms are unclear. To determine whether Par-3 is

involved in polarizing the dynamics of Notch signaling endosomes, we disrupted the activity of the zebrafish orthologous gene *pard3ab* (therefore referred to as *par-3*) via microinjection of a well-established antisense morpholino oligo-nucleotide (MO) (19, 20, 41). Despite the fact that a maternal zygotic germline *pard3ab* knockout has been previously generated, it has grossly normal brain morphology and survives largely to adulthood (42). This phenotype is distinct from defective brain morphology and abnormal proliferation/differentiation states observed in the morphants, suggesting that genetic compensation (43) is at play. Therefore, this knockout line is deemed unsuitable for our study. Imaging of internalized Dld in *par-3* morphants uncovered that, while Dld endosomes underwent largely normal subcortical association and congregation toward the future cleavage plane, their final asymmetric segregation into the posterior daughter was significantly disrupted (Fig. 3, B and E to G, and movie S9). This defect was rescuable by *Par-3*-GFP mRNA injection (fig. S6). These data, together with the observed knockdown of *Par-3* protein in RGP (fig. S8), validate the MO specificity and efficacy in our system and suggest that *Par-3* is essential for polarized segregation of Notch signaling endosomes during RGP ACD. Previous studies in *Drosophila* SOPs have uncovered a critical role of plus-end kinesin motors in the initial targeting of Notch signaling endosomes toward the cleavage plane (24). However, motor involvement in the later asymmetric segregation step is not known. In dividing zebrafish RGP, we observed directed movements of Dld endosomes toward the posterior, which implies that the final polarization process might also be motor dependent. We therefore examined whether minus-end dynein motors might play a role. The pharmacological dynein inhibitor ciliobrevin D (CBD) was applied to zebrafish embryos at a concentration that still enabled RGP cell division. In CBD-treated RGP, we observed that the Notch signaling endosomes were much larger in appearance as if they “collided” into one another. These “enlarged” endosomes remained at the cleavage furrow throughout the division (Fig. 3, C and E to G, and movie S10). We next sought to genetically test the involvement of dynein in the

polarized dynamics of Notch signaling endosomes by investigating the role of *dync1li* (dynein cytoplasmic 1 light intermediate chain, also referred to as *dlic*) genes. This experiment was motivated by a previous study reporting an interaction between DLIC2 and Par-3 in cultured NIH 3T3 cells (44). While invertebrates have a single *dlic* gene (45, 46), vertebrates have evolved to express two *dlic* genes (*dlic1* and *dlic2*), which are thought to define tissue- or cell type-specific dynein complexes (47). Among all the cytoplasmic dynein subunits, *Dlic* is the least well understood. It contains a RAS-like domain that interacts with the dynein heavy-chain and a C-terminal domain contacting activating adaptors and, in some cases, the cargo (48). We therefore sought to perturb *dlic1* and *dlic2* activity and ask whether it would disrupt the polarized dynamics of Dld endosomes in zebrafish RGP. MO-mediated knockdown has certain advantages over germline knockouts. First, it circumvents the troubling genetic compensation effect (e.g., as in the case for *pard3ab*). Second, the concentration of MOs delivered to each embryo can be titrated to obtain partial knockdown, which provides an opportunity to bypass early embryonic arrests (e.g., as in the case for dynein subunit-encoding genes, which are essential for cell division). Last, MOs can be conveniently delivered into transgenic lines harboring multiple transgenes for live-imaging purposes. Getting multiple transgenes together with one or multiple homozygous germline knockout alleles in a single embryo is challenging and time-consuming. Together, MOs are effective tools for performing gene knockdowns, if proper controls for validating efficacy and specificity are included. We used established MOs that target *dlic1* and *dlic2* in zebrafish in our study (49). Although both MOs disrupted embryonic development (e.g., as shown by the enlarged yolk indicative of reduced growth rate; fig. S7A), only *dlic1* MO affected Dld asymmetry in mitotic RGPs (Fig. 3, D to G, and fig. S6, C to E). To evaluate MO efficacy in the context of our system, we used an anti-*Dlic*-Cter antibody against the *Drosophila* isoform (50) because of the lack of antibodies against zebrafish *Dlic1* and *Dlic2*. Western blotting on 24-hpf embryos detected a major band of ~54 kDa (the expected size

for zDlic1 and zDlic2 proteins). This band was significantly reduced in the dlic1 morphants but was increased in the dlic2 morphants (fig. S7B). Furthermore, immuno-reactivity was detected in mitotic RGPs, which was significantly reduced again in the dlic1 (but not the dlic2) morphants (fig. S7C). This observation is consistent with the notion that the Drosophila anti-Dlic-Cter antibody specifically recognizes zDlic1 but not zDlic2. These results further suggest that dlic1 is expressed in mitotic RGPs and can be effectively knocked down by the dlic1 MO, resulting in disrupted Dld asymmetry. However, no conclusion can be drawn from our data regarding the role of zDlic2, as we are unable to verify the efficacy of dlic2 MO because of the lack of a zDlic2-specific antibody. To further evaluate the specificity of dlic1 MO, we microinjected MO-insensitive dlic1 mRNA. The loss of polarized Dld endosome dynamics in dlic1 MOs was rescued by such mRNA injection (fig. S6, B, D, and E). Together, these results have thus validated the efficacy and specificity of dlic1 MO and suggest that dlic1 plays a critical role in directional Dld endosome transport in mitotic RGPs. DLIC1 is involved in endosomal transport in cultured human cells (51), suggesting that it may be the isoform that engages endosomes as cargoes. Thus, combined pharmacological and genetic perturbation of dynein function, while not affecting the congregation of Notch signaling endosomes toward the cleavage plane, selectively disrupts their asymmetric segregation into the posterior daughter during RGP ACD.

1.3.4 Par-3 and Dld endosomes are preferentially co-segregated to the posterior daughter following RGP division

Having established an essential role of Par-3 and the dynein motor in polarizing the distribution of Dld endosomes during RGP ACD, we next asked how they might perform such function. In both invertebrates and vertebrates, Par-3 protein displays prominent cortical asymmetry and is widely considered to function at the cell cortex during ACD (19, 40, 52, 53). To understand how

Par-3 cortical asymmetry relates to polarized Dld endosome dynamics, we performed in vivo time-lapse imaging to simultaneously track the dynamics of Par-3 and internalized Dld in dividing RGPs. Par-3-GFP, which is shown fully functional through rescue experiments (fig. S6) (41), was used as a live reporter. Previous studies in mammalian forebrain cortical RGPs find that the daughter cell inheriting a greater amount of Par-3 develops high Notch activity and remains a RGP, whereas the daughter cell inheriting less Par-3 harbors low Notch activity and adopts an intermediate progenitor or neuronal fate (27). In contrast, in the developing zebrafish caudal hindbrain and anterior spinal cord (from 20 to 30 hpf), Par-3 is reported to segregate into the neuronal daughter following neural precursor ACD (19). These differences could be related to the differences in species or due to spatiotemporal heterogeneity of progenitors. To determine the nature of Par-3 and Dld dynamics in the developing zebrafish forebrain RGPs, we microinjected the mRNAs encoding Par-3-GFP and histone H2B-monomeric RFP (H2B-mRFP) (for marking chromosomes) into 1 cell of 16- to 32-cell stage embryos to achieve sparse labeling; the Dld antibody was subsequently microinjected into the brain ventricle at ~24 hpf. Time-lapse imaging was performed at ~28 to 30 hpf. We found that, during prophase and metaphase, Par-3 was prominently localized to the apical cortex (Fig. 4A). As the cell cycle progressed, beginning around anaphase, cortical Par-3 shifted more toward the posterior. Symmetric segregation (Fig. 4B) or asymmetric segregation of Par-3 and Dld to the anterior daughter (Fig. 4C) was also observed. Among 54 RGPs examined, most (64.8%) showed posteriorly enriched Par-3 at the telophase (Fig. 4D). Further quantifications of both internalized Dld and Par-3 at the telophase stage showed that most of the RGPs (59.2%) segregated both Par-3 and Dld into the posterior daughter (Fig. 4D). These observations are consistent with the heterogeneity of RGP behavior or, alternatively, reflecting, to a certain extent, the noise introduced by mosaic Dld labeling. Nevertheless, these results show clearly that, following RGP division in the developing forebrain, Par-3 preferentially co-segregates with Dld endosomes to

the posterior daughter that is Notch^{hi} (as shown in Fig. 2).

1.3.5 Cytoplasmic Par-3 decorates Dld endosomes and is required to recruit Dlic1

Notably, in dividing RGPs, some weak Par-3-GFP signal appeared to be present in the cytoplasm (e.g., Fig. 4A; 3 min). While previous studies are focused on the cortical Par-3, which is much more abundant and considered to be the active form, we were intrigued by the possible presence and function of cytosolic Par-3. To verify the cytosolic presence of Par-3 protein, we used an anti-Par-3 antibody, the specificity of which was validated by both Western blot and immunofluorescence (IF) labeling on the *par-3* morphants without or with MO-insensitive Par-3-GFP mRNA coinjection (fig. S8). While live imaging uses a reporter to uncover protein dynamics and can be limited in detecting lowly expressed proteins, IF labeling detects endogenous proteins on fixed-sample preparations. Depending on the quality of antibodies and the accessibility of antigens, IF labeling can offer higher sensitivity than live imaging. co-IF labeling of Par-3, Dlic1, and Dld detected punctate Par-3 immunoreactivity in the cytosol that appeared in close proximity to Dlic1 and Dld immunoreactivity (Fig. 5A and fig. S8). Analyses of protein colocalization with organelles such as endosomes require specific methods, as the fluorescence signals may not appear to exactly overlap because of the size of the organelle (average endosome diameters of 250 to 1000 nm). Using such method that is shown to work well for quantifying colocalization of proteins with endosomes (24, 54), we analyzed colocalization of these proteins in the cytoplasmic area in between two nuclei of the anaphase telophase RGPs (Fig. 5B). At this image resolution, ~60% of total Par-3 immunoreactivity colocalized with Dlic1, whereas about 30% of total Dlic1 immunoreactivity colocalized with Par-3. This difference was expected given the broad role of Dlic1 in other dynein-mediated processes. It was further observed that the colocalization of Dld with Dlic1 was significantly

decreased in *par-3*-deficient embryos, which was rescued by Par-3-GFP mRNA injection (Fig. 5B). This observation suggests an essential role of Par-3 in localizing Dlic1 (in turn, the dynein motor) to Dld endosomes. To visualize at high resolution the cytoplasmic Par-3 in relationship to Dld endosomes and Dlic1, we applied LR-ExM. ExM physically expands biological samples to enable nanoscale superresolution via diffraction-limited confocal microscopy (55, 56). LR-ExM further overcomes the limitation of signal loss associated with traditional ExM and enables high-efficiency protein labeling using an engineered set of trifunctional anchors (36). Twenty-four- to 28-hpf embryos expressing Par-3-GFP and with internalized Dld were processed for immunolabeling of GFP and Dlic1 followed by LR-ExM. In addition to the cortex, Par-3-GFP was detected in the cytosol in close proximity to Dlic1 and Dld (Fig. 5C). The ring-shaped distribution patterns of Dlic1 and Par-3 together with the diameter of the ring suggest that they decorate Dld endosomes. We also performed LR-ExM by immunolabeling of endogenous Par-3. The results showed similar colocalization of endogenous Par-3 and Dlic1 on Dld endosomes (fig. S9A). Quantification of colocalization after LR-ExM (Fig. 5D) showed patterns that were largely consistent with those observed while analyzing low-magnification images (Fig. 5B). Last, conventional *in vivo* coimmunoprecipitation (co-IP) was performed to determine whether Par-3, Dlic1, and Dld could be detected in protein complexes. One- to 2-day-old zebrafish embryos were homogenized and incubated with each of the antibodies against Dld, Dlic1, or Par-3. The corresponding immunoprecipitants were then probed with each of these antibodies by Western blotting (fig. S9B). The results showed that IPing Dld was able to co-IP Par-3 and Dlic1; likewise, IPing Par-3 or Dlic1 was able to co-IP other two proteins. These results provide further biochemical validation that Dld, Dlic1, and Par-3 are associated in complexes *in vivo*.

1.4 DISCUSSION

The evolutionarily conserved polarity regulator Par-3 is required for differential activity of Notch signaling in daughter cells of asymmetrically dividing RGP (20), but the underlying mechanisms are unclear. Using *in vivo* time-lapse imaging and ExM, in combination with molecular genetics, pharmacological, and biochemical approaches, we have uncovered a role of cytoplasmic Par-3 together with the dynein motor in polarized transport of Dld endosomes (Fig. 5E). This study, together with previous work (24), reveals an evolutionarily conserved role of Par-3 in polarizing Notch signaling endosomes. However, Par-3 appears to do so through distinct mechanisms: In *Drosophila* SOPs, Par-3 is previously shown to regulate central spindle asymmetry (24); here, we show that in zebrafish RGP, Par-3 in the cytoplasm engages dynein in polarized transport of endosomes. It is worth noting that a role of Par-3 in regulating central spindle asymmetry has not been investigated in zebrafish; likewise, a role of Par-3 in dynein-mediated polarized transport of Notch signaling endosomes has not been examined in *Drosophila* SOPs. Therefore, future studies are needed to determine whether convergence of these mechanisms can be observed in different cellular contexts. Similar species-related differences have also been observed in terms of polarized segregation of cortical Par-3. In the developing mammalian cortex (part of the forebrain), the daughter cell that inherits a greater amount of Par-3 is suggested to develop higher Notch signaling activity (27). However, in the developing zebrafish caudal hindbrain and anterior spinal cord, Par-3 is reported to be segregated to the neuronal daughter during the ACD that generates a progenitor and a neuron (19). Our studies of the developing zebrafish forebrain uncover that Par-3 and Dld endosomes are preferentially co-segregated into the posterior daughter in horizontally dividing RGP. Using three independent approaches (cell position tracking, referencing Mib distribution, and direct

visualization with the Notch activity reporter), we have demonstrated that the posterior daughter is preferentially Notchhi. Thus, horizontally dividing zebrafish forebrain RGPs are similar to the mammalian cortical RGPs in their patterns of co-segregating cortical Par-3 and Notch activity. Future studies are needed to understand the relationship between Par-3 and Notch activity in other cell types (e.g., hindbrain and spinal cord) in zebrafish. During ACDs studied across different metazoan species, Par-3 displays prominent cortical localization (19, 40, 52, 53). This cortical Par-3 has received much attention as key to establishing polarity (e.g., by sequestering atypical protein kinase C) (31, 57). Cytoplasmic Par-3, released from the membrane via phosphorylation by Par-1 (58–61), has been considered a largely nonfunctional form in the context of polarity regulation. Being able to visualize Par-3 in the cytoplasm in association with the dynein motor and Dld endosomes as we have done in this study suggests a direct role of cytoplasmic Par-3 in actively localizing intracellular determinants. Cytoplasmic Par-3 has been associated with adverse cancer prognosis in clinical settings (62), further suggesting that this form of Par-3 and its dynamic relationship with the cortex-associated oligomeric ensemble deserve more attention in future studies.

1.5 MATERIALS and METHODS

1.5.1 Experimental Design

Mitotic RGP in the developing zebrafish forebrain during active neurogenesis were analyzed using a combination of in vivo time-lapse imaging, molecular genetics, pharmacology, biochemistry, and other advanced microscopic methods, which has uncovered a novel role of cytoplasmic Par-3 in recruiting dynein and actively localizing intracellular determinants.

1.5.2 Zebrafish strains and maintenance

Wild-type (WT) embryos were obtained from natural spawning of AB adults, staged, and maintained according to established protocols (63). Embryos were raised at 28.5°C in 0.3× Danieau's embryo medium (30× Danieau's embryo medium contains 1740 mM NaCl, 21 mM KCl, 12 mM MgSO₄·7H₂O, 18 mM Ca(NO₃)₂, and 150 mM Hepes buffer). Embryonic ages were described as hpf. To prevent pigment formation, 0.003% phenylthiourea (PTU) was added into the medium at 24 hpf. The following zebrafish mutants and transgenic lines were used: *mibta52b* (35), Tg [*ef1a:Myr-Tdtomato*] and Tg [*ef1a:H2B-RFP*] (64), and Tg [*her4.1-RFP*] (38). All animal experiments were approved by the Institutional Animal Care and Use Committee at the University of California, San Francisco, USA.

1.5.3 Morpholinos

Knockdown experiments were carried out using previously characterized translational blocking antisense MOs: *pard3ab/par-3* MO (5' -TCA AAG GCT CCC GTG CTC TGG TGT C-3') (19,

20, 41, 65), *dync1li1/dlic1* MO (5' -GTG TAT TTC TGC CCG TCG TCG CCA T-3'), and *dync1li2/dlic2* MO (5' -TTC TTC TCT AAA ACG GGA GCC ATC T-3') (49). Standard control MO (5' -CCT CTT ACC TCA GTT ACA ATT TAT A-3') was used as injection controls (Gene Tools). All MOs were stored at 300 mM in distilled water. For microinjection, ~4 nl of the diluted MO at 100 mM in the injection mixture containing 0.05% phenyl red (corresponding to 4 ng of MOs) was injected into the yolk of one- to four-cell stage embryos..

1.5.4 Pharmacology

The Zebrafish embryos were treated with the dynein inhibitor CBD [Calbiochem via Sigma-Aldrich, 250401-10MG; 2.5 μ M in 0.1% dimethyl sulfoxide (DMSO), 0.3 \times Danieau's buffer] from 18 to 24 hpf. Vehicle (DMSO)-treated control and CBD-treated embryos were then embedded in 1.2% low-melting point agarose in the Danieau medium, supplemented with 2.5 μ M CBD and 0.003% tricaine, and subjected to Dld antibody uptake assay and in vivo time-lapse imaging.

1.5.5. DNA plasmids and complementary DNA preparation

The Plasmid DNAs (pCS2-H2B-mRFP, pCS2-mib-GFP, Pef1a-gal4, and Puas-E1b-EGFP) were prepared as previously described (20, 39). pCS2-par-3-GFP plasmid was a gift from J. von Trotha (66). pCS2- GFP-centrin plasmid was a gift from W. A. Harris (67). For mib-GFP, GFP is at the 3' end of Mib protein. For par3-GFP, GFP is at the 3' end of Par-3 protein. For GFP-centrin, GFP is at the 5' end of centrin. pCS2+-*dlic1* was made by cloning the *dlic1* complementary DNA (ensemble: ENSDARG00000098317) with codon-optimized sequence to

avoid binding by the *dlic1* MO. The total RNA from 10 larvae of 5 dpf was extracted and purified by using the RNAqueous- Micro Total RNA Isolation Kit (Invitrogen, AM1931). The pair of primers used for reverse transcription polymerase chain reaction is 5' -ATT CAT GGA TCC ATG GCC ACC ACC GGA CGC AAC ACT TTA CTA TCG GTT AGC ACA AAT G-3' and 5' - AAT ACT CTC GAG TCA GGA TTT GTC GTT TTC AGC AGG G-3' , which contain the restriction enzyme sites+of Bam HI and Not I for the digestion and ligation with the pCS2 vector plasmid.

1.5.6. mRNA synthesis and microinjections

Plasmids (pCS2-H2B-mRFP, pCS2-mib-GFP, pCS2-par-3-GFP, and pCS2-GFP-centrin) were linearized by the restriction enzyme Not I digestion. Not I-linearized plasmids were purified (QIAquick Gel Extraction Kit), and the 5' -capped mRNAs were synthesized using the SP6 mMessenger mMachine Kit (Ambion). For GFP-centrin, H2B-mRFP, mib-GFP, and par-3-GFP mRNA mRNA injection, 4-nt mRNAs at 0.2 to 0.5 $\mu\text{g}/\mu\text{l}$ were mixed with an equal volume of injection buffer containing 0.05% phenyl red and injected into the yolk of a one- to four-cell stage embryos. For par-3-GFP mRNA injection, the mRNAs were injected into single cells at the 32- to 64-cell stages to obtain mosaic expression. All injections were done with an injector (WPI PV830 Pneumatic Pico Pump) and a micro- manipulator (Narishige, Tokyo, Japan).

1.5.7. Anti-Dld antibody uptake assay

Anti-mouse immunoglobulin G (IgG)–Atto647N (Sigma-Aldrich, 50185) was used for labeling the mouse monoclonal anti-Dld antibody (Abcam, ab73331). For antibody conjugation, 1 μl of anti-

Dld antibody (0.5 mg/ml) was mixed with 2.5 μ l of anti-mouse IgG-Atto647N antibody (1 mg/ml) and incubated at room temperature for 30 min or on ice for 2 to 3 hours. After incubation, 2.5 μ l of blocking buffer [mouse IgG (10 mg/ml) with 5 mM azide] and 0.5 μ l of 0.5% phenol red (Sigma-Aldrich, P0290) were added for blocking the unconjugated anti-mouse IgG-Atto647N and vortexed thoroughly. Mixtures without anti-Dld antibody were used as control. Before microinjection, 24- to 26-hpf embryos were anesthetized in the Danieau medium supplemented with 0.003% tricaine followed by embedding in 1.2% low-melting point agarose. Ten nanoliters of labeled Dld antibody was injected into the hindbrain ventricle. The phenol red indicator serves to show the diffusion of antibody mixture into the forebrain ventricle. The injected embryos were then released from agarose and cultured in the Danieau medium for 2 hours before imaging.

1.5.8. Brain ventricle-targeted electroporation of plasmid DNAs

Pef1a-gal4 and Pvas-E1b-EGFP plasmids were mixed at 500 ng/ μ l for each, and about 20 nl of mixture was microinjected into the hindbrain ventricles of 20- to 22-hpf Tg [her4.1-RFP] embryos embedded in 1.2% low-melting point agarose. The electroporation setting and procedures were according to previously established protocols (39). Electroporated embryos were released from agarose and transferred to a fresh dish of embryonic medium containing 0.003% PTU and incubated at 28.5°C. Electroporated embryos were checked under a fluorescent stereo microscope after 6 to 8 hours. The embryos with sparsely GFP-labeled RGP were subjected to the Dld antibody uptake assay followed by in vivo time-lapse imaging.

1.5.9. Antibodies, western blotting, and immunocytochemistry

Primary antibodies used in this study were as follows: mouse anti-Dld [Abcam, ab73331; Research Resource Identifier (RRID): AB_1268496; lot GR115501-3; 1:200 dilution for immunostaining] (20), chicken anti-GFP (Abcam, ab13970; RRID: AB_300798; lot GR3190550-20; 1:500 dilution for immunostaining), rabbit anti-Par-3 (Millipore 07-330; RRID: AB_2101325; lot 3322358; 1:500 for immunostaining) (validated in this study), guinea pig anti-DLIC-Cter (a gift from T. Uemura; 1:100 for immunostaining and 1:500 for Western blotting, validated in this study) (50), and rabbit anti- α -tubulin (Santa Cruz Biotechnology, SC-12462; RRID: AB_2241125; lot A2907; 1:1000 for Western blotting). Secondary antibodies used for IF labeling were as follows: Alexa-conjugated goat anti-rabbit (Alexa 568; Invitrogen, A11011; RRID: AB_143157; lot 792518), goat anti-chicken (Alexa 488; Invitrogen, A11039; RRID: AB_142924; lot 2020124), goat anti-mouse (Alexa 488; Invitrogen, A11002; RRID: AB_2534070; lot 1786359), goat anti-guinea pig (Alexa 488; Invitrogen, A11073; RRID: AB_2534117; lot 46214A), or donkey anti-guinea pig (Alexa 647; the Jackson laboratory, 706-605-148; RRID: AB_2340476; lot 102649-478). All were used at 1:1000 dilution. Secondary antibodies used for Western blotting were as follows: Amersham ECL donkey anti-rabbit IgG horseradish peroxidase (HRP; GE Healthcare, NA934V; RRID: AB_772211; lot 16921443) and rabbit anti-guinea pig IgG (H + L) HRP (Sigma-Aldrich, A5545; RRID: AB_258247). All were used at the 1:2000 dilution. Secondary antibodies used for trifunctional linker conjugation in LR-ExM were as follows: goat anti-guinea pig IgG (H + L) unconjugated secondary antibody (Invitrogen, A18771; RRID: AB_2535548), goat anti-rabbit IgG (H + L) cross-adsorbed unconjugated secondary antibody (Invitrogen, 31212; RRID: AB_228335), and goat anti-chicken IgY (H + L) unconjugated secondary antibody (Invitrogen, A16056; RRID: AB_2534729). For Western blotting, lysates from 15 to 20 28-hpf embryos were homogenized in

80 μ l of SDS sample buffer; 15 μ l of lysate was used for SDS–polyacrylamide gel electrophoresis (Bio-Rad). Proteins were transferred to a Hybond nitrocellulose membrane by a semidry blotting technique with a Turbo-transblotting cell (Bio-Rad) and detected with appropriate antibodies as previously described (68). After the HRP-conjugated secondary antibody incubation, the samples were visualized using the SuperSignal West Dura Extended Duration Substrate (Thermo Fisher Scientific) with the LI-COR Western blotting detection system (LI-COR Biosciences). For the preparation of cryosections, 28-hpf embryos were fixed overnight at 4°C in phosphate-buffered saline (PBS) buffer with 4% paraformaldehyde. Fixed embryos were washed and incubated in PBS buffer containing 30% sucrose overnight at 4°C. Embryos were then transferred to plastic molds, with the sucrose buffer removed and optimum cutting temperature (OCT) (Tissue-Tek) added. After orienting the embryos to proper positions in the mold, the block was frozen on dry ice. Blocks can be stored at –80°C up to several months. Frozen blocks were then cut into 20- μ m sections on a cryostat (Leica) and mounted on Superfrost Plus slides (Thermo Fisher Scientific). The slides were dried at room temperature for 2 to 3 hours and then stored at –80°C until use. For immunocytochemistry, samples were first washed and pre-incubated in PBS containing 0.1% Tween 20 or 0.25% Triton X-100 (PBS-T; pH 7.4) with 1% DMSO and 5% natural goat serum at 4°C overnight or longer. They were then incubated with primary antibodies in the preincubation solution (PBS-T with 5% natural goat serum) overnight at 4°C. The samples were then washed thoroughly with PBS-T five times \times 10 min each time, followed by incubation in Alexa-conjugated goat anti-rabbit (Alexa 568), goat anti-chicken (Alexa 488), goat anti-mouse (Alexa 488), or goat anti–guinea pig (Alexa 647) secondary antibodies (diluted 1:1000) in the preincubation solution for over 2 hours at room temperature or overnight at 4°C. The samples were washed with PBS-T twice for 10 min each, thrice with PBS for 10 min each, and once with 50% glycerol in PBS for 1 hour, followed by infiltration overnight in 80% glycerol/PBS before imaging. Imaging was done using a confocal

microscope (Nikon CSU-W1 Spinning Disk/confocal microscopy) with a 100× oil immersion objective. The z-step of the imaging stack is 0.26 μ m.

1.5.10. Time-lapse in vivo imaging

Time-lapse in vivo imaging was done using a confocal microscope (Nikon CSU-W1 Spinning Disk/High Speed Widefield confocal microscopy) with a 40× water immersion objective. Embryos were mounted with 1.2% low-melting point agarose (0.3× Danieau medium and 0.003% tricaine) in glass-bottom culture dishes (MatTek; 35 mm) with the dorsal forebrain facing the coverslip. For in vivo time-lapse imaging of internalized Dld, Mib-GFP, or Par-3-GFP in dividing RGP of Tg [ef1a:Myr-Tdtomato], z-stacks with 20 to 30 z-planes were acquired consecutively at a 1- μ m z-step for each embryonic forebrain region. The exposure time for each fluorescent channel was set at 100 ms by choosing the sequential channel scanning mode for each z-plane. The interval between each z-stack ranged from 12 to 30 s, depending on the z-stack settings of the samples. Usually, 80 volumes of z-stacks were captured for each time-lapse imaging, and the duration spanned about 30 min. For long-term imaging, embryos were placed on a temperature-controlled stage set at 28.5°C. For imaging Notch activity in paired daughter cells using Tg[her4.1-RFP] embryos, a GFP reporter plasmid was electroporated into the hindbrain region to label individual RGPs as this transgenic line was reported to better recapitulate Notch activity in the hindbrain than in the forebrain (38). Z-stacks with 50 to 60 z-planes were acquired consecutively with a 1- μ m z-step for each volume. The scanning interval between volumes of z-stacks was set at 6 min. The exposure time for each channel was set at 100 ms for each z-plane as described above. For each embryo, 100 to 120 volumes of z-stacks were captured lasting ~12 hours. Data presented in figure panels corresponded to maximum intensity projections of 5 to 10 z-planes with 1- μ m z-step size, representing the approximate

size of RGP.

1.5.11. Label retention expansion microscopy

LR-ExM was performed on cryosections of a 28-hpf embryonic forebrain. Chicken anti-GFP antibody (for detecting Par-3-GFP) or rabbit anti-Par-3 antibody (for detecting endogenous Par-3) and guinea pig anti-Dlic-Cter antibody were used, in conjunction with visualizing DId (either internalized Atto-labeled DId or endogenous DId labeled with mouse anti-DId antibody). Buffers were prepared as previously described with modifications needed for processing in vivo tissue samples (36). The forebrain sections were blocked in blocking buffer, PBS containing 0.1% Triton X-100 (PBS-T, pH 7.4) with 5% natural goat serum overnight at 4°C. The slides were then incubated with primary antibodies in the preincubation buffer overnight at 4°C as described in the immunocytochemistry section above. After washing off primary antibodies, tissue sections were incubated with trifunctional linkers {N-hydroxysuccinimide (NHS)-methacrylamide (MA)-biotin-conjugated anti-chicken (or anti-rabbit) IgG (for visualizing Par-3), and NHS-MA-digoxigenin (DIG)-conjugated anti-guinea pig IgG (for visualizing Dlic1) [stock (200 mg/ml), dilute 1:100 before use]} in the preincubation buffer overnight at 4°C in the dark. After washes in PBS four times (5 min each) in the dark, freshly prepared 40 μ l of gelation solution was added on each section to cover the whole-tissue sample. The gelation solution was prepared by deoxygenizing the gel monomer solution using a vacuum pump for over 15 min before adding tetramethylethylenediamine (TEMED) and ammonium persulfate (APS), to enhance the effects of trifunctional linkers. The gelation solution-covered samples, protected from light, were incubated in a humidity chamber and allowed to undergo gelation at 37°C for 1 hour. The gelated samples were incubated in the digestion buffer [proteinase K (8 U/ml) in 50 mM tris (pH 8.0), 1 mM EDTA, and 0.5% Triton X-100] on the slides 4 hours at 37°C or overnight at room

temperature. At least 10-fold excess volume of digestion buffer was used. Sufficient digestion enabled sections embedded in gels to slide off the glass surface. The gels were washed with excess volume of 150 mM NaCl in six-well plates (black-walled plates, CellVis P06- 1.5H-N), at least 5 ml in each well four times, 20 to 30 min each time. After washing off the digestion buffer, the gel samples were incubated in the staining buffer [10 mM Hepes and 150 mM NaCl (pH 7.5)] with 3 to 5 μ M Alexa Fluor 488–streptavidin, 3 to 5 μ M goat anti- digoxigenin/digoxin Dylight 594, anti-mouse Atto647N (1:500), and 4',6-diamidino-2-phenylindole (1:1000) for 24 hours at 4°C in the dark. Last, the gels were washed four times with milli-Q water (30 min for each wash) at 4°C in the dark. The gel expanded approximately four times of the original sample size after washing and was ready for imaging in the well under the confocal microscope (Nikon CSU-W1 Spinning Disk/High-Speed Widefield confocal microscopy) with a 60 \times water immersion objective. The excess water in the well was removed to keep the gel-embedded samples adhered to the glass dish bottom. For immobilization of the gel, 2% low-melting point agarose was added onto the edge of the gel-embedded samples before imaging. The scanning z-step is 0.26 μ m.

1.5.12. Image analyses

All the confocal imaging stacks were captured and processed using Micro-Manager 2.0 gamma (μ Manager, University of California) and ImageJ. For generating kymographs of internalized DId in dividing RGPs, maximum intensity projection of five to seven z-planes (1- μ m z-step) was applied to the three-dimensional image stacks to cover the entire RGP. Each RGP at every time frame was manually segmented according to the cell membrane labeling. Each single DId endosome was located from all frames using a Gaussian fitting algorithm assisted with the ImageJ-embedded plugin TrackMate (69), by choosing “LoG” detector and setting the

“estimated diameter” to be about 8 pixels and “threshold” to be about 3 pixels (pixel width and pixel height are 0.164 μ m, and voxel depth is 1 μ m). The Linear Assignment Problem (LAP) tracker was adopted without “allow gap closing.” All Dld endosomes tracked on each image frame were pre-viewed and compared to the original frame. The threshold parameter was then adjusted on the basis of this visual feedback. The two labeled centrosomes were used to define the anteroposterior (A-P) axis: The anterior centrosome was given the coordinate of 0, and the posterior centrosome was given the coordinate of 1. Each Dld endosome was then projected onto this axis to obtain its relative distance (value between 0 and 1). The relative distances of all tracked Dld endosomes were then used to generate the kymograph, where the grayscale value of each pixel indicates the probability of Dld endosomes appearing at the corresponding location at a given time. Movies for each RGP used for kymograph analyses were registered spatiotemporally: The spatial registration was done by adopting the center point between two centrosomes as the center of dividing RGPs. The temporal registration was done by adopting the anaphase with the first appearance of cleavage furrow to be $T = 0$ min. The first appearance of the cleavage furrow was also verified in a set of embryos with double labeling of cell membrane and nucleus. Almost all WT (or control MO-injected) RGPs complete their cytokinesis at $T = 2$ min. However, for RGPs in *par-3* MO, *dlic* MO, or CBD-treated embryos, the time from first appearance of the cleavage furrow ($T = 0$ min) to the completion of cytokinesis ($T = 2$ min in control) was variable because of possible cell cycle defects. We therefore normalized this to WT cell cycle by considering the completion of cytokinesis as $T = 2$ min.

1.5.13. Quantification and statistical analysis

The number of times each experiment was repeated was provided in the figures or figure legends. For live imaging, one or multiple RGPs were analyzed from each embryo, depending on the number of mitotic RGPs that were present in each image stack. For immunocyto-

chemistry experiments, multiple sections from individual brains were analyzed. No statistical methods were used to predetermine sample size. Sample size was determined to be adequate on the basis of the magnitude and consistency of measurable differences between groups. No randomization of samples was performed. Embryos used in the analyses were age-matched between control and experimental conditions, and sex cannot be discerned at these embryonic stages. Investigators were not blinded to chemically or genetically perturbed conditions during experiments. Data are quantitatively analyzed. Statistical analyses were carried out using Prism 8 version 8.4.2: The mean value with SEM was labeled in the graphs. The two-tailed unpaired t test was used to assess significance. To compare the proportions of each cell division orientation (extended data in Fig. 1), normal (z) test for proportions (implemented by Python's statsmodels package) (70) was used. The chi-square analyses were also applied in Fig. 3 and fig.S6.

1.5.14. Measurement of asymmetry index

The total fluorescence intensity of internalized DId (or Mib-GFP and Par-3-GFP) in paired daughter cells immediately after abscission (i.e., at telophase of mother RGP division) was measured by ImageJ. To quantitatively describe the distribution, normalized ratio of fluorescence between the two newly formed daughter cells was calculated as follows

$$X = \frac{\sum_{i=1}^n (DId)_P - \sum_{i=1}^n (DId)_A}{\sum_{i=1}^n (DId)_P + \sum_{i=1}^n (DId)_A}$$

Figure 1.1 Measurement of asymmetry index.

$\Sigma(\text{Dld})\text{P}$ means total intensity in the posterior daughter cell, and $\Sigma(\text{Dld})\text{A}$ means total intensity in the anterior daughter cell. “0” indicates perfect symmetry, and “1” or “-1” indicates absolute asymmetry (posterior or anterior, respectively). For filtering out potential noise, we defined asymmetry when $\Sigma(\text{Dld})\text{P}$ is 50% more or less than $\Sigma(\text{Dld})\text{A}$, as has been previously used for quantifying Par-3 asymmetry (27) and internalized Dld-containing Sara endosome asymmetry (25). It means that when $X \geq 0.2$, Dld endosomes (or Mib-GFP and Par-3-GFP) are considered asymmetric with more in the posterior daughter, and when $X \leq -0.2$, they are considered asymmetric with more in the anterior. The asymmetry index for Par3-GFP included both membrane and cytoplasmic fluorescence.

1.5.15. Colocalization

To measure the colocalization of Dlic1 and Par-3 (or Par-3-GFP), in the context of Dld (either internalized or immunostained) endosomes in the cytosol of dividing RGPs, we adopted the methods as previously described for measuring colocalization in the context of endosomes (24, 54). This method is distinct from conventional, intensity correlation coefficient-based colocalization method, which performs poorly because the membrane of endosomes is organized as a mosaic of domains (71). Immunostained mitotic RGPs were segmented, and maximum intensity projections of 10 consecutive z-planes (with 0.26- μm z-step size) were generated, which typically covers the central cytoplasmic area between the nuclei (~2.6 μm). The area of 60 \times 100 pixels (1 pixel = 0.064 μm) was then cropped for colocalization analysis using the JACop plugin in ImageJ. The colocalization between each fluorescent channel (i.e., the proportion of each fluorescence colocalized with another) was measured using Manders' coefficients (72). We used an optimized XY block size of 2 pixels (54). To remove potential background noise, the threshold of each channel was set in JACop using a blank area on the image (i.e., without tissue samples) as a negative control. Costes' automatic threshold was fur-

ther applied for each measurement. Costes' automatic threshold is an algorithm that identifies and removes noise using scatter plotting of randomized images generated from the image under analysis (73). It automatically quantifies colocalization without the bias of visual interpretation. For RGPs from LR-ExM, the maximum intensity projections of 10 consecutive z-planes (0.26- μ m z-step size scanned with a 60 \times water immersion objective) were generated. The central cytoplasmic area between the nuclei was then selected, and XY block size was defined as 1 pixel for JACop colocalization analyses.

1.6 ACKNOWLEDGMENTS

We thank M. Wagle for technical training on brain ventricle-targeted electroporation; M. Munchua and V. Yuan for excellent animal care; A. Kriegstein, B. Lu, M. Nachury, J. Reiter, and Guo laboratory members for helpful discussions; D. Larsen,

1.7 FIGURES

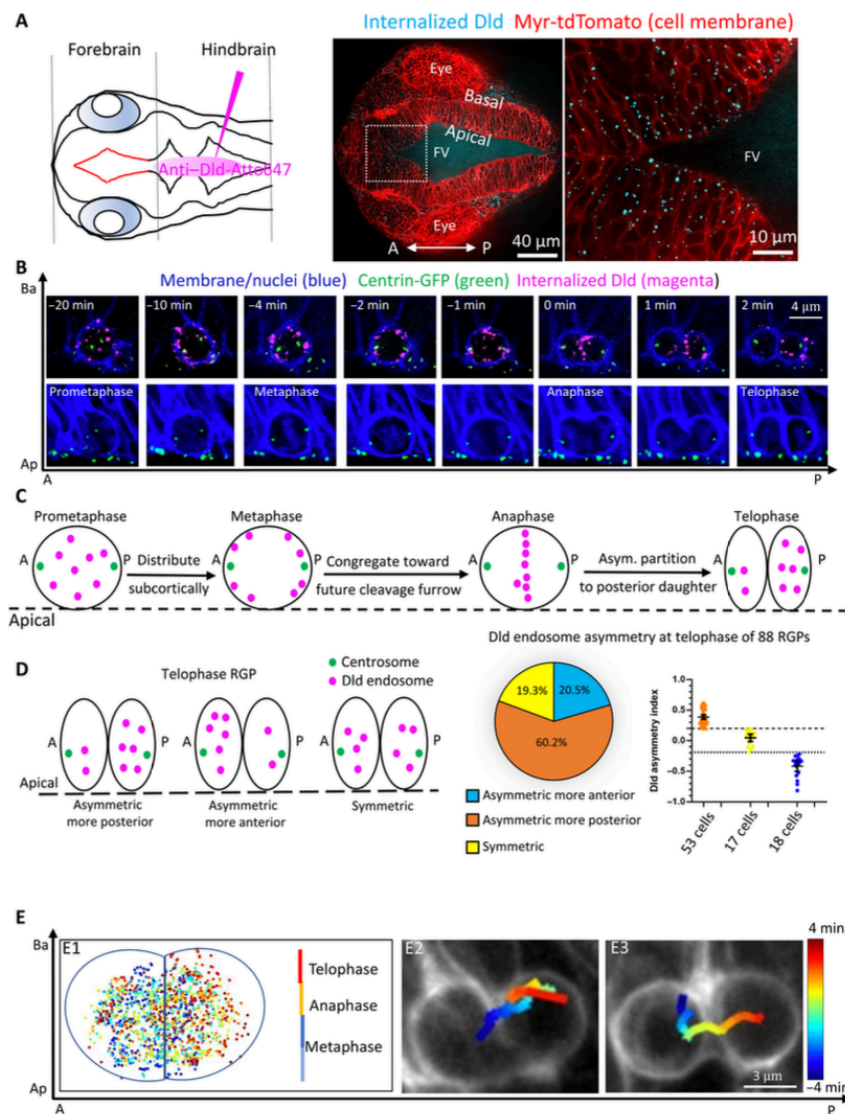


Figure 1.2 Polarized dynamics of notch ligand-containing endosome during RGP division.

(A) Schematic diagram of a 28-hpf embryo (dorsal view) indicating the site of anti-Delta D-Atto647N (Dld) antibody injection (left). Right: Internalized Dld (blue) imaged 2 hours after antibody injection shows punctate appearance in RGPs (membrane labeled red). FV, forebrain ventricle. (B) Time-lapse imaging of mitotic RGP showing the dynamics of labeled Dld endosomes. Membrane, nucleus, and centrosomes [green fluorescent protein (GFP)–centrin] are marked as shown. (C) Schematic diagram showing typical phases of internalized Dld dynamic patterns in (B). (D) Schematic diagrams and statistics of distribution patterns of Dld endosomes in telophase RGPs (see Materials and Methods for the quantification of asymmetry index). Dotted lines in the scatter plot (Figure caption continued on the next page),

(Figure caption continued from the previous page) denote the asymmetric threshold of $|0.2|$. $n = 88$ RGPs, from 20 embryos of six experiments. (E) Automated tracking of Dld endosomes. (E1) Plot of time-lapse data from a composite of 19 RGPs. Each dot represents a tracked endosome at a given time. Color codes for cell cycle stages. The blue vertical line denoting the midpoint between two centrosomes is used for image registration. (E2 and E3) The plot trajectory of a singly labeled Dld endosome in two RGPs. Time is registered and color-coded (anaphase, $T = 0$). A-P, anteroposterior; Ap-Ba, apicobasal. In all images/plots, maximum intensity projection (MIP) of 5- μm z-stacks (1- μm z-step) is shown. The time interval between each z-stack is 12 s.

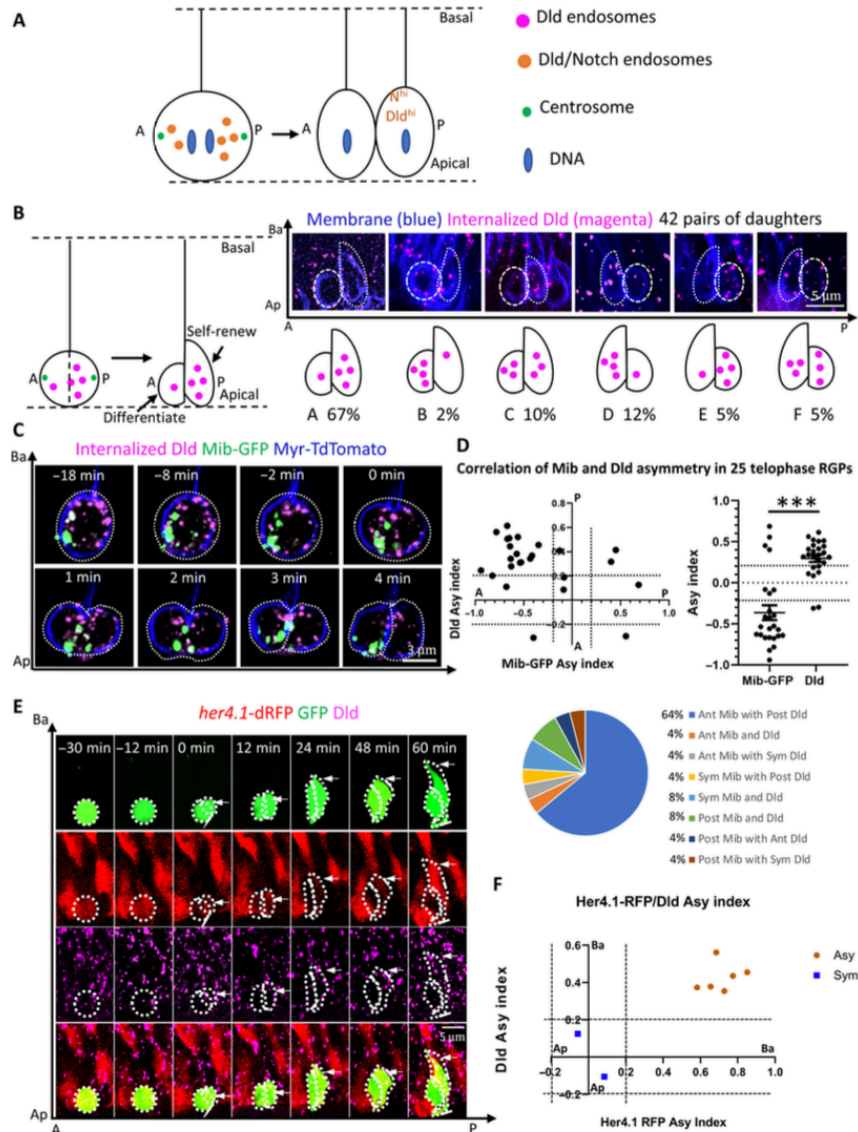


Figure 1.3 Dld endosomes are preferentially segregated into the Notch^{hi} daughter following RGP division.

(A) Schematic depicting the asymmetry of Dld endosomes (Dld^{hi}) and Notch activity (N^{hi}) in daughter cells. (B) Topology and statistics of relative daughter cell position along A-P (anteroposterior) and Ap-Ba (apicobasal) axes after horizontal division. MIP of 5- μ m z-stacks (1- μ m z-step) is shown. (C) Time-lapse images showing that Dld endosomes and Mib are segregated into different daughter cells following RGP division ($n = 25$). MIP of 5- μ m z-stacks (1- μ m z-step) is shown. The time interval between z-stacks is 20 s, and the total acquisition time is 30 min. (D) The top left graph plots individual RGP's asymmetry indices for Mib-GFP (x axis) and internalized Dld (y axis). The top right graph shows the distribution of asymmetry indices for Mib-GFP and Dld endosomes; the dotted lines indicate the threshold of $|0.2|$ for calling asymmetry. *** $P < 0.0001$, $t = 6.549$, $df = 48$, $n = 25$; unpaired two tailed t test. Mean with SEM is shown. The bottom pie chart (Figure caption continued on the next page),

(Figure caption continued from the previous page) shows the percentage of RGPs with indicated distribution patterns. $n = 25$ RGPs, from eight embryos of five repeat experiments. (E) Time-lapse images of a clonally labeled RGP (green) showing preferential segregation of internalized Dld to her4.1-dRFP daughter. MIP of 8- μ m z-stacks (1- μ m z-step) is shown. The time interval between z-stacks is 6 min, and the total acquisition time is ~ 10 hours. (F) Plot for quantifying her4.1-dRFP and internalized Dld in daughter RGPs 1 hour after anaphase. $n = 8$ RGPs, from eight embryos of six repeat experiments.

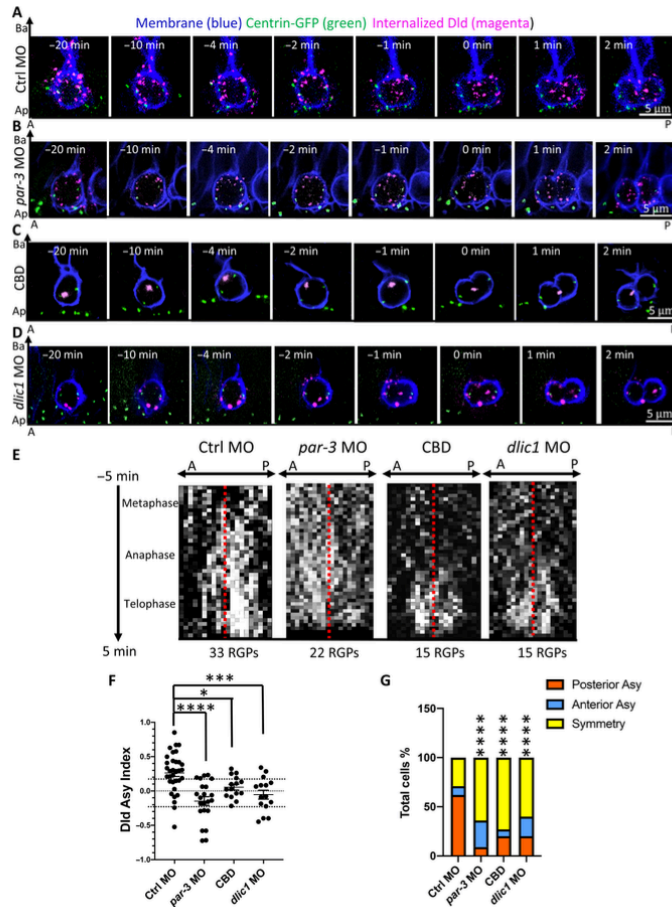


Figure 1.4 Dld endosome asymmetry is dependent on Par-3 and the dynein motor-machinery.

(A to D) Time-lapse sequence of images showing Dld endosome dynamics in mitotic RGP cells from 28-hpf control MO (A) and embryos deficient for *par-3* activity (B), treated with the dynein inhibitor CBD (C), deficient for dynein intermediate light chain 1 (*dlic1*) (D). Centrioles are labeled with GFP-centrin, and membrane is labeled with Myr-TdTomato reporter. For (A) to (D), all images shown are the MIP of five confocal z-stacks (1-μm z-step). The time interval between each volume of z-stacks is 15 s, and the total acquisition time is 25 min. (E) Kymograph of horizontal projection of (A) to (D) showing distribution of all tracked Dld endosomes along the anteroposterior (A-P) axis (x) over time (y). The red line delineates center point of the axis defined by two centrosomes. (F) Scatter plot showing asymmetry indices in telophase RGP cells. Thirty-three control MO RGP cells were from 25 embryos of eight repeat experiments, 22 *par-3* MO RGP cells were from 9 embryos of six repeat experiments, 15 CBD-treated RGP cells were from 7 embryos of four repeat experiments, and 15 *dlic1* MO RGP cells were from 8 embryos of four repeat experiments. The unpaired two tailed t test shows significance between ctrl versus *par-3* MO, **** $P < 0.0001$ ($t = 4.706$, $df = 53$); ctrl MO versus CBD, * $P = 0.0129$ ($t = 2.589$, $df = 46$); ctrl versus *dlic1* MO ** $P = 0.0007$ ($t = 3.645$, $df = 46$). Mean with SEM is shown for each group. (G) Bar graph showing the percentage of RGP cells with different patterns of internalized Dld distribution. Disruption of either Par-3 or dynein activity results in a significant decrease of asymmetric posterior Dld segregation. **** $P < 0.0001$, χ^2 test (chi-square = 95.62, $df = 6$).

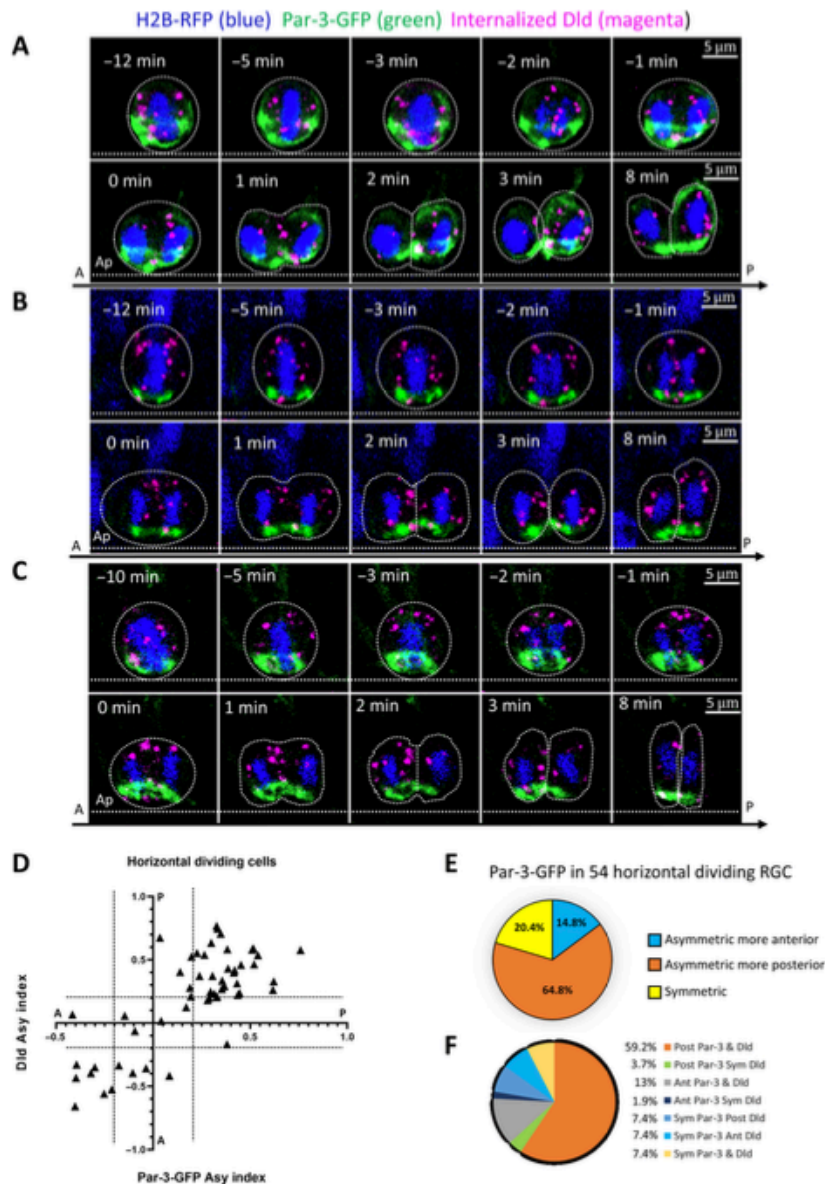


Figure 1.5 Preferential segregation of Par-3 and internalized Dld to the posterior daughter following horizontal RGP division.

Time-lapse sequence of images showing the dynamics of internalized Dld and Par-3-GFP in mitotic RGPs. DNA is marked by H2B-RFP (pseudo-colored in blue). Time=2min denotes telophase when asymmetry indices are calculated. (A) Both internalized Dld and Par-3-GFP are asymmetrically segregated to the posterior daughter shortly after division. (B) Both internalized Dld and Par-3-GFP appear symmetrically distributed shortly after division. (C) Both internalized Dld and Par-3-GFP appear asymmetrically segregated into the anterior daughter shortly after division. For (A) to (C), all images shown are the maximum MIP of five confocal z-stacks (1- μ m z-step). The time interval (Figure caption continued on the next page),

(Figure caption continued from the previous page) between each volume of z-stacks is 30 s, and the total acquisition time is 30 min. (D) Quantification. Left: The asymmetry indices of Par-3-GFP (x axis) and internalized Dld (y axis) in 54 horizontally dividing RGPs. The dotted lines indicate the threshold of $|0.2|$ for calling asymmetry. Right: Pie charts show the percentage of RGPs with different patterns of Par-3-GFP (top), and Par-3-GFP and internalized Dld (bottom) in 54 horizontally dividing RGPs. Most of the RGPs (64.8%) asymmetrically segregate Par-3 to the posterior daughter. Likewise, most of the RGPs (59.2%) asymmetrically segregate both Par-3 and Dld to the posterior daughter. Other minor classes of RGPs displaying different patterns of segregation might reflect real biological heterogeneity or noise due to mosaic nature of Dld labeling. The 54 RGPs are from 15 embryos in eight repeat experiments.

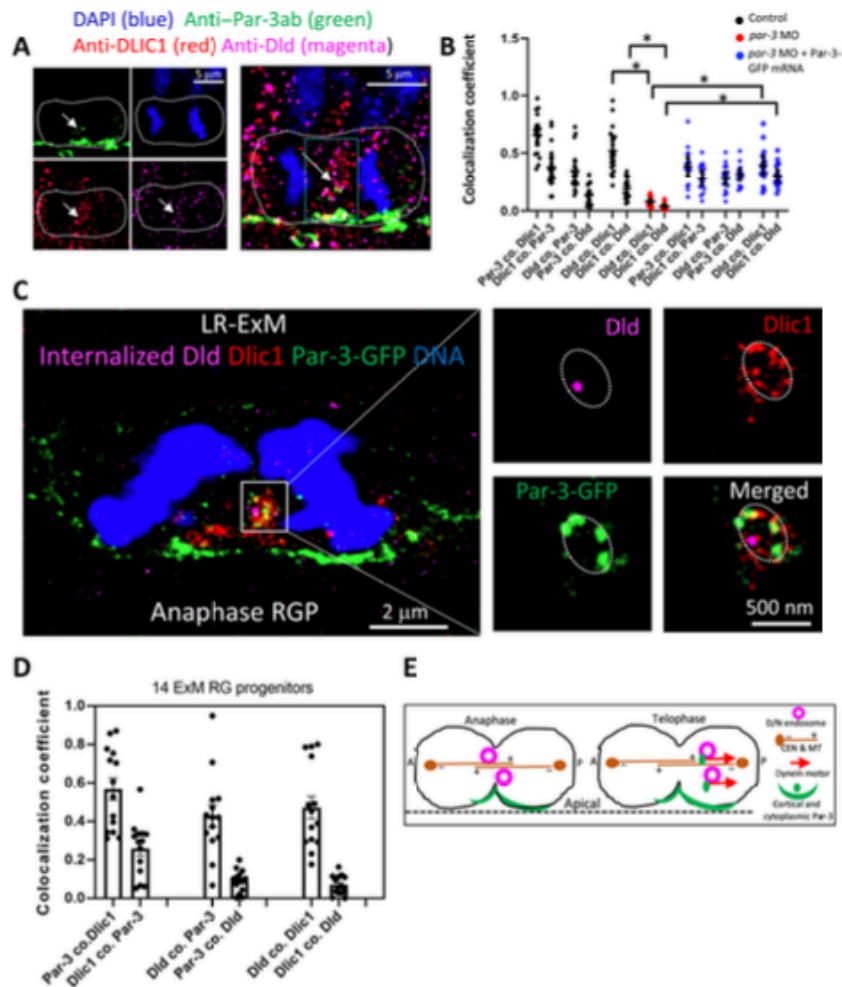


Figure 1.6 Cytosolic Par-3 together with Dlic1 decorates Dld endsomes.

(A) Immunostained anaphase RGP. The green box denotes the area for colocalization analysis (60×100 pixels, $0.126\text{-}\mu\text{m}$ pixel size). The white arrows indicate the overlapped cytosolic staining. The MIP of 10 z-planes ($0.2\text{-}\mu\text{m}$ z-step) is shown. (B) Quantification of colocalization coefficients (see Materials and Methods) in RGPs. Dld and Dlic1 colocalization is significantly reduced in the *par-3*-deficient (*par-3* MO) RGPs ($n = 18$, from six embryos of four repeat experiments) compared with control RGPs ($n = 20$, from five embryos of four repeat experiments). $*P < 0.0001$ (Dld co. Dlic1, $t = 9.56$ and $df = 36$; Dlic1 co. Dld, $t = 7.27$ and $df = 36$), unpaired two-tailed t test. In the *par-3* knockdown RGPs rescued with *Par-3*-GFP mRNA (*par-3* MO + *Par-3*-GFP mRNA, $n = 17$, from eight embryos of four repeat experiments), Dld and Dlic1 colocalizations are significantly restored. $*P < 0.0001$ (Dld co. Dlic1, $t = 8.252$ and $df = 33$; Dlic1 co. Dld, $t = 10.57$ and $df = 33$), unpaired two-tailed t test. Mean with SEM is shown. (C) Left: LR-ExM of anaphase RGP from 28-hpf embryo (*par-3*-GFP mRNA injected at 16-cell stage and anti-Dld-Atto647 uptake at 26 hpf). Scale bars denote the real biological size. The MIP of 10 z-planes is shown. Right: Enlarged view (MIP of four z-planes) of the endosomal structure (dotted ring-like) containing Dld. Z-step = $0.26\text{-}\mu\text{m}$. (D) Statistics of the colocalization coefficient of anti-*Par-3*, anti-Dlic1, and internalized Dld fluorescence in 14 RGPs (from six embryos of four repeat experiments) processed by LR-ExM. (Figure caption continued on the next page),

(Figure caption continued from the previous page) Mean with SEM is shown. (E) Summary model. D/N, delta and Notch; CEN, centrosome; MT, microtubule.

1.8 SUPPLEMENTAL MATERIALS

Supplementary materials and methods In vivo co-immunoprecipitation (co-IP) ~ 100 embryos at 2dpf were collected for preparing each lysate sample. The embryos were placed in the Eppendorf tube with 1mL modified Ringer's solution (116 mM NaCl, 3 mM KCl, 4 mM CaCl₂, 5 mM HEPES; pH 7.5) containing Protease Inhibitor (Roche, Cat. No. 04693132001) and Phosstop (Roche, Cat. No. 04906845001). After incubation at room temperature on the shaker for 10 min. supernatant was removed the liquid and 0.3 ml lysis buffer (50 mM Tris pH 7.5, 150 mM NaCl, 1 mM EDTA, 10% glycerol, 1% Triton X-100) with Protease Inhibitor and Phosstop was added. The tube was kept on ice, and the embryos were homogenized manually by pumping through the syringe with 22-gauge needles for over 20 times. After homogenization, the tube was placed on the shaker in ice for over 30 minutes. Then the tube was centrifuged for 30 minutes at 10,000 g at 4 °C, and the supernatant was transferred to fresh tube for the following experiment. SureBeads™ Protein A Magnetic Beads were used for co-IP with anti-Dlic antibody and anti-Par-3 antibody. SureBeads™ Protein G Magnetic Beads were used for the co-IP with anti-Dld antibody. The beads were thoroughly resuspended before use; 150 µl beads were transferred to 1.5 ml tubes. After washing with 1ml PBS-T (PBS + 0.1% Tween 20), 200 µl PBS-T with 2 µg antibody was added to resuspend the beads. After rotating for 2 hours at room temperature (RT), magnetized beads were collected and supernatant was discarded. The antibody-conjugated beads were then washed with 1ml PBS-T for three times and added to the 300 µl embryonic lysate prepared above. After incubation on the rotor at 4 °C for overnight, magnetized beads were collected and supernatant was discarded, followed by five times wash with 1ml PBS-T. Before the last magnetization, the resuspended beads were transferred to a new tube and centrifuged for several seconds. Beads were then collected on a magnet and residual buffer was aspirated from the tube. 40 µl 1x Laemmli buffer was added to the beads and incubated for 10 min at 70°C. Eluents were then transferred to a new tube. Final collected

samples were boiled at 99°C for 10 min before running SDS-PAGE, or storage at -20 °C.

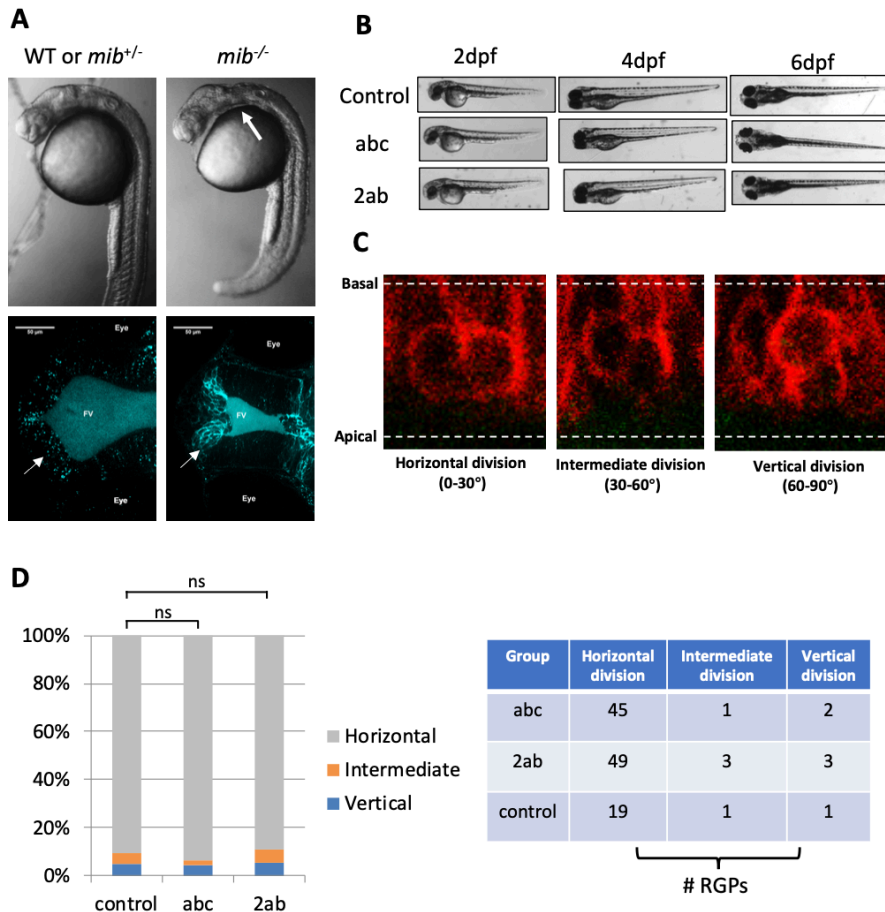


Figure S1.1 In vivo antibody uptake assay labels endocytosed notch ligand Dld without affecting cell division patterns and embryonic development.

(A) morphological (top) and confocal images (bottom) showing impaired Dld internalization in 24 hpf *mib*^{-/-} embryo. Since Mib is essential for Dld endocytosis, this demonstrates that the internalized Dld labels Dld endosomes. Similar results are observed in 5 embryos for each condition. The maximum intensity projection of 10 confocal z-stacks (1 μm z-step) are shown. (B) Morphological images showing grossly normal development of control, abc (injected with the dye-labeled secondary antibody conjugated anti-Dld), and 2ab (injected with the dye-labeled secondary antibody only) embryos at 2 dpf, 4 dpf and 6 dpf (days post fertilization). Similar results are observed in 5 embryos for (Figure caption continued on the next page),

(Figure caption continued from the previous page) each condition. (C) Confocal images showing different orientations of division in mitotic RGPs from ~28 hpf embryos (horizontal division: the angle between the division axis and apical surface is between 0-300; non- horizontal division includes intermediate division-the angle between the division axis and apical surface is between 30-600 and vertical division-the angle between the division axis and apical surface is between 60- 900). The maximum intensity projection of 5 confocal z-stacks (1 μm z-step) are shown. (D) Statistical graph showing percent division modes of RGPs from ~28 hpf embryos in control, abc, and 2ab. Majority of RGPs undergo horizontal division. Normal (z) test for proportions (implemented by Python statsmodels package) shows no statistical difference between control group and any of the other two groups. Control vs abc (Proportions of Horizontal division): z score = -0.483, P = 0.629; control vs abc (Proportions of Intermediate division): z score = 0.610, P = 0.542; control vs abc (Proportions of Vertical division): z score = 0.112, P = 0.911; control vs 2ab (Proportions of Horizontal division): z score = 0.176, P = 0.860; control vs 2ab (Proportions of Intermediate division): z score = -0.121, P = 0.904; control vs 2ab (Proportions of Vertical division): z score = -0.121, P = 0.904.

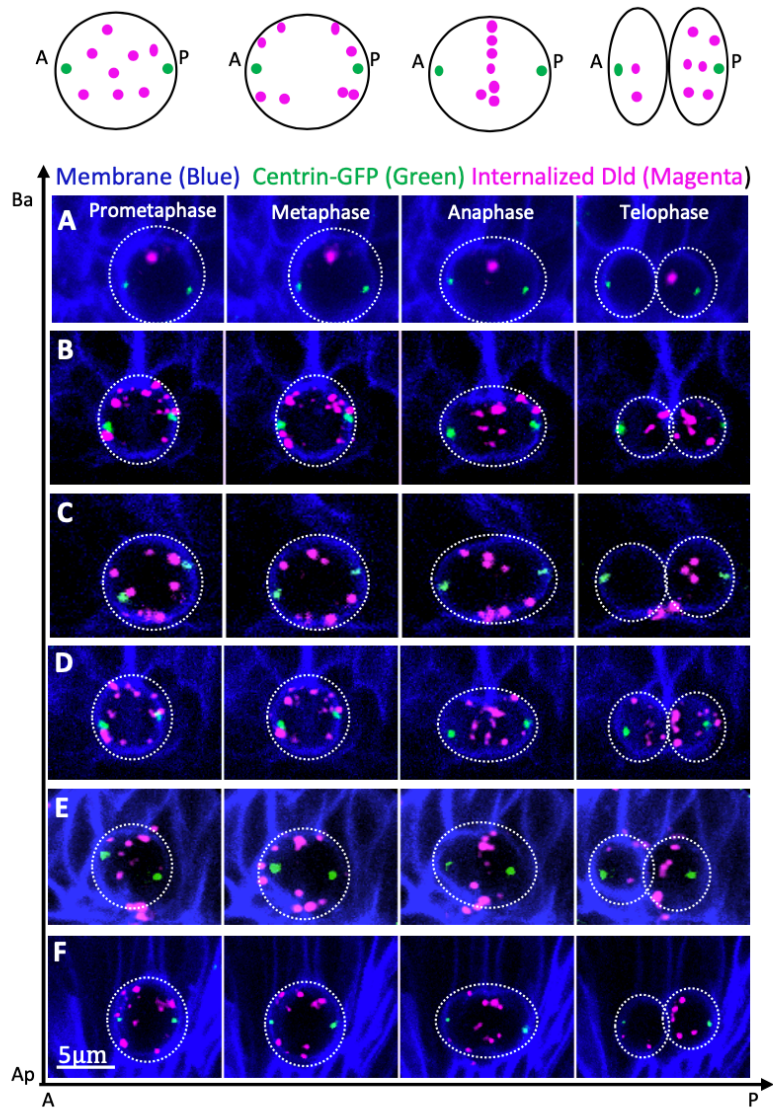


Figure S1.2 In vivo time-lapse sequences of images show the dynamics of DId endosomes in 6 additional mitotic RGP.

(Top) Schematic map showing the DId endosome dynamics during the cell cycle at different phases. (A-F) six mitotic RGP. Membrane is marked with Myr-TdTomato (pseudo-colored blue). Centrosome is marked with GFP-Centrin. The maximum intensity projection of 5 confocal z-stacks (1 μm z-step) are shown. The time interval between each volume of z-stacks is 12 sec and the total acquisition time is 25 min.

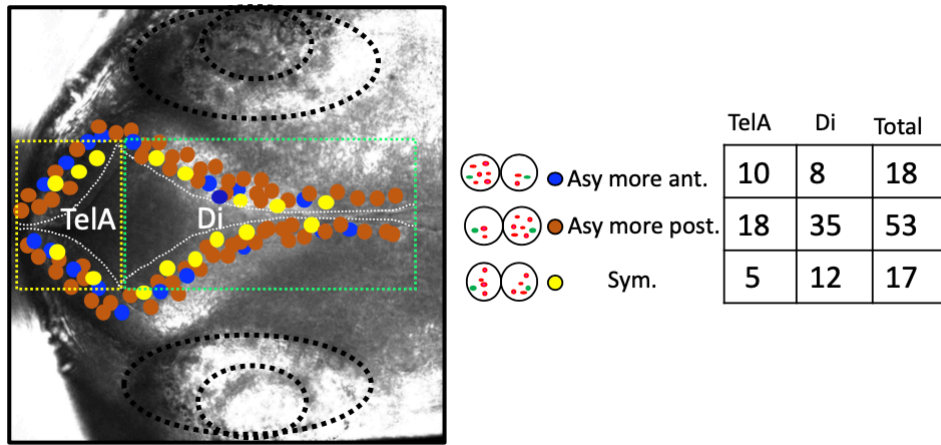


Figure S1.3 Spatial distributions of imaged telophase RGPs in the embryonic forebrain.

Bright-field image of 28 hpf embryonic forebrain. The position of RGPs (n=88, selected from 20 different embryos) surrounding the forebrain ventricle was plotted. These RGPs were included in the statistics of Figure 1D. TelA, telencephalic anterior part of the ventricle; Di, diencephalic part of the ventricle.

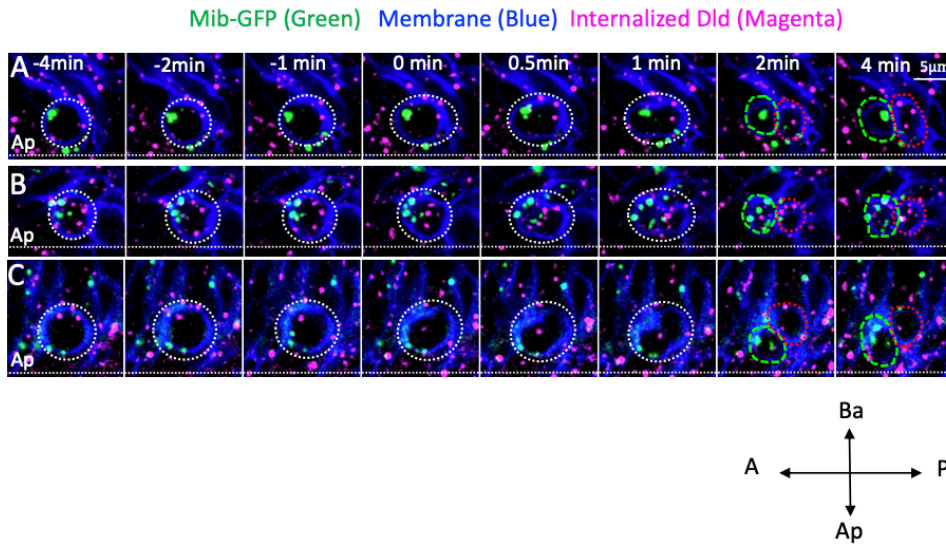


Figure S1.4 Mib and DId endosomes preferentially segregate into different daughter cells in 3 additional mitotic RGPs.

(A-C) In vivo time-lapse sequence of images showing three mitotic RGPs, with more Mib-GFP in the anterior daughter and more DId endosomes in the posterior daughter. The membrane is marked with Myr-TdTomato (pseudo-colored blue). The maximum intensity projection of 5 confocal z- stacks (1 µm z-step) are shown. The time interval between each volume of z-stacks is 20 sec and the total acquisition time of the whole set is 30 min.

Symmetric Her4.1-dRFP and Dld-Atto 647 in the pair of daughter cells

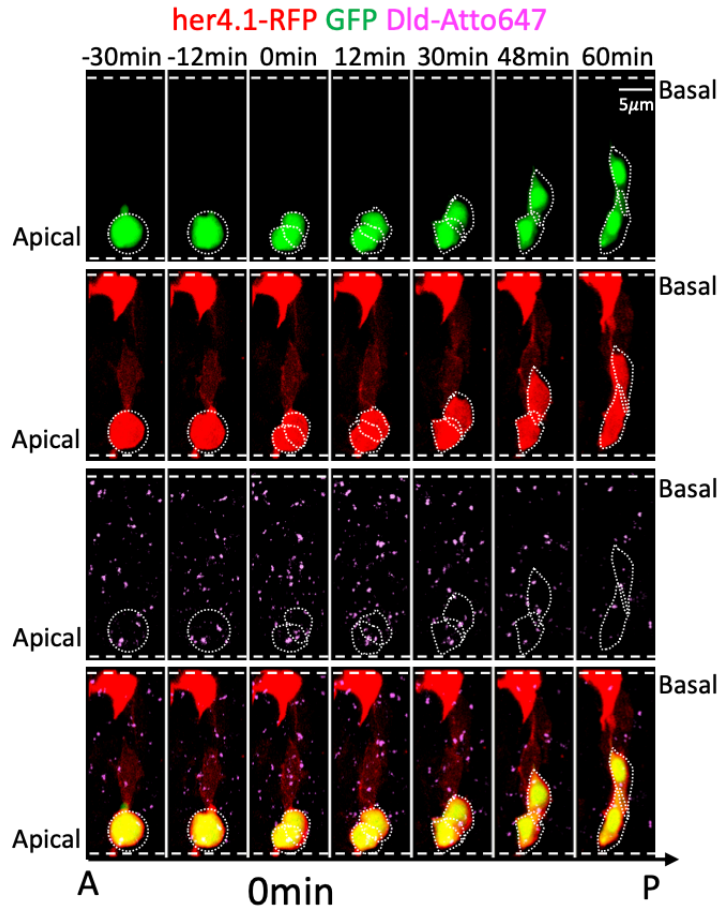


Figure S1.5 An Example of Paired Daughter Cell with Symmetric Dld and Her4.1-RFP Dynamics.

In vivo time-lapse sequence of images showing a sparsely GFP-labeled mitotic RGP with internalized Dld in Tg[her4.1-dRFP] embryo. The maximum intensity projection of 8 confocal z-stacks (1 μm z-step) are shown. The time interval between each volume of z-stacks is 6 min and the total acquisition time is 12 hours.

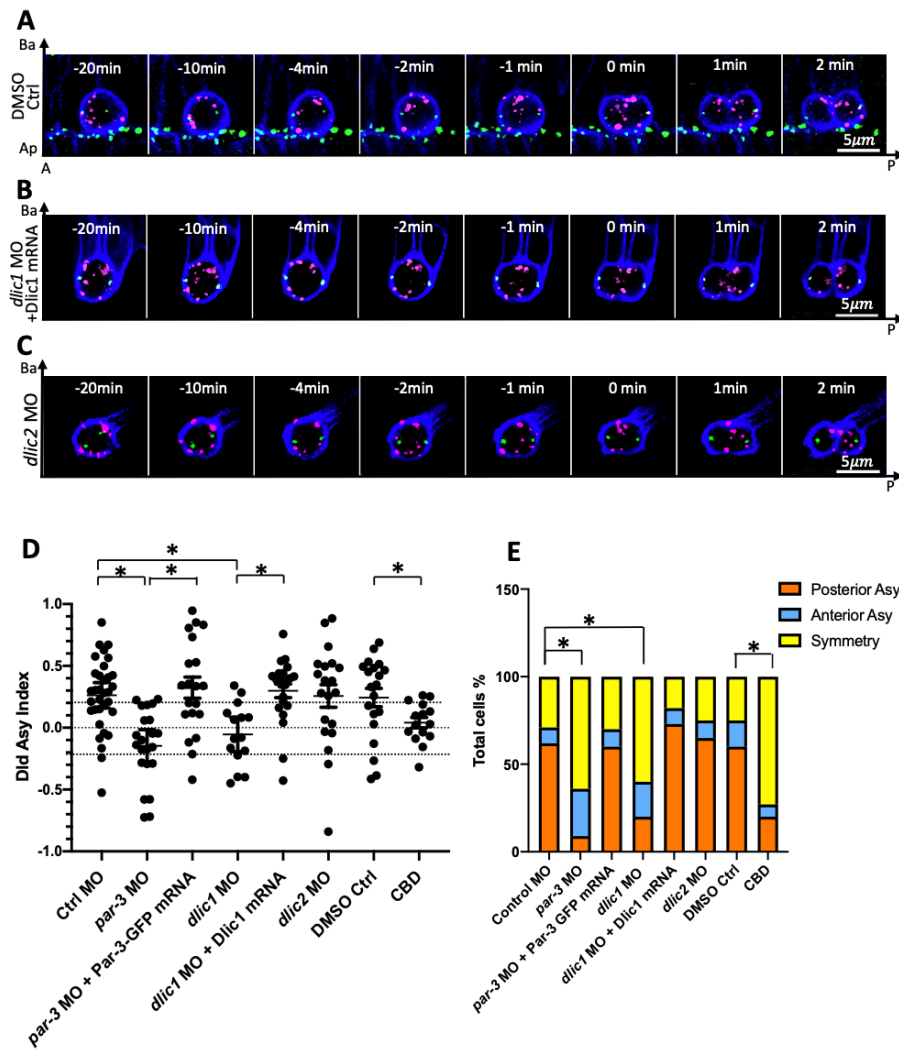


Figure S1.6 Rescue of Par-3 and Dlic1 Morphant Phenotypes by Par-3-GFP and Dlic1 mRNAs Respectively.

(A-C) Time-lapse sequence of images showing directional posterior asymmetric Dld endosome dynamics in mitotic RGPs from 28 hpf DMSO control embryos (A), *dlic1* morphant rescued by Dlic1 mRNA embryos (B), and *dlic2* morphant embryos (C). Centrosomes are labeled with GFP-Centrin and membrane is labeled with Myr-TdTomato reporter. For (A-C), all images shown are the maximum intensity projection of 5 confocal z-stacks (1 μ m z-step). The time interval between each volume of z-stacks is 15 sec and the total acquisition time is 25 min. (D) Scatter plot showing asymmetry indices of internalized Dld in telophase RGPs. They are significantly different between the control MO RGPs (n=34, from 25 embryos of 8 repeat experiments) and *par-3* MO RGPs (n=22, from 9 embryos of 6 repeat experiments; * $P < 0.001$, $t = 5.087$, $df = 53$, unpaired two-tailed t-test); control MO and *dlic1* MO RGPs (n=15, from 7 embryos of 4 repeat experiments; * $P < 0.001$, $t = 3.645$, $df = 46$, unpaired two-tailed t-test). The RGPs of *par-3* MO + Par-3-GFP mRNA injected groups (n=20, from 6 embryos of 4 repeat experiments) are significantly different from the *par-3* MO RGPs (* $P < 0.001$, $t = 4.494$, $df = 40$, unpaired two-tailed t-test). The RGPs of *dlic1* MO + Dlic1 mRNA (Figure caption continued on the next page),

(Figure caption continued from the previous page) injected groups (n=22, from 7 embryos of 4 repeat experiments) are significantly different from the dlic1 MO RGP (* P<0.001, t =4.092, df =35, unpaired two-tailed t-test). The RGP of dlic2 MO injected groups (n=20, from 6 embryos of 3 repeat experiments) and DMSO control groups (n=20, from 5 embryos of 4 repeat experiments) did not exhibit any significant differences from Ctrl MO RGP. The RGP of CBD treated groups (n=15, from 7 embryos of 4 repeat experiments) are significantly different from DMSO control group (* P<0.05, t = 2.176, df = 33, unpaired two-tailed t-test). Mean with SEM is shown for each group. € Bar graph representation of the data in (A), showing the percentage of RGP with different Dld endosome segregation patterns. Disruption of either par-3 or dlic1 activity results in a significant decrease of RGP with posterior segregation of Dld endosomes, which can be rescued by Par-3-GFP or Dlic1 mRNAs respectively. Disruption of dlic2 activity has not changed Dld endosome segregation patterns (P = 0.8107, χ^2 test, df=2). The par-3 MO and dlic1 MO groups are significantly different from control MO (*P < 0.001, χ^2 test, df=2), whereas either par-3 MO+Par-3-GFP mRNA or Dlic1 MO+Dlic1 mRNA group showed no difference from control MO (P = 0.2839, χ^2 test, df=2). CBD treated group is significantly different from DMSO control group (*P < 0.001, χ^2 test, df=2).

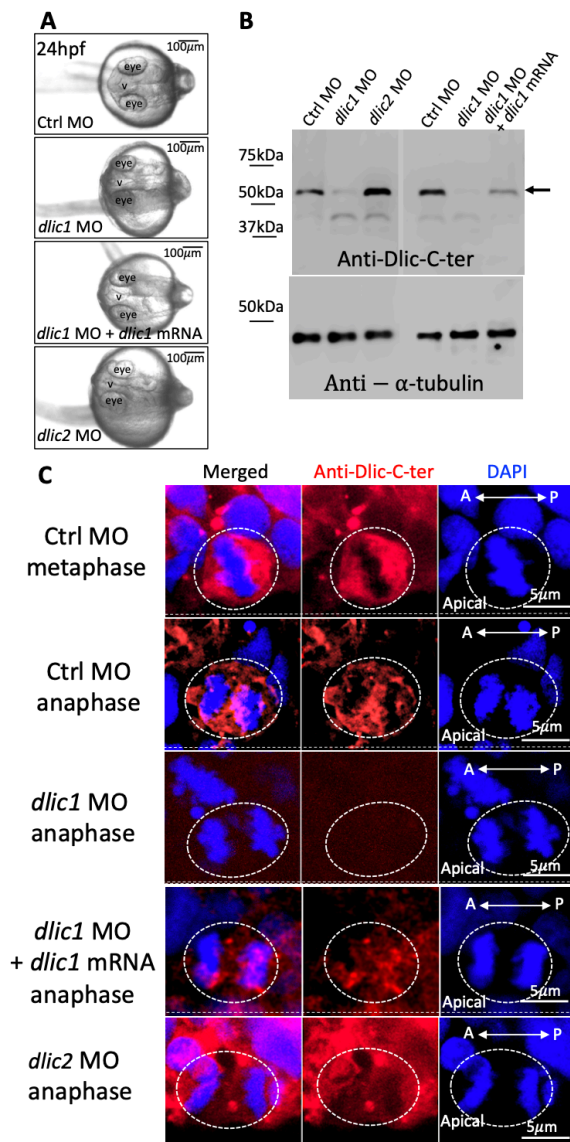


Figure S1.7 The Dlic1 Isoform is expressed in mitotic RGPs and can be effectively knocked down using morpholinos antisense oligonucleotides.

(A) Morphological images (left) showing that both *dlic1* and *dlic2* MO knockdown reduced the overall size of embryos at 24 hpf (n=30 embryos for each group). The *dlic1* MO plus *dlic1* mRNA injected embryos are comparable to Control MO-injected ones, indicating functional rescue. (B) Western blotting (right) using an anti-Drosophila Dlic-C-ter antibody showing a band at the expected size of zebrafish Dlic proteins (~54 kDa). The intensity of the band is significantly decreased in *dlic1* MO but increased in *dlic2* MO, indicating that the antibody recognizes the Dlic1 protein in zebrafish. A small minor band of unknown identity is also detected at ~40 kDa. (C) IF labeling of mitotic RGPs in 28 hpf embryo showing staining with anti-Drosophila Dlic-C-ter antibody that specifically recognizes zebrafish Dlic1 as shown above. Immunoreactivity is observed in control MO (15 metaphase and 8 anaphase RGPs from 6 embryos of two repeat experiments), *dlic1* MO injected with MO-insensitive *dlic1* mRNA (12 metaphase and 6 anaphase RGPs from 6 embryos of three repeat experiments, only anaphase RGP is shown), and *dlic2* MO (Figure caption continued on the next page),

(Figure caption continued from the previous page) (6 anaphase RGPs from 4 embryos), but lost in *dlic1* MO (10 metaphase and 5 anaphase RGPs from 5 embryos of three repeat experiments, only anaphase RGP is shown), indicating that the antibody specifically recognizes Dlic1 isoform in mitotic RGPs. Maximum intensity projection of 20-25 confocal z-stacks (0.26 μm z-step) are shown.

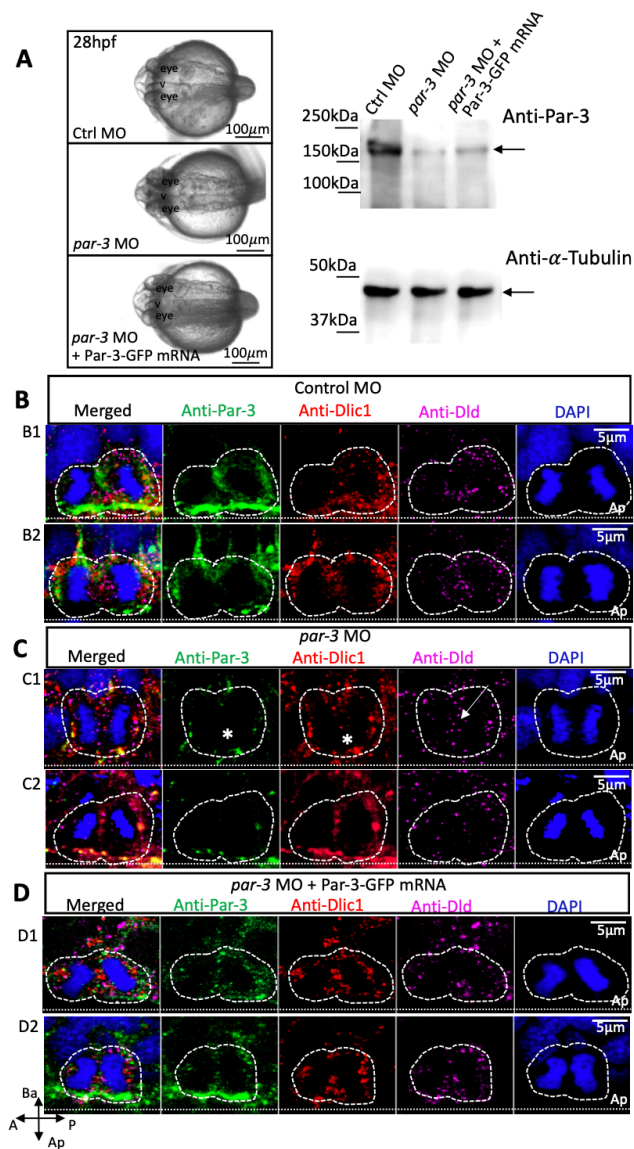


Figure S1.8 Validation of Anti-Par-3 Antibody and Immunofluorescence Labeling (IF)

(A) Left: Morphological images showing *par-3* MO knockdown induced brain defects in 28 hpf embryos ($n=30$ embryos for each group). The *par-3* morphants injected with MO-insensitive Par-3-GFP mRNA are morphologically similar to control MO-injected embryos. Right: Western blotting using the anti-Par-3 antibody showing a band at the expected Par-3 protein size of ~150 kDa. The intensity of the band is decreased in *par-3* MO group but increased in *par-3* MO injected with Par-3-GFP mRNA, indicating that the antibody recognizes the Par-3 protein in zebrafish. (B) IF labeling with anti-Par-3, anti-Dlic1, and anti-Dld in mitotic RGPs from control MO-injected 28 hpf embryo. Two representative RGPs are shown (B1 and B2). (C) IF labeling of RGPs in *par-3* MO injected embryos showing the loss of Par-3 immunoreactivity. Two representative RGPs are shown (C1 and C2). (D) IF labeling of RGPs in embryos co-injected with *par-3* MO and Par-3-GFP mRNA. Two representative RGPs are shown (D1 and D2). For (B-D), maximum intensity projections of 10 confocal z-stacks (0.26 μ m z-step) are shown. Mitotic RGPs are outlined according to the cytoplasmic staining of anti-Dlic1 and anti-Par-3 antibodies.

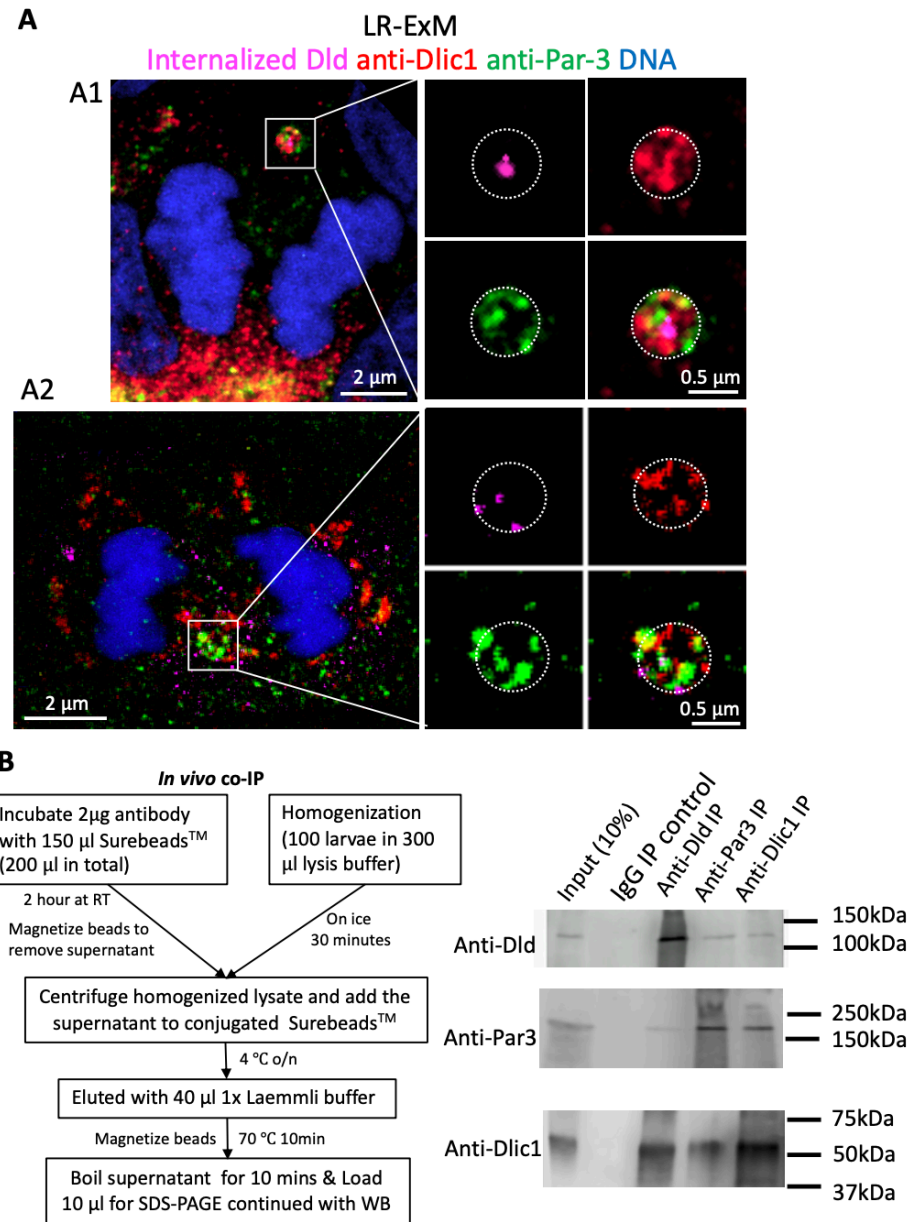


Figure S1.9 Endogenous Par-3 and Dlic1 Associate with Dld Endosomes in mitotic RGPs.

(A) LR-ExM of RGPs (A1 and A2) showing the co-localization of internalized Dld, anti-Dlic1, and anti-Par-3 on a ring-shaped endosome (outlined with dotted lines) at anaphase (expanded 4-fold). The scale bars denote the real biological size prior to expansion. The maximum intensity projection of 5 confocal z-stacks (0.26 μm z-step) are shown. (B) (Left) Flow chart showing the steps of *in vivo* co-immunoprecipitation (co-IP) using 1-2-day old zebrafish embryos. (Right) co-IP results with anti-Dld, anti-Par-3 and anti-Dlic1 antibodies. The input (10%) is the lysate sample made from 20 embryos without IP. The IgG IP serves as a negative control. For the anti-Dld and anti-Par-3 western blotting, 25 μl of anti-Dld IP sample and 10 μl of other IP samples are loaded on the gel. For the anti-Dlic1 western blotting, 5 μl of anti-Dlic1 IP sample and 10 μl of other IP samples are loaded on the gel.

1.9 REFERENCES

1. K. J. Yong, B. Yan, The relevance of symmetric and asymmetric cell divisions to human central nervous system diseases. *J. Clin. Neurosci.* 18, 458–463 (2011).
2. M. C. Florian, H. Geiger, Concise review: Polarity in stem cells, disease, and aging. *StemCells* 28, 1623–1629 (2010).
3. V. Aranda, M. E. Nolan, S. K. Muthuswamy, Par complex in cancer: A regulator of normal cell polarity joins the dark side. *Oncogene* 27, 6878–6887 (2008).
4. M. C. Wagner, B. A. Molitoris, Renal epithelial polarity in health and disease. *Pediatr. Nephrol.* 13, 163–170 (1999).
5. S. Guo, K. J. Kemphues, Molecular genetics of asymmetric cleavage in the early *Caenorhabditis elegans* embryo. *Curr. Opin. Genet. Dev.* 6, 408–415 (1996).
6. K. J. Kemphues, J. R. Priess, D. G. Morton, N. S. Cheng, Identification of genes required for cytoplasmic localization in early *C. elegans* embryos. *Cell* 52, 311–320 (1988).
7. L. S. Rose, K. J. Kemphues, Early patterning of the *C. elegans* embryo. *Annu. Rev. Genet.* 32, 521–545 (1998).
8. B. Goldstein, I. G. Macara, The PAR proteins: Fundamental players in animal cell polarization. *Dev. Cell* 13, 609–622 (2007).

9. F. Motegi, G. Seydoux, The PAR network: Redundancy and robustness in a symmetry-breaking system. *Philos. Trans. R. Soc. Lond. B Biol. Sci.* 368, 20130010 (2013).
10. C. Hoegel, A. A. Hyman, Principles of PAR polarity in *Caenorhabditis elegans* embryos. *Nat. Rev. Mol. Cell Biol.* 14, 315–322 (2013).
11. F. Peglion, N. W. Goehring, Switching states: Dynamic remodelling of polarity complexes as a toolkit for cell polarization. *Curr. Opin. Cell Biol.* 60, 121–130 (2019).
12. M. Inaba, Y. M. Yamashita, Asymmetric stem cell division: Precision for robustness. *Cell Stem Cell* 11, 461–469 (2012).
13. C. C. Homem, M. Repic, J. A. Knoblich, Proliferation control in neural stem and progenitor cells. *Nat. Rev. Neurosci.* 16, 647–659 (2015).
14. E. Taverna, M. Götz, W. B. Huttner, The cell biology of neurogenesis: Toward an understanding of the
15. C. Q. Doe, Neural stem cells: Balancing self-renewal with differentiation. *Development* 135, 1575–1587 (2008).
16. D. Delaunay, A. Kawaguchi, C. Dehay, F. Matsuzaki, Division modes and physical asymmetry in cerebral cortex progenitors. *Curr. Opin. Neurobiol.* 42, 75–83 (2017).

17. F. Schweisguth, Asymmetric cell division in the *Drosophila* bristle lineage: From the polarization of sensory organ precursor cells to notch-mediated binary fate decision. *Wiley Interdiscip. Rev. Dev. Biol.* 4, 299–309 (2015).
18. B. Lu, L. Jan, Y. N. Jan, Control of cell divisions in the nervous system: Symmetry and asymmetry. *Annu. Rev. Neurosci.* 23, 531–556 (2000).
19. P. Alexandre, A. M. Reugels, D. Barker, E. Blanc, J. D. Clarke, Neurons derive from the more apical daughter in asymmetric divisions in the zebrafish neural tube. *Nat. Neurosci.* 13, 673–679 (2010).
20. Z. Dong, N. Yang, S.-Y. Yeo, A. Chitnis, S. Guo, Intralineaage directional Notch signaling regulates self-renewal and differentiation of asymmetrically dividing radial glia. *Neuron* 74, 65–78 (2012).
21. S. Singh, D. J. Solecki, Polarity transitions during neurogenesis and germinal zone exit in the developing central nervous system. *Front. Cell. Neurosci.* 9, 62 (2015).
22. W. A. Liu, S. Chen, Z. Li, C. H. Lee, G. Mirzaa, W. B. Dobyns, M. E. Ross, J. Zhang, S. H. Shi, PARD3 dysfunction in conjunction with dynamic HIPPO signaling drives cortical enlargement with massive heterotopia. *Genes Dev.* 32, 763–780 (2018).
23. F. Coumilleau, M. Fürthauer, J. A. Knoblich, M. González-Gaitán, Directional Delta and Notch trafficking in Sara endosomes during asymmetric cell division. *Nature* 458, 1051–1055 (2009).

24. E. Derivery, C. Seum, A. Daeden, S. Loubéry, L. Holtzer, F. Jülicher, M. Gonzalez-Gaitan, Polarized endosome dynamics by spindle asymmetry during asymmetric cell division. *Nature* 528, 280–285 (2015).
25. S. Kressmann, C. Campos, I. Castanon, M. Fürthauer, M. González-Gaitán, Directional Notch trafficking in Sara endosomes during asymmetric cell division in the spinal cord. *Nat. Cell Biol.* 17, 333–339 (2015).
26. K. Mizutani, K. Yoon, L. Dang, A. Tokunaga, N. Gaiano, Differential Notch signalling distinguishes neural stem cells from intermediate progenitors. *Nature* 449, 351–355 (2007).
27. R. S. Bultje, D. R. Castaneda-Castellanos, L. Y. Jan, Y. N. Jan, A. R. Kriegstein, S. H. Shi, Mammalian Par3 regulates progenitor cell asymmetric division via notch signaling in the developing neocortex. *Neuron* 63, 189–202 (2009).
28. S. E. Williams, S. Beronja, H. A. Pasolli, E. Fuchs, Asymmetric cell divisions promote Notch-dependent epidermal differentiation. *Nature* 470, 353–358 (2011).
29. S. Artavanis-Tsakonas, M. Rand, R. Lake, Notch signaling: Cell fate control and signal integration in development. *Science* 284, 770–776 (1999).
30. N. Gaiano, G. Fishell, The role of notch in promoting glial and neural stem cell fates. *Annu. Rev. Neurosci.* 25, 471–490 (2002).

31. E. Munro, Protein clustering shapes polarity protein gradients. *Dev. Cell* 42, 309–311 (2017).
32. S. C. Noctor, A. C. Flint, T. A. Weissman, R. S. Dammerman, A. R. Kriegstein, Neurons derived from radial glial cells establish radial units in neocortex. *Nature* 409, 714–720 (2001).
33. A. Kriegstein, A. Alvarez-Buylla, The glial nature of embryonic and adult neural stem cells. *Annu. Rev. Neurosci.* 32, 49–84 (2009).
34. K. Tong, M. Wagle, S. Guo, Antibody uptake assay in the embryonic zebrafish forebrain to study notch signaling dynamics in neural progenitor cells in vivo. *Methods Mol. Biol.* 1576, 273–281 (2019).
35. M. Itoh, C. H. Kim, G. Palardy, T. Oda, Y. J. Jiang, D. Maust, S. Y. Yeo, K. Lorick, G. J. Wright, L. Ariza-McNaughton, A. M. Weissman, J. Lewis, S. C. Chandrasekharappa, A. B. Chitnis, Mind bomb is a ubiquitin ligase that is essential for efficient activation of Notch signaling by Delta. *Dev. Cell* 4, 67–82 (2003).
36. X. Shi, Q. Li, Z. Dai, A. Tran, S. Feng, A. D. Ramirez, Z. Lin, X. Wang, T. T. Chow, I. B. Seiple, B. Huang, Label-retention expansion microscopy. *BioRxiv* 2019, 687954 (2019).
37. S. Tozer, C. Baek, E. Fischer, R. Gojame, X. Morin, Differential routing of Mindbomb1 via centriolar satellites regulates asymmetric divisions of neural progenitors. *Neuron* 93, 542–551.e4 (2017).

38. S. Y. Yeo, M. Kim, H. S. Kim, T. L. Huh, A. B. Chitnis, Fluorescent protein expression driven by her4 regulatory elements reveals the spatiotemporal pattern of Notch signaling in the nervous system of zebrafish embryos. *Dev. Biol.* 301, 555–567 (2007).
39. Z. Dong, M. Wagle, S. Guo, Time-lapse live imaging of clonally related neural progenitor cells in the developing zebrafish forebrain. *J. Vis. Exp.* 2011, 2594 (2011).
40. B. Etemad-Moghadam, S. Guo, K. J. Kemphues, Asymmetrically distributed PAR-3 protein contributes to cell polarity and spindle alignment in early *C. elegans* embryos. *Cell* 83, 743–752 (1995).
41. M. Tawk, C. Araya, D. A. Lyons, A. M. Reugels, G. C. Girdler, P. R. Bayley, D. R. Hyde, M. Tada, J. D. W. Clarke, A mirror-symmetric cell division that orchestrates neuroepithelial morphogenesis. *Nature* 446, 797–800 (2007).
42. A. J. Blasky, L. Pan, C. B. Moens, B. Appel, Pard3 regulates contact between neural crest cells and the timing of schwann cell differentiation but is not essential for neural crest migration or myelination. *Dev. Dyn.* 243, 1511–1523 (2014).
43. A. Rossi, Z. Kontarakis, C. Gerri, H. Nolte, S. Hölper, M. Krüger, D. Y. R. Stainier, Genetic compensation induced by deleterious mutations but not gene knockdowns. *Nature* 524, 230–233 (2015).
44. J. Schmoranzer, J. P. Fawcett, M. Segura, S. Tan, R. B. Vallee, T. Pawson, G. G. Gundersen, Par3 and dynein associate to regulate local microtubule dynamics and centrosome

orientation during migration. *Curr. Biol.* 19, 1065–1074 (2009).

45. S. Mische, Y. He, L. Ma, M. Li, M. Serr, T. S. Hays, Dynein light intermediate chain: An essential subunit that contributes to spindle checkpoint inactivation. *Mol. Biol. Cell* 19, 4918–4929 (2008).

46. J. H. Yoder, M. Han, Cytoplasmic dynein light intermediate chain is required for discrete aspects of mitosis in *Caenorhabditis elegans*. *Mol. Biol. Cell* 12, 2921–2933 (2001).

47. S. H. Tynan, A. Purohit, S. J. Doxsey, R. B. Vallee, Light intermediate chain 1 defines a functional subfraction of cytoplasmic dynein which binds to pericentrin. *J. Biol. Chem.* 275, 32763–32768 (2000).

48. S. L. Reck-Peterson, W. B. Redwine, R. D. Vale, A. P. Carter, The cytoplasmic dynein transport machinery and its many cargoes. *Nat. Rev. Mol. Cell Biol.* 19, 382–398 (2018).

49. S. Mahale, M. Kumar, A. Sharma, A. Babu, S. Ranjan, C. Sachidanandan, S. V. S. Mylavarapu, The light intermediate chain 2 subpopulation of dynein regulates mitotic spindle orientation. *Sci. Rep.* 6, 22 (2016).

50. D. Satoh, D. Sato, T. Tsuyama, M. Saito, H. Ohkura, M. M. Rolls, F. Ishikawa, T. Uemura, Spatial control of branching within dendritic arbors by dynein-dependent transport of Rab5-endosomes. *Nat. Cell Biol.* 10, 1164–1171 (2008).

51. C. P. Horgan, S. R. Hanscom, R. S. Jolly, C. E. Futter, M. W. McCaffrey, Rab11-FIP3 links

the Rab11 GTPase and cytoplasmic dynein to mediate transport to the endosomal- recycling compartment. *J. Cell Sci.* 123, 181–191 (2010).

52. A. Wodarz, A. Ramrath, U. Kuchinke, E. Knust, Bazooka provides an apical cue for Inscuteable localization in *Drosophila* neuroblasts. *Nature* 402, 544–547 (1999).

53. M. Schober, M. Schaefer, J. A. Knoblich, Bazooka recruits Inscuteable to orient asymmetric cell divisions in *Drosophila* neuroblasts. *Nature* 402, 548–551 (1999).

54. S. Bolte, F. P. Cordelières, A guided tour into subcellular colocalization analysis in light microscopy. *J. Microsc.* 224, 213–232 (2006).

55. F. Chen, P. W. Tillberg, E. S. Boyden, Expansion microscopy. *Science* 347, 543–548 (2015).

56. P. W. Tillberg, F. Chen, K. D. Piatkevich, Y. Zhao, C. C. Yu, B. P. English, L. Gao, A. Martorell, H. J. Suk, F. Yoshida, E. M. DeGennaro, D. H. Roossien, G. Gong, U. Seneviratne, S. R. Tannenbaum, R. Desimone, D. Cai, E. S. Boyden, Protein-retention expansion microscopy of cells and tissues labeled using standard fluorescent proteins and antibodies. *Nat. Biotechnol.* 34, 987–992 (2016).

57. J. Betschinger, K. Mechtler, J. A. Knoblich, The Par complex directs asymmetric cell division by phosphorylating the cytoskeletal protein Lgl. *Nature* 422, 326–330 (2003).

58. Z. Yang, B. Xue, M. Umitsu, M. Ikura, S. K. Muthuswamy, B. G. Neel, The signaling adaptor

GAB1 regulates cell polarity by acting as a PAR protein scaffold. *Mol. Cell* 47, 469–483 (2012).

Wolman, M. & Granato, M. Behavioral genetics in larval zebrafish: learning from the young. *Dev. Neurobiol.* 72, 366-372 (2012).

59. F. Motegi, S. Zonies, Y. Hao, A. A. Cuenca, E. Griffin, G. Seydoux, Microtubules induce self-organization of polarized PAR domains in *Caenorhabditis elegans* zygotes. *Nat. Cell Biol.* 13, 1361–1367 (2011).

60. A. Sailer, A. Anneken, Y. Li, S. Lee, E. Munro, Dynamic opposition of clustered proteins stabilizes cortical polarity in the *C. elegans* zygote. *Dev. Cell* 35, 131–142 (2015).

61. S. Guo, K. J. Kemphues, *par-1*, a gene required for establishing polarity in *C. elegans* embryos, encodes a putative ser/thr kinase that is asymmetrically distributed. *Cell* 81, 611–620 (1995).

62. J. Dagher, F. Dugay, N. Rioux-Leclercq, G. Verhoest, E. Oger, K. Bensalah, F. Cabillic, F. Jouan, S. F. Kammerer-Jacquet, P. Fergelot, C. Vigneau, Y. Arlot-Bonnemains, M. A. Belaud-Rotureau, Cytoplasmic PAR-3 protein expression is associated with adverse prognostic factors in clear cell renal cell carcinoma and independently impacts survival. *Hum. Pathol.* 45, 1639–1646 (2014).

63. C. B. Kimmel, W. W. Ballard, S. R. Kimmel, B. Ullmann, T. F. Schilling, Stages of embryonic development of the zebrafish. *Dev. Dyn.* 203, 253–310 (1995).

64. D. Yu, Z. Dong, W. C. Gustafson, R. Ruiz-González, L. Signor, F. Marzocca, F. Borel, M. P. Klassen, K. Makhijani, A. Royant, Y. N. Jan, W. A. Weiss, S. Guo, X. Shu, Rational design of a

monomeric and photostable far-red fluorescent protein for fluorescence imaging in vivo. *Protein Sci.* 25, 308–315 (2016).

65. X. Wei, Y. Cheng, Y. Luo, X. Shi, S. Nelson, D. R. Hyde, The Zebrafish *Pard3* ortholog is required for separation of the eye fields and retinal lamination. *Dev. Biol.* 269, 286–301 (2004).

66. J. W. von Trotha, J. A. Campos-Ortega, A. M. Reugels, Apical localization of ASIP/PAR-3:EGFP in zebrafish neuroepithelial cells involves the oligomerization domain CR1, the PDZ domains, and the C-terminal portion of the protein. *Dev. Dyn.* 235, 967–977 (2006).

67. F. R. Zolessi, L. Poggi, C. J. Wilkinson, C. B. Chien, W. A. Harris, Polarization and orientation of retinal ganglion cells in vivo. *Neural Dev.* 1, 2 (2006).

68. X. Zhao, J. Kuja-Panula, M. Sundvik, Y. C. Chen, V. Aho, M. A. Peltola, T. Porkka-Heiskanen, P. Panula, H. Rauvala, Amigo adhesion protein regulates development of neural circuits in zebrafish brain. *J. Biol. Chem.* 289, 19958–19975 (2014).

69. J. Y. Tinevez, N. Perry, J. Schindelin, G. M. Hoopes, G. D. Reynolds, E. Laplantine, S. Y. Bednarek, S. L. Shorte, K. W. Eliceiri, TrackMate: An open and extensible platform for single-particle tracking. *Methods* 115, 80–90 (2017).

70. S. Seabold, J. Perktold, statsmodels: Econometric and statistical modeling with python, in *Proceedings of the 9th Python in Science Conference (SCIPY, 2010)*, pp. 92–96.

71. J. Gruenberg, The endocytic pathway: A mosaic of domains. *Nat. Rev. Mol. Cell Biol.* 2,

721–730 (2001).

72. E. M. Manders, J. Stap, G. J. Brakenhoff, R. van Driel, J. A. Aten, Dynamics of three-dimensional replication patterns during the S-phase, analysed by double labelling of DNA and confocal microscopy. *J. Cell Sci.* 103, 857–862 (1992).

73. S. V. Costes, D. Daelemans, E. H. Cho, Z. Dobbin, G. Pavlakis, S. Lockett, Automatic and quantitative measurement of protein-protein colocalization in live cells. *Biophys. J.* 86, 3993–4003 (2004).

CHAPTER 2: Phosphorylation by Aurora Kinase A Facilitates the Cortical-Cytoplasmic Dynamics of Par-3 in Asymmetric Division of Radial Glia Progenitors

2.1 ABSTRACT

During asymmetric cell division (ACD) of radial glia progenitors (RGPs), the cortical polarity regulator Par-3 is detected in the cytoplasm in a complex with dynein and Notch ligand DeltaD (Dld). The regulation of cytoplasmic Par-3 and its impact on RGP ACD remains unknown. Here, we visualize cytoplasmic Par-3 using in vivo time-lapse imaging and find that Serine-954 of zebrafish Par-3 is phosphorylated by Aurora Kinase A (AurkA). Expression of the non-phosphorylated mutant Par-3S954A exerts a dominant-negative effect on embryonic development, reduces cytoplasmic Par-3 presence, disrupts the anteroposterior asymmetry of cortical Par-3 and Dld, and in turn daughter cell fate. AurkA in mitotic RGPs shows dynamic peri-centrosomal localization that transiently contacts cortical Par-3. Over-expression of AurkA is sufficient to increase Par-3 cytoplasmic presence and disrupts Par-3 cortical asymmetry. Based on these findings, we propose that AurkA phosphorylation of Par-3 regulates its cortical-cytoplasmic dynamics that is critical for ACD and daughter cell fate.

2.2 INTRODUCTION

During early brain development, radial glia progenitors (RGPs), the principal vertebrate neural stem cells (NSCs), can undergo asymmetric cell division (ACD) to generate two distinct daughter cells: one maintains stemness (self-renewal) and the other becomes a differentiating neuron. The process of ACD is essential for generating diverse differentiated cell types while maintaining the stem cell population. Therefore, disruption of this process can lead to early developmental defects and cancer (1,2,3,4,5). Understanding and elucidating the mechanisms that regulate ACD is not only fundamental for understanding basic biology but also for elucidating disease mechanisms.

ACD requires the establishment of a polarity axis in relation to the cleavage plane in the

mother cell. The evolutionarily conserved Partitioning defective protein (Par) complexes, originally discovered in *C. elegans* (6,7,8,9), play a crucial role in regulating these processes. In the developing vertebrate forebrain, Par-3, also known as PARD3 in humans and Bazooka in *Drosophila*, is prominently localized at the apical cortex of neuroepithelial cells that later give rise to RGP (10,11,12,13,14). However, during active neurogenesis, most RGPs divide along the anterior-posterior (A-P) embryonic axis (not the perpendicularly positioned apical basal axis) to generate daughter cells with asymmetric activity of Notch signaling (13,14,15,16,17), a key regulator of cell fate decisions (18,19). Disruption of Par-3 results in a loss of Notch asymmetry (13,14) which may contribute to tumorigenesis and cancer metastasis (1,5,20,21,22).

Par-3 was thought to function exclusively at the cell cortex until recently. Studies in the developing zebrafish forebrain during active neurogenesis have revealed that apically localized Par-3 in dividing RGPs becomes further polarized along the A-P axis and is preferentially segregated to the posterior self-renewing daughter (14,23). Moreover, Par-3 is detected in the cytoplasm to form a complex with the dynein intermediate light chain 1 (Dlic1) on the Notch ligand DeltaD (Dld)-containing endosomes and is required for the asymmetric segregation of these endosome (23). Polarized dynamics of Notch signaling endosomes was first observed during ACD of *Drosophila* neural progenitors (24,25), suggesting that it is evolutionarily conserved.

Together, these findings raise the following questions: What is the relationship between cortical and cytoplasmic Par-3? How are the dynamics of Par-3 regulated, and how does such regulation contribute to the establishment of cell polarity of RGPs and ensuing daughter cell fate?

Phosphorylation, a crucial post-translational modification in biological systems, has profound impact on cellular processes, signaling cascades, and organismal development. Phosphorylation of Par-3 by the atypical protein kinase C (aPKC) (26,27,28,29,30), Par-1 (8,31),

and PLK-1 (32) has been studied in invertebrates or mammalian cells. Aurora A kinase (AurkA), highly expressed in the nervous system (33), emerges as a significant player in cellular processes associated with cell cycle regulation, particularly during development. Studies have linked AurkA with another Par complex component, Par-6, during ACD in *Drosophila* neuroblasts (34), and mammalian AurkA has been shown to phosphorylate human PARD3 at Ser-962 in axon formation of hippocampal neurons (35).

In this study, we carried out *in vivo* time-lapse imaging to observe the cortical-cytoplasmic dynamics of Par-3 using an established Par-3-GFP reporter (10,11,12,23). We provided evidence for a deployment of Par-3 from the cortex to the cytoplasm that is regulated by AurkA phosphorylation of the Ser-954 of Par-3. Furthermore, we detected a transient interaction between AurkA and cortical Par-3 on one side of the anaphase RGPs, correlating with the directionality of Par-3 cortical asymmetry along the A-P axis. Over-expression of AurkA increased Par-3 cytoplasmic presence and disrupted its cortical asymmetry. Overall, our findings reveal a role of AurkA in phosphorylating Par-3, regulating Par-3 cytoplasmic-cortical dynamics in mitotic RGPs, and neural progenitor fate.

2.3 RESULTS

2.3.1 In vivo time-lapse imaging detects the cytoplasmic Par-3 in mitotic RGP.

Using label retention expansion microscopy, we previously detected Par-3 in the cytoplasm in complexes with Dlic1 and Dld endosomes²³. To understand the nature of cytoplasmic Par-3 and its potential relationship to cortical Par-3, we carried out in vivo time-lapse imaging of mitotic RGPs in the developing zebrafish forebrain during active neurogenesis. The mRNAs encoding Par-3-GFP and Histone monomeric RFP (H2B-mRFP) (marks cell nuclei) were microinjected into one cell of 16-32 cell Tg[ef1a-MyrTdTtomato] (marks cell membranes) embryos to achieve sparse labeling. Subsequently, the Dld antibody conjugated to a fluorophore was microinjected into the brain ventricle at 22 hours post fertilization (hpf) to label Dld endosomes as previously described ^{23,36,37,38}. Live imaging was performed at ~24-30 hpf (Figure 1A). Punctate GFP signals were observed in the cytoplasm of mitotic RGPs starting at around metaphase (Figure 1B; Video S1). Compared to cortical Par-3, cytoplasmic Par-3 was detected at a much lower level. Consistent with previous expansion microscopy data ²³, colocalization of the GFP signal with Dld endosomes was observed (Figure 1B, insets). Intriguingly, cytoplasmic Par-3-GFP appeared as a gradient that emanated from the apical side and enriched on the side with more cortical Par-3 in the dividing RGPs (Figure 1C). Together, these observations provide evidence that rather than de novo protein synthesis, cytoplasmic Par-3 may be derived from the cortical pool.

To better visualize the dynamics of cytoplasmic Par-3, we reasoned that knocking down endogenous Par-3 and replacing it with exogenously provided Par-3-GFP should enhance the detection of cytoplasmic Par-3. We co-injected a validated Par-3 morpholino (MO) antisense oligonucleotide 11 with MO-resistant Par-3-GFP mRNAs as described above. Indeed, in vivo

time-lapse imaging of mitotic RGPs unveiled more intense Par-3-GFP signal in the cytoplasm. Intriguingly, cytoplasmic Par-3-GFP appeared as a large circular structure that was decorated with Dld endosomes. As mitotic RGPs progressed through the cell cycle, this structure moved toward the posterior (Figure 1D, 1E; Video S2). Together, in vivo time-lapse imaging of Par-3-GFP and Dld endosome dynamics provide evidence for a possible deployment of cortical Par-3 to the cytoplasm, where cytoplasmic Par-3 co-localizes with Dld endosomes in a large assembly that undergoes directional movement in mitotic RGPs.

2.3.2 Systemic expression of Par-3^{S954A} dominantly interferes with embryonic brain development.

To build on these qualitative observations and to understand the mechanisms that regulate the dynamics of Par-3, we turned to phosphorylation. Par-3 has many established and predicted phosphorylation sites, among which, two serines, Ser-227 and Ser-954 in zebrafish Par-3, conserved across vertebrates, are predicted phosphorylation sites of AurkA (Figure 2A).

Given that cytoplasmic Par-3 was prominent during mitosis, we sought to determine whether phosphorylation of these two serines by AurkA might play a role in this process. Precise genome editing of single amino acids has been reported in zebrafish 39, but the overall efficiency remains low and is highly dependent on having efficacious sgRNAs near the desired target sites. As we need to target two serines in different regions of Par-3, we decided to employ an alternative transgenic approach. Serine to Alanine and Serine to Aspartic acid mutations were introduced into Par-3-GFP. The mRNAs encoding these mutated forms of Par-3 were micro-injected into one-cell stage embryos (Figure 2B). Embryos were raised to 28 hours post fertilization (hpf) and their brain morphological phenotypes were scored using a phenotype rubric (Figure S1). We observed that while Par-3-GFP- or Par-3SD-GFP- injected embryos

appeared largely normal, Par-3SA-GFP- injected embryos showed defects in brain morphology similar to Par-3 morphants. Further analysis of individual serine mutations uncovered that Par-3S954A-GFP- but not Par-3S227A-GFP- injected embryos were defective (Figure 2C-D), suggesting that serine-954 is the key residue. Together, systemic expression of Par-3S954A-GFP dominantly interferes with endogenous Par-3 function leading to defects in embryonic brain development. These data provide evidence that phosphorylation of Par-3 at Ser-954 is critical for Par-3 function.

2.3.3 Sparsely expressed Par-3^{S954A} displays decreased cytoplasmic presence in mitotic RGP.

To determine whether phosphorylation of these two serines is critical for Par-3 dynamics in mitotic RGPs, we co-injected H2B-RFP with different forms of Par-3 mRNAs into one-cell of 16-32-cell stage Tg[ef1a-MyrTdTtomato] embryos (Figure 2B). By sparse labeling, we were able to follow individual RGPs using in vivo time-lapse imaging in embryos with normal brain morphology. The quantification method for cortical vs. cytoplasmic Par-3-GFP fluorescent intensity in RGPs was described in Figure S2. We found that in Par-3SA-GFP- and Par-3S954A-GFP- injected embryos compared to Par-3-GFP-injected ones, mitotic RGPs showed significantly decreased cytoplasmic Par-3 at metaphase and telophase, whereas Par-3SD-GFP- and Par-3S227A-GFP- injected embryos had no significant difference compared to controls (Figure 2E-F, Figure S1B-C; Videos S3-7). Together, these data provide evidence that phosphorylation of Par-3 at Ser-954 is critical for Par-3 cytoplasmic presence in mitotic RGPs.

2.3.4 Sparsely expressed Par-3^{S954A} is defective in anteroposterior cortical asymmetry, and dominantly interferes with Dld endosome formation and polarized dynamics in mitotic RGPs.

To further understand the effect of Par-3^{S954A} in mitotic RGPs, we simultaneously tracked the dynamics of the Par-3 reporter and internalized Dld using in vivo time-lapse imaging (Figure 3A). In control (Par-3-GFP -expressing) embryos, both Par-3 and Dld were preferentially segregated into the posterior daughter (Figure 3B) as previously reported²³. In Par-3^{SA}-GFP -expressing embryos, not only the cytoplasmic Par-3 SA-GFP signal was reduced, but also the cortical Par-3 SA-GFP asymmetry was disrupted (Figure 3C). These disruptions were not observed in Par-3^{SD}-GFP- and Par-3^{S227A}-GFP- expressing embryos (Figure 3D-E) but was similarly observed in Par-3^{S954A}-GFP- expressing embryos (Figure 3F). Further quantifications of both internalized Dld and Par-3 reporters at telophase showed a significantly reduced asymmetry of Par-3 reporter and Dld endosomes in Par-3^{SA}-GFP and Par-3^{S954A}-GFP- expressing embryos (Figure 3G-H). Additionally, a decrease of internalized Dld was observed in Par-3^{SA}-GFP- and Par-3^{S954A}-GFP- expressing embryos compared to tcontrols (Figure 3I). A similar decrease of internalized Dld expression was also observed in the Par-3 morphants compared to control MO (Figure S3), suggesting that these forms of non-phosphorylated Par-3 dominantly interfere with Dld endocytosis. Taken together, these findings suggest that phosphorylation at Ser-954 plays a role in promoting the cytoplasmic presence and cortical asymmetry of Par-3, and in turn Dld asymmetry during ACD in RGPs.

2.3.5 Systemic expression of Par-3^{S954A} dominantly interferes with progenitor-neuron fate specification in the developing forebrain.

Next, we investigated the impact of Par-3 phosphorylation at Ser-954 on cell fate in the

developing forebrain through an EDU (5-ethynyl-2'-deoxyuridine) labeling experiment. We expressed Par-3-GFP or Par-3S954A-GFP in WT embryos by microinjecting them at the one-cell stage. Embryos were then allowed to develop until 18 hpf, followed by injection of 50 μ M EDU into the yolk-sac, as previously described 40. Embryos were raised and fixed at 24 hpf and 36 hpf, and samples were prepared for cryo-sectioning and immunostaining for HuC (neuronal marker) and EDU (proliferation marker) using Click it-EDU chemistry labeling (Figure 4A).

Quantification of EDU positive cells at 24 hpf and 36 hpf showed no difference among WT, full-length Par-3-GFP-, and Par-3S954A-GFP- expressing embryos (Figure 4B-G, 4H, 4K), suggesting that the expression of Par-3S954A does not affect progenitor proliferation per se. However, we found a significant decrease in the ratio of EDU+HuC+/EDU+(Figure 4B-G, 4J, 4M) cells and a corresponding increase in the ratio of EDU+HuC-/EDU+ cells (Figure 4B-G, 4I, 4L), suggesting a reduced cell cycle exit of neural progenitors in Par-3S954A-GFP-expressing embryos compared to full-length Par-3-GFP-expressing and WT embryos. These results provide evidence that phosphorylation of Par-3 at Serine-954 is critical for promoting neurogenesis in the developing zebrafish forebrain.

2.3.6 Aurora Kinase A phosphorylates Par-3 at Ser-954 in vitro

To determine whether Ser-954 in zebrafish Par-3 is phosphorylated by AurkA, we performed an in vitro kinase assay using in vitro translated forms of Par-3 (Par-3-GFP, Par-3S227A-GFP, Par-3S954A-GFP, and Par-3SA-GFP) and recombinant AurkA (Figure 5A). We first verified that zebrafish Par-3 was phosphorylated by AurkA in vitro (Figure S4). We then used 35S labeling to quantify the amount of in vitro translated proteins for different forms of Par-3 and used this for normalization of the detected phosphorylation signals (Figure 5B). We uncovered significantly reduced phosphorylation for Par-3S954A-GFP and Par-3SA-GFP but not Par-3S227A-GFP

compared to Par-3-GFP (Figure 5D). Taken together, our biochemical analysis demonstrates that AurkA phosphorylates Par-3 at Ser-954 *in vitro*.

2.3.7 In vivo time-lapse imaging reveals a transient interaction between AurkA and cortical Par-3 that biases the directionality of Par-3 cortical asymmetry in mitotic RGPs.

To determine whether AurkA and Par-3 interact *in vivo*, we microinjected mRNAs encoding 100 pg Centrin-GFP (or Par-3-GFP) and 50 pg of mCherry-AurkA into one-cell of 16/32-cell stage Tg[b-actin2:H2B-HaloTag] (marking nuclei) embryos. We then incubated the embryos for 2 hours in the Halo ligand646 to label the nuclei prior to time-lapse imaging of mitotic RGPs (Figure 6A). Consistent with previous studies (33,41), we observed AurkA localization near the centrosomes in mitotic RGPs and the signal disappeared shortly after the completion of mitosis (Figure S5; Video S8).

Intriguingly, these peri-centrosomal AurkA underwent dynamic movements. We observed mCherry-AurkA and Par-3-GFP that were in proximity at metaphase and co-localized at anaphase in the posterior (Figure 6B; Video S9) or the anterior sides (Figure 6C; Video S10). In some RGPs, no such contact was observed (Figure 6D, Video S11). Next, we asked if there is a correlation between the side where AurkA interacted with cortical Par-3 and the directionality of Par-3 cortical asymmetry. We found that among 27 RGPs analyzed, 14 showed an AurkA-Par-3 interaction on the posterior side, 4 showed interaction on the anterior side, and 9 did not have detectable interaction. Among the RGPs with an AurkA-Par-3 interaction on the posterior side, 71% had Par-3-GFP asymmetrically segregated to the posterior daughter cell. Among the RGPs with an AurkA-Par-3 interaction on the anterior side, 50% had Par-3-GFP asymmetrically segregated to the anterior daughter cell. Additionally, in the cases where no Par-3-AurkA interaction was detected, 45% of RGPs had Par-3-GFP symmetrically distributed

between the two daughter cells (Figure 6E). Thus, there is a significant correlation between the side of AurkA-Par-3 dynamic interaction and the side of enriched cortical Par-3 in RGPs. These findings provide in vivo evidence that AurkA interacts with Par-3 to carry out the phosphorylation observed on ser-594 in vitro, and the site of such interaction significantly correlates with the directionality of Par-3 cortical asymmetry.

2.3.8 Inhibition of AurkA activity disrupts cell cycle progression in mitotic RGPs

Next, Next, we investigated the impact of inhibiting AurkA on mitotic RGPs, using a specific chemical inhibitor MK-5108. We microinjected the mRNAs encoding Par-3-GFP together with H2B-RFP into one-cell of 16-to 32-cell stage embryos to achieve sparse labeling. Subsequently, Dld antibody was microinjected into the brain ventricle at 20 hpf. Prior to imaging, embryos were incubated in 1 μ M MK-5108 for one hour (Figure S6A). In AurkA inhibitor-treated embryos, RGPs failed to complete mitosis and appeared to undergo cell cycle arrest (Figure S6B). Therefore, we were not able to assess the impact of AurkA loss-of-function on Par-3 dynamics.

2.3.9 Over-expression of Aurora Kinase A increases cytoplasmic Par-3 presence and disrupts Par-3 cortical asymmetry

We next asked how over-expression (OE) of AurkA might affect Par-3 dynamics and ACD of mitotic RGPs. One group of embryos were injected with mRNAs encoding Par-3-GFP into one-cell at the 16-to 32-cell stage to achieve sparse labeling (Figure 7A). Another group of embryos were injected with mRNAs encoding Par-3-GFP and AurkA into one-cell at the 16-to 32-cell stage (Figure 7B; Video S12). Significantly reduced Par-3-GFP in the apical cortex (Figure 7C) and a corresponding increase of non-apical Par-3-GFP (including both cytoplasmic and basally

enriched Par-3) (Figure 7D) were detected in the embryos injected with mRNAs encoding Par-3-GFP and AurkA, compared to those injected with mRNAs encoding Par-3-GFP only.

To determine whether decreased apical Par-3-GFP and increased non-apical Par-3-GFP is dependent on the phosphorylation of Par-3 at Ser-954 by AurkA, we injected mRNAs encoding Par-3S954A-GFP and AurkA into one-cell at the 16-to 32-cell stage embryos. We quantified the levels of AurkA overexpression in Par-3-GFP-injected vs. Par-3S954A-GFP-injected embryos and found them to be comparable (Figure S7). In the embryos co-injected with Par-3S954A-GFP and AurkA mRNAs (Figure 7E, Video S13), Par-3S954A-GFP fluorescence was significantly increased in the apical cortex (Figure 7F) and correspondingly reduced in the cytoplasm (Figure 7G), compared to those injected with mRNAs encoding Par-3-GFP and AurkA. Together, these results suggest that Ser-954 phosphorylation by AurkA is important for Par-3 cytoplasmic localization.

Finally, we asked how AurkA overexpression might affect Par-3 cortical asymmetry. In the embryos expressing Par-3-GFP, the reporter was enriched in the posterior daughter of telophase RGPs. In the embryos expressing Par-3-GFP and AurkA, a significant decrease of asymmetric posterior Par-3-GFP was observed. In the embryos expressing Par-3 S954A -GFP and AurkA, a significant decrease of asymmetric posterior Par-3 S954A-GFP was also observed (Figure 7H). These results suggest that the level of Par-3 phosphorylation by AurkA is critical for Par-3 asymmetry in mitotic RGPs: both too much and too little phosphorylation can lead to disrupted cortical asymmetry of Par-3.

2.4 DISCUSSION

The evolutionarily conserved polarity regulator Par-3 has been traditionally studied at the cell cortex for its role in establishing polarity during ACD. Recent discoveries, however, have revealed the presence of Par-3 in the cytoplasm of RGP, with clinical implications linking cytoplasmic Par-3 to adverse cancer prognosis 42. Despite this association, the origin and functionality of cytoplasmic Par-3 in polarity regulation remain poorly understood, prompting a deeper exploration of its dynamics and relationship with cortical Par-3. In this study, utilizing *in vivo* time-lapse imaging and molecular genetics, pharmacological, and biochemical approaches, we uncovered a dominant negative effect of the Ser-954A mutant form of Par-3. When expressed ubiquitously in wild-type embryos, this mutant disrupted embryonic brain development; when expressed sparsely, it preserved embryonic morphology but interfered with RGP ACD and daughter cell fate specification. We further showed that Ser-954 of Par-3 was phosphorylated by Aurora Kinase A, and this phosphorylation promoted the cytoplasmic presence (and a correspondingly decreased cortical presence) of Par-3. Both too much and too little phosphorylation led to disrupted Par-3 cortical asymmetry along the A-P axis. Based on these findings, we propose a mechanism for the regulation and function of cytoplasmic Par-3 during ACD in RGP. As RGP enter mitosis, AurkA becomes active. Through transient interaction with the apically localized Par-3 (mostly on the posterior side), AurkA phosphorylates Par-3 to promote its translocation into the cytoplasm. Subsequently, cytoplasmic Par-3 interacts with endocytosed Dld endosomes. Together, these components—cortical Par-3, cytoplasmic Par-3 (together with dynein), and Dld endosomes—are asymmetrically segregated to the posterior daughter cell, where they play a crucial role to promote the fate of progenitor state. When such asymmetry was disrupted in the RGP expressing the dominant negative Par-3S954A -GFP, a decrease of neuronal production and a corresponding increase of progenitors were observed (Figure 7I).

Our findings reveal a new role of AurkA in phosphorylating Par-3 at Ser-954 and suggest that this phosphorylation deploys the cortical Par-3 into the cytoplasm. It is conceivable that such phosphorylation may disrupt Par-3 interactions with other cortical proteins such as Par-6 or aPKC, thereby releasing it from the cortex. Once in the cytoplasm, Ser-954 phosphorylated Par-3 can interact with other proteins such as dynein motor and endosome-associated proteins.

Intriguingly, AurkA phosphorylation of Par-3 at Ser-954 also impacts the cortical asymmetry of Par-3. How this is accomplished is not clear. We can postulate two possible mechanisms. One involves the initial deployment of phosphorylated Par-3 to the cytoplasm and subsequent return of de-phosphorylated Par-3 back to the cortex preferentially on the posterior side of the cell. Alternatively, phosphorylated Par-3 may travel within the cortical domain in addition to being deployed into the cytoplasm, leading to posterior enrichment. Future experiments are required to test these hypotheses.

2.5 LIMITATIONS OF THE STUDY

This study involved ectopic expression of Par-3 and its mutant forms. Therefore, it becomes imperative to conduct further research aimed at validating the findings with tagged endogenous wildtype and mutant forms of proteins *in vivo*.

While our study provides valuable insights into the regulation of Par-3 dynamics by AurkA *in vivo* in mitotic RGPs of the developing zebrafish forebrain, questions remain regarding the precise mechanisms governing the deployment of cytoplasmic Par-3 during mitosis. Future investigations will unravel these intricate mechanisms and deepen our understanding of Par-3 regulation during ACD in RGPs. For example, exploring how this phosphorylation impacts the interaction of Par-3 with other Par complex members (aPKC, Par-6) and dynein motors could

provide further understanding into the regulation of Par-3 during ACD. It will also be of interest to explore whether phosphatases are involved in dephosphorylating cytoplasmic Par-3 to enable its return to the cortex linking to the observed cortical asymmetry.

2.6 MATERIALS AND METHODS

2.6.1 Experimental design

Mitotic RGP in the developing zebrafish forebrain during active neurogenesis were analyzed using a combination of in vivo time-lapse imaging, molecular genetics, pharmacology, and biochemistry, which has uncovered the role of Par-3 phosphorylation during ACD in RGP.

2.6.2 Zebrafish strains and maintenance

Wild-type (WT) embryos were obtained from natural spawning of AB adults, staged, and maintained according to established protocols 43. Embryos were raised at 28.5°C in 0.3× Danieau's embryo medium (30× Danieau's embryo medium contains 1740 mM NaCl, 21 mM KCl, 12 mM MgSO₄·7H₂O, 18 mM Ca(NO₃)₂, and 150 mM Hepes buffer). Embryonic ages were described as hpf. The following zebrafish mutants and transgenic lines were used: Tg[ef1a:Myr-Tdtomato] and Tg[b-actin2:H2B-HaloTag] 44, Halo Tag ligand, Janelia Flour 646 (1:1,000) for 2 hours prior to imaging. All animal experiments were approved by the Institutional Animal Care and Use Committee at the University of California, San Francisco, USA. with National Institutes of Health and University of California, San Francisco guidelines.

2.6.3 Morpholinos

Knockdown experiments were carried out using previously characterized translational blocking antisense MOs: pard3ab/par-3 MO (5' -TCA AAG GCT CCC GTG CTC TGG TGT C-3') 11,12,14,25,45. All MOs were stored at 300 mM in distilled water. Standard control MO (5' -CCT CTT ACC TCA GTT ACA ATT TAT A-3') was used as injection controls (Gene Tools). For microinjection, ~4 nl of the diluted MO at 100 mM in the injection mixture containing 0.05% phenyl red (corresponding to 4 ng of MOs) was injected into the yolk of one- to four-cell stage embryos.

2.6.4 DNA plasmids and complementary DNA preparation

Plasmid DNAs (pCS2-H2B-mRFP) were prepared as previously described 14,46. pCS2-par-3-GFP plasmid was a gift from J. von Trotha 10. pCS2-GFP-centrin plasmid was a gift from W. A. Harris 47. pCS2-mCherry-AurkA was a gift from Hee-Yeon Jeon 31. pCS2-Par-3-SA-GFP (Ser227 and Ser954 converted to Ala227 and Ala954) and pCS2-Par-3-SD-GFP (Ser227 and Ser954 converted to Asp227 and Asp954) were designed by Su Guo and sent to VectorBuilder for implementing phosphorylation mutants. Single phosphor-mutants: pCS2-Par-3-S227A-GFP and pCS2-Par-3-S954A-GFP were cloned using Gibson Assembly (NEBuilder). For all par-3-GFP, GFP is at the 3' end of Par-3 protein. For GFP-centrin, GFP is at the 5' end of centrin. For mCherry-AurkA, mCherry is at the 5' end of AurkA.

2.4.3 Whole mount in situ hybridization

2.6.5 mRNA synthesis and microinjection

Plasmids (pCS2-H2B-mRFP, pCS2-Par-3-GFP, pCS2-Par-3-SA-GFP, pCS2-Par-3-SD-GFP, pCS2-Par-3-S227A-GFP, pCS2-Par-3-S954A-GFP, pCS2-mCherry-AurkA, and pCS2-GFP-centrin) were linearized by the restriction enzyme Not I digestion. NotI-linearized plasmids were purified (QIAquick Gel Extraction Kit), and the 5' -capped mRNAs were synthesized using the SP6 mMessenger mMachine Kit (Ambion). For GFP-centrin, H2B-mRFP, and all Par-3-GFP mRNAs, mRNA injection, 4- μ l mRNAs at 0.2 to 0.5 μ g/ μ l were mixed with an equal volume of injection buffer containing 0.05% phenyl red and injected into the yolk of a one- to four-cell stage embryos. For all Par3-GFP mRNAs injection, the mRNAs were injected into single cells at the 32- to 64-cell stages to obtain mosaic expression. All injections were done with an injector (WPI PV830 Pneumatic Pico Pump) and a micro-manipulator (Narishige, Tokyo, Japan).

2.6.6 Anti-Dld antibody uptake assay

Anti-mouse immunoglobulin G (IgG)-Atto647N (Sigma-Aldrich, 50185) was used for labeling the mouse monoclonal anti-Dld antibody (Abcam, ab73331). For antibody conjugation, 1 μ l of anti-Dld antibody (0.5 mg/ml) was mixed with 2.5 μ l of anti-mouse IgG-Atto647N antibody (1 mg/ml) and incubated at room temperature for 30 min or on ice for 2 to 3 hours. After incubation, 2.5 μ l of blocking buffer [mouse IgG (10 mg/ml) with 5 mM azide] and 0.5 μ l of 0.5% phenol red (Sigma-Aldrich, P0290) were added for blocking the unconjugated anti-mouse IgG-Atto647N and vortexed thoroughly. Mixtures without anti-Dld antibody were used as control. Before microinjection, 24- to 26-hpf embryos were anesthetized in the Danieau medium supplemented with 0.003% tricaine followed by embedding in 1.2% low-melting point agarose. Ten nanoliters of labeled Dld antibody was injected into the hindbrain ventricle. The phenol red indicator shows

the diffusion of antibody mix-ture into the forebrain ventricle. The injected embryos were then released from agarose and cultured in the Danieau medium for 2 hours before imaging.

2.6.7 Pharmacology

Zebrafish embryos were treated with an Aurora Kinase A inhibitor [Medchemexpress, (MCE), MK-5108, HY-13252, CAS No.:1010085-13-8] from 22 to 24 hpf for about one hour before imaging. DId antibody uptake assay was performed prior to Vehicle (DMSO)–treated control and 1 μ M AurkA-treated embryos were then embedded in 1.5% low–melting point agarose in the Danieau medium, 0.003% tricaine for in vivo time-lapse imaging.

2.6.8 Antibodies, Western blotting, and immunocytochemistry

Primary antibodies used in this study were as follows: mouse anti-DId [Abcam, ab73331; Research Resource Identifier (RRID): AB_1268496; chicken anti-GFP (Abcam, ab13970; RRID: AB_300798; lot GR3190550-20; 1:500 dilution for immunostaining), rabbit anti–Par-3 (Millipore 07-330; RRID: AB_2101325; lot 3322358; 1:500 for immunostaining), anti-HuC (Invitrogen A-21271; RRID: AB_221448; 1:1000 for immunostaining). EdU labeling; Click-iT EdU Alexa Flour 555; C10338; lot 2491411. The kit contains all components needed to label DNA-synthesizing cells and to detect EdU incorporated into DNA. Stained according to the manufacturer's protocol (Invitrogen). For 5-ethynyl-2' -deoxyuridine (EdU) labeling, Embryos are embedded in 1.2% low melt agarose, EdU and 0.5 ul of 0.5% phenol red (Sigma-Aldrich, P0290) were added to the injection mixture and was administered into the yolk sac with 4.2 nl of 50 μ Mol at 18 hpf into the yolk sac. For the preparation of cryosections, 28-hpf and 36-hpf embryos were fixed overnight at 4°C in phosphate-buffered saline (PBS) buffer with 4% paraformaldehyde. Fixed embryos

were washed abundantly with PBS and then cryoprotected in 30% sucrose overnight at 4°C. Embryos were then embedded with optimum cutting temperature (OCT) (Tissue-Tek) and transferred to plastic molds. After orienting the embryos to proper positions in the mold, the block was frozen on dry ice and then stored at -80°C up to several months. Frozen blocks were then cut into 18-um sections on a cryostat (Leica) and mounted on Superfrost Plus slides (Thermo Fisher Scientific). The slides were dried at room temperature for 2 to 3 hours and then stored at -80°C until use.

2.6.9 In vitro–translated proteins and In vitro Immunoprecipitation

pCS2+-Par-3-GFP plasmid and phosphor-mutants (pCS2+-Par-3-S227A-GFP, pCS2+-Par-3-S954A-GFP, and pCS2+-Par-3-SA-GFP) plasmids were generated in TNT SP6 High-Yield Protein Expression System (Promega) according to the manufacturer's instructions. In brief, 1ug of DNA was mixed with a master mix of TNT Sp6, and Methionine or radiolabeled Methionine (S35). Incubated at 25c for 2 hours and then mixed with the ChromoTek GFP-Trap®_Agarose beads (Proteintech). The beads were then washed twice with ice cold wash buffer, In vitro kinase assay was performed, and after samples were resuspended in 4x laemmli sample buffer and boiled for 10 minutes at 95°C before loading onto the SDS-PAGE gels.

2.6.10 In vitro–translated proteins and In vitro Immunoprecipitation

pCS2+-Par-3-GFP plasmid and phosphor-mutants (pCS2+-Par-3-S227A-GFP, pCS2+-Par-3-S954A-GFP, and pCS2+-Par-3-SA-GFP) plasmids were generated in TNT SP6 High-Yield Protein Expression System (Promega) according to the manufacturer's instructions. In brief, 1ug of DNA was mixed with a master mix of TNT Sp6, and Methionine or 35S-labeled Methionine.

Incubated at 25°C for 2 hours and then mixed with the ChromoTek GFP-Trap®_Agarose beads (Proteintech). The beads were then washed twice with ice cold wash buffer, In vitro kinase assay was performed, and after samples were resuspended in 4x laemmli sample buffer and boiled for 10 minutes at 95°C before loading onto the SDS-PAGE gels.

2.6.11 In Vitro Kinase Assay

For multisite phosphorylation analysis of WT and mutant Par-3, phosphorylation reactions were supplemented with [γ -³²P]-ATP (Hartmann Analytic). Reactions were stopped at 5, 15, and 60 min by pipetting an aliquot of SDS-PAGE into sample buffer (1 mol HEPES, pH 7.5, 2 mol NaCl, 1 mol MgCl₂, 100 μ Mol DTT, and H₂O). Reactions were separated on 7.5% SDS (Bio-Rad). ³²P phosphorylation signals were detected using an Amersham Typhoon 5 Biomolecular Imager (GE Healthcare Life Sciences) and quantified using ImageQuant TL (Amersham Biosciences). 250 nmol of Human Aurora Kinase A-His Tag Recombinant Protein (Invitrogen, PR5935A).

2.6.12 Time-lapse in vivo imaging

Time-lapse in vivo imaging Time-lapse in vivo imaging was done using a confocal microscope (Nikon CSU-W1 Spinning Disk/High Speed Widefield confocal microscopy and Weill CSU-W1 SoRA Spinning Disk Confocal) with a 40 \times water immersion objective. Embryos were mounted with 1.5% low-melting point agarose (0.3 \times Danieau medium and 0.003% tricaine) in glass-bottom culture dishes (MatTek; 35 mm) with the dorsal forebrain facing the coverslip. For in vivo time-lapse imaging of internalized DId or Par3-GFP in dividing RGPs of Tg [ef1a:Myr-Tdtomato], z-stacks with 20 to 30 z-planes were acquired consecutively at a 1- μ m z-step for each embryonic forebrain region. The exposure time for each fluorescent channel was set at 200 ms

by choosing the sequential channel scanning mode for each z-plane. The interval between each z-stack was 20 secs. Usually, 90 volumes of z-stacks were captured for each time-lapse imaging, and the duration spanned about 35 mins.

2.6.13 Image analyses

Image analyses All the confocal imaging stacks were captured and processed using Micro-Manager 2.0 gamma (uManager, University of California) and ImageJ. Dividing RGPs, maximum intensity projection of 3 z-planes (1-um z-step) was applied to the three-dimensional image stacks to cover the entire RGP. Each RGP at every time frame was manually segmented according to the cell membrane labeling. As previously described in Zhao et al., 2021 Science Advances. Cell-profiler was used for the pulse-chase cryosection, 21 microns were taken and the brightest (1-um z-step) was taken and processed and analyzed through cell profiler. We established a pipeline for image intensity through cell-profiler.

2.6.14 Quantification and statistical analysis

The number of times each experiment was repeated was provided in the figures or figure legends. For live imaging, one or multiple RGPs were analyzed from each embryo, depending on the number of mitotic RGPs that were present in each image stack. No statistical methods were used to predetermine sample size. Sample size was determined to be adequate based on the magnitude and consistency of measurable differences between groups. No randomization of samples was performed. Embryos used in the analyses were age-matched between control and experimental conditions, and sex cannot be discerned at these embryonic stages. Investigators were not blinded to chemically or genetically perturbed conditions during experiments. Data are

quantitatively analyzed. Statistical analyses were carried out using Prism 10 version 10.1.1: The mean value with SEM was labeled in the graphs. The two-tailed unpaired t test and two-tailed mann whitney were used to assess significance. One-way ANOVA with a post-hoc comparison used to assess significance as well. The chi-square analyses were also applied. As previously described in Zhao et al., 2021 Science Advances.

2.6.15 Measurement of asymmetry index

The total fluorescence intensity of internalized Dld (or Par-3-GFP) in paired daughter cells immediately after abscission (i.e., at telophase of mother RGP division) was measured by ImageJ. To quantitatively describe the distribution, normalized ratio of fluorescence between the two newly formed daughter cells was calculated as follows:

$$X = \frac{\sum_{i=1}^n (\text{Dld})_P - \sum_{i=1}^n (\text{Dld})_A}{\sum_{i=1}^n (\text{Dld})_P + \sum_{i=1}^n (\text{Dld})_A}$$

Figure 2.1 Measurement of asymmetry index.

$\Sigma(\text{Dld})_P$ means total intensity in the posterior daughter cell, and $\Sigma(\text{Dld})_A$ means total intensity in the anterior daughter cell. “0” indicates perfect symmetry, and “1” or “-1” indicates absolute asymmetry (posterior or anterior, respectively). For filtering out potential noise, we defined asymmetry when $\Sigma(\text{Dld})_P$ is 50% more or less than $\Sigma(\text{Dld})_A$, as has been previously used for quantifying Par-3 asymmetry 13 and internalized Dld-containing Sara endosome asymmetry 17. It means that when $X \geq 0.2$, Dld endosomes (and Par-3-GFP) are considered asymmetric with more in the posterior daughter, and when $X \leq -0.2$, they are considered asymmetric with more in

the anterior. The asymmetry index for Par3-GFP included both membrane and cytoplasmic fluorescence. As previously described in Zhao et al., 2021 Science Advances.

2.7 ACKNOWLEDGEMENTS

We thank M. Munchua and Evan Lee for excellent animal care, Guo laboratory members for helpful discussions, D. Larsen, K. Harrington, S. Kim, and UCSF Nikon imaging center for assistance with imaging and data analysis.

2.8 FIGURES

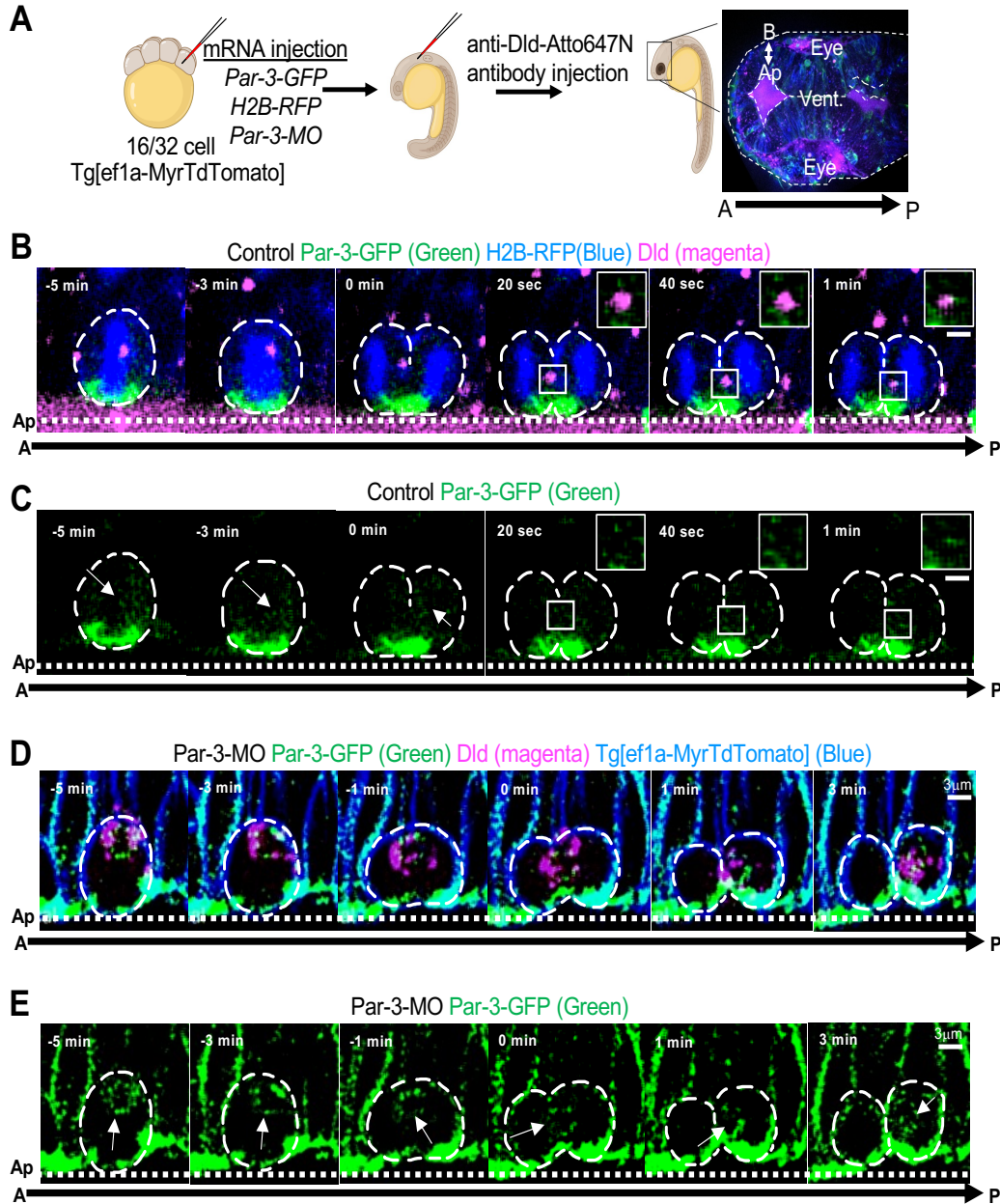


Figure 2.2 In vivo time lapse imaging reveals cytoplasmic Par-3 in mitotic RGP.

(A) Experimental Schematic of sparse labeling of mRNA injection (200 pg). Embryos are injected with mRNA at 16/32 cell stage to achieve sparse labeling. Embryos are then incubated until 20 hpf, which Dld antibody uptake assay is performed in the hindbrain. 24 hpf embryos are then mounted on a petri dish with a glass cover for live confocal imaging. Confocal image of a 40x zebrafish forebrain 28 hpf under 40x water immersion objective (NA=1.40)(dorsal view). Membrane is marked with Tg[ef1a-MyrTdTomo] embryos (pseudo-colored in blue), DNA is marked by H2B-RFP (pseudo-colored in blue) (Figure caption continued on the next page),

(Figure caption continued from the previous page) and Par-3-GFP (Green). Time-lapse sequence of all images shown are the maximum MIP of three confocal z-stacks (1- μ m z-step). Time = -3 min denotes metaphase. The time interval between each volume of z-stacks is 20s, and the total acquisition time is 30 mins. (B) Time-lapse sequence of images showing the dynamics of internalized Dld and Par-3-GFP in mitotic RGPs. Inserts visualize cytoplasmic Par-3 and Dld, demonstrating interactions during live imaging in RGPs. (C) Time-lapse sequence of images showing the dynamics of Par-3-GFP (only) in mitotic RGPs. (D) One-to four-cell stage Tg[ef1a-MyrTdTomato] embryos (pseudo-colored in blue) embryos were injected with 4 ng of morphant and 400 pg of Par-3-GFP to rescue phenotype. Embryos are then incubated until 20 hpf, which Dld antibody uptake assay is performed in the hindbrain. 24-30 hpf embryos are then mounted on a petri dish with a glass cover for live confocal imaging. Time-lapse sequence of images showing the dynamics of internalized Dld and Par-3-GFP in mitotic RGPs. Time lapse imaging reveals cytoplasmic Par-3 and Dld, demonstrating interactions during live imaging in RGPs. Time = 3 min denotes telophase. The time interval between each volume of z-stacks is 30s, and the total acquisition time is 30 mins. All images shown are the maximum MIP of three confocal z-stacks (1- μ m z-step). (E) Time-lapse sequence of images showing the dynamics of Par-3-GFP (GFP only) in mitotic RGPs. Ap (Apical), A (anterior), B (Basal), P (posterior), and Vent. (ventricle).

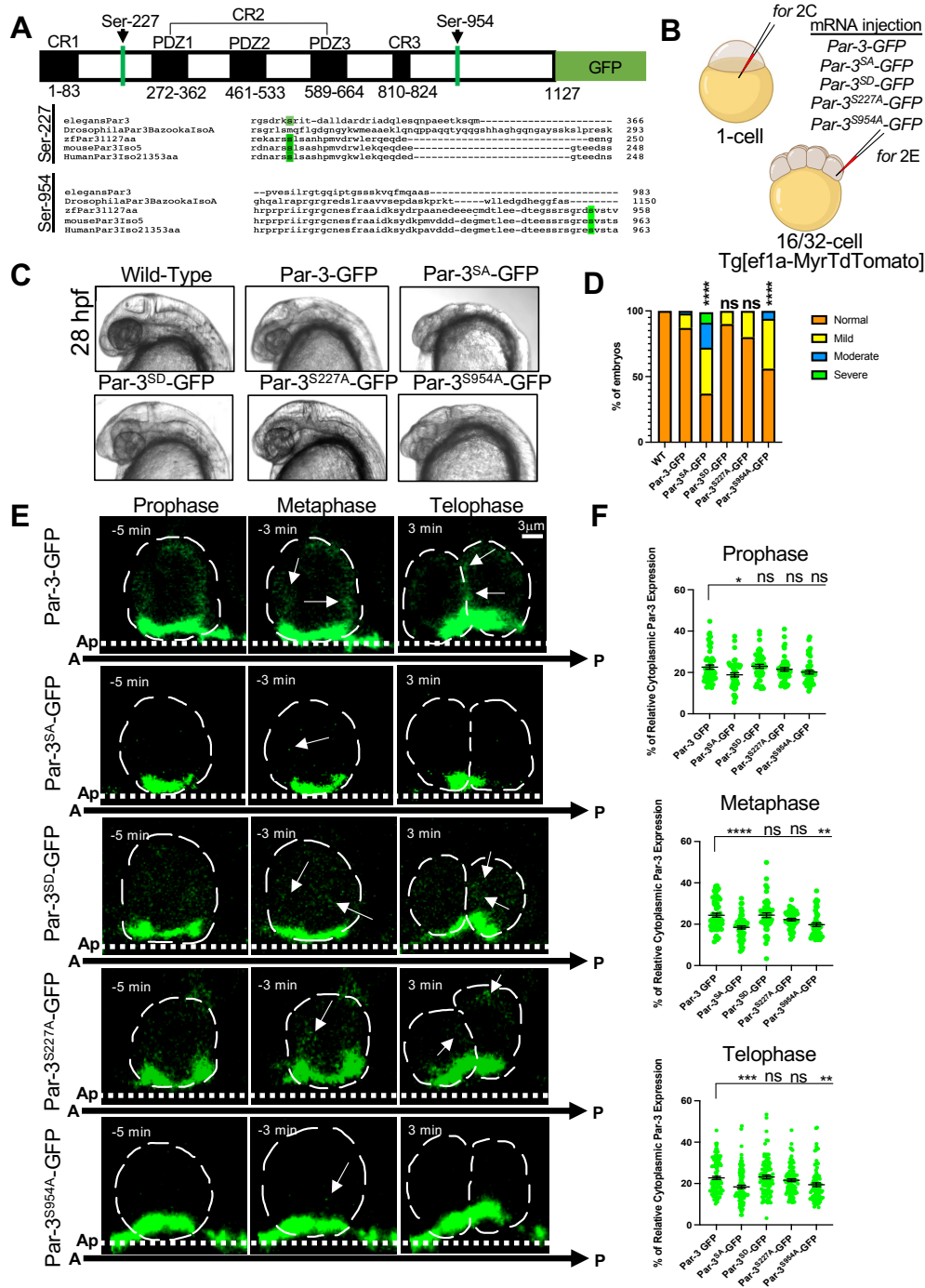


Figure 2.3 Par-3^{Ser954} Phospho-Incapable mutant reveals a dominate negative affect during brain development and cytoplasmic Par-3 localization in RGPs.

Par-3 consists of three conserved regions (CRs), the oligomerization domain (CR1) the three PDZ domains (CR2), and the aPKC binding domain (CR3). The predicted Aurora Kinase A phosphorylation sites are located at Ser227 & Ser954 (green bars indicate phosphorylation sites). Phosphorylation sites are conserved across (Figure caption continued on the next page),

(Figure caption continued from the previous page) other organisms. (B) Experimental schematic of one-cell and 16/32 cell injections into zebrafish embryos using mRNAs of Par-3-GFP and Par-3-(SA,S954A,SD,S227A)-GFP with a dosage of 200 pg. (C) Embryos were raised to 28 hours post fertilization (hpf) and images were taken at 200x on the Zeiss compound microscope 02 using micromanager 1.4 to document phenotypic effects on the forebrain. Uninjected/Wild-Type embryos were used as a control. From 9 repeated experiments. (D) Phenotype quantification. (Chi-square=199.7 df=15) $P < 0.0001^{****}$. Phenotypes are described in supplemental figure 1. Time-lapse sequence of images showing Par-3 and Par-3 phospho mutants (GFP only) in mitotic RGP at Prophase, Metaphase, and Telophase. All images shown are the maximum MIP of three confocal z-stacks (1- μ m z-step). The time interval between each volume of z-stacks is 20s, and the total acquisition time is 30 min. Time = 3 min denotes telophase. (F) Quantification. Relative cytoplasmic Par-3 expression was measured at prophase, metaphase, and telophase using Fiji. One way ANOVA Test with a Post-Hoc comparing to control (Par-3-GFP), Prophase: Par-3-GFP (N=54), Par-3-SA-GFP (N=46), Par-3-SD-GFP (N=49), Par-3-S227A-GFP (N=49), and Par-3-S954A-GFP (N=44). $P = 0.0163$, *, $R^2: 0.04954$. Par-3-SA-GFP * $P < 0.0226$, Par-3-SD-GFP NS $P > 0.9960$, Par-3-S227A-GFP NS $P > 0.8320$, and Par-3-S954A-GFP NS $P > 0.2193$. Metaphase: Par-3-GFP (N=56), Par-3-SA-GFP (N=56), Par-3-SD-GFP (N=50), Par-3-S227A-GFP (N=50), and Par-3-S954A-GFP (N=44). $P < 0.0001^{****}$, $R^2: 0.1271$. Par-3-SA-GFP **** $P < 0.0001$, Par-3-SD-GFP NS $P > 0.9999$, Par-3-S227A-GFP $P > 0.2780$, and Par-3-S954A-GFP ** $P < 0.0018$. Telophase: Par-3-GFP (N=56), Par-3-SA-GFP (N=55), Par-3-SD-GFP (N=50), Par-3-S227A-GFP (N=50), and Par-3-S954A-GFP (N=44). $P < 0.0001^{****}$, $R^2: 0.05002$. Par-3-SA-GFP *** $P < 0.0003$, Par-3-SD-GFP NS $P > 0.9985$, Par-3-S227A-GFP NS $P > 0.6938$, and Par-3-S954A-GFP ** $P < 0.0064$. Arrows indicate Cytoplasmic Par-3. Ap (Apical), A (anterior), and P (posterior). The RGs from Par-3-GFP, Par-3-SA, Par-3-S954, —r--3-SD, and Par3-S227A are from 16, 16, 13, 15, and 13 embryos, respectively, in 9, 9, 7, 7, and 6 repeated experiments, respectively.

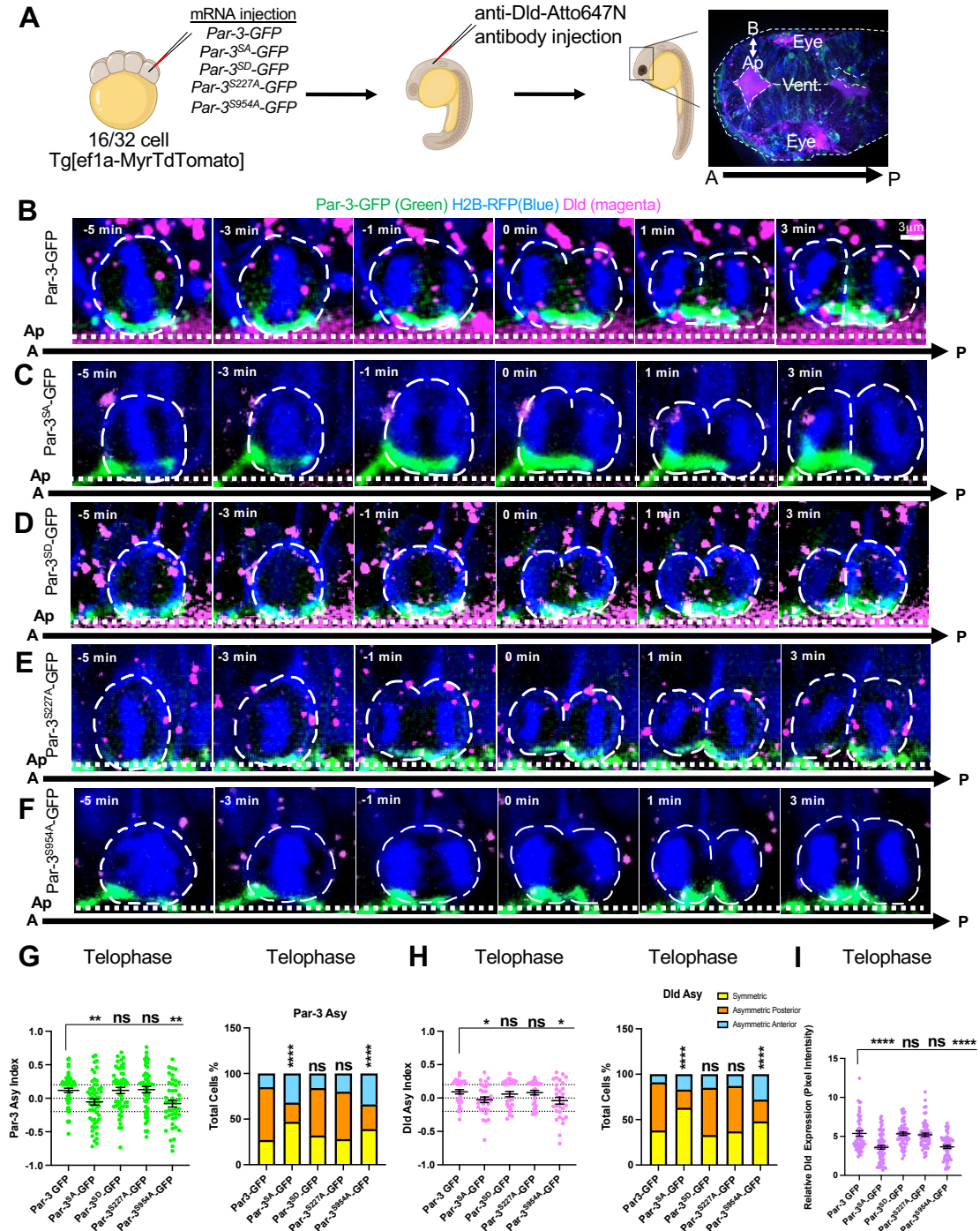


Figure 2.4 Par-3 Phospho-Incapable mutants demonstrate a disruption of Par-3 and Dld asymmetry during RGP ACD.

(A) Experimental Schematic: mRNA injections (200 pg) into 16/32 cell embryos to achieve sparse labeling. Embryos are then incubated until 20 hpf, which Dld antibody uptake assay is performed in the hindbrain. Embryos are mounted and confocal imaging is conducted at 40x of the zebrafish forebrain 28 hpf water immersion (Figure caption continued on the next page),

(Figure caption continued from the previous page) objective (NA=1.40) (dorsal-view). Membrane is marked with Tg[ef1a-MyrTdTomato] embryos (pseudo-colored in blue), DNA is marked by H2B-RFP (pseudo-colored in blue) and Par-3-(SA,S954A,SD,S227A)-GFP (Green). Time-lapse sequence of images showing the dynamics of internalized Dld and Par-3-GFP (SA, S954A, SD and S227A) in mitotic RGPs. Time = 3 min denotes telophase when asymmetry indices are calculated. The time interval between each volume of z-stacks is 20s, and the total acquisition time is 30 mins. All images shown are the maximum MIP of three confocal z-stacks (1- μ m z-step). (B) Par-3-GFP: both internalized Dld and Par-3 are asymmetrically segregated to the posterior daughter shortly after division. (C) Par-3-SA-GFP: disrupts internalized Dld and Par-3 asymmetry shortly after division compared to Par-3-GFP. (D) Par-3-SD-GFP: both internalized Dld and Par-3 are asymmetrically segregated to the posterior daughter shortly after division, similar to Par-3-GFP. (E) Par-3-S227A-GFP: both internalized Dld and Par-3 are asymmetrically segregated to the posterior daughter shortly after division, similar to Par-3-GFP. (F) Par-3-S954A-GFP: disrupts internalized Dld and Par-3 asymmetry shortly after division compared to Par-3-GFP. (G-I) Quantification. Scatter plot showing asymmetry indices in telophase RGPs. The asymmetry indices of Par-3-GFP (Left) and internalized Dld (right) The dotted lines indicate the threshold of |0.2| for calling asymmetry. The Par-3 Asy index unpaired two tailed t-test shows significance between Par-3-GFP vs. Par-3-SA-GFP, $^{**}P < 0.0024$ ($t=3.109$, $df=110$) and Par-3-GFP vs. Par-3-S954A-GFP, $^{**}P < 0.0013$ ($t= t=3.302$, $df=99$). However, there is no significant difference in the unpaired two tailed t test between: Par-3-GFP vs Par-3-SD-GFP, $ns= 0.9793$ ($t=0.02606$, $df=104$) and Par-3-GFP vs Par-3-S227A-GFP, $ns=0.8519$ ($t=0.1871$, $df=104$). Mean with SEM is shown for each group. Bar graph showing the percentage of RGPs with different patterns of Par-3. Disruption of Par-3 activity results in a significant decrease of asymmetric posterior Par-3. $^{****}P < 0.0001$, Par-3: (chi-square = 47.51, $df = 8$) (H) Scatter plot showing asymmetry indices in telophase RGPs. The asymmetry indices of internalized Dld (right) The dotted lines indicate the threshold of |0.2| for calling asymmetry. The Dld Asy index unpaired two tailed t test shows significance between Par-3-GFP vs. Par-3-SA-GFP, $^{*}P < 0.0259$ ($t=2.284$, $df=60$) and Par-3-GFP vs. Par-3-S954A-GFP, $^{*}P < 0.0448$ ($t=2.049$, $df=60$). However, there is no significant difference in the unpaired two tailed t test between: Par-3-GFP vs Par-3-SD-GFP, $ns=0.4980$ ($t=0.6820$, $df=57$) and Par-3-GFP vs Par-3-S227A-GFP, $ns=0.7862$ ($t=0.2725$, $df=60$). Mean with SEM is shown for each group. Bar graph showing the percentage of RGPs with different patterns of internalized Dld distribution. Disruption of Dld activity results in a significant decrease of asymmetric posterior Dld distribution; Dld: (chi-square = 50.63, $df = 8$). (I) RGPs Telophase: relative Dld expression graph reveals a decrease of Dld expression in Par-3-SA-GFP and Par-3-S954A-GFP compared to control Par-3-GFP. One way ANOVA test with a post-Huc comparing to control (Par-3-GFP). $^{****}p < 0.0001$, $R^2=0.1564$: Par-3-GFP ($n=32$), Par-3-SA-GFP ($n=30$), Par-3-SD-GFP ($n=27$), and Par-3-S227A-GFP ($n=30$), and Par-3-S954A-GFP ($n=29$). $^{****}P < 0.0001$, Par-3-SA-GFP $^{****}P < 0.0001$, Par-3-SD-GFP $ns=0.8943$, Par-3-S227A-GFP $ns=0.8527$, and $^{****}P < 0.0001$ Par-3-S954A-GFP $P < 0.0001$. Ap (Apical), A (anterior), and P (posterior). The RGPs from Par-3-GFP, Par-3-SA-GFP, Par-3-S954A-GFP, Par-3-SD-GFP, and Par-3-S227A-GFP are from 10, 10, 9, 8, and 8 embryos, respectively. Additionally, from 6, 5, 4, 4, and 3 repeated experiments, respectively.

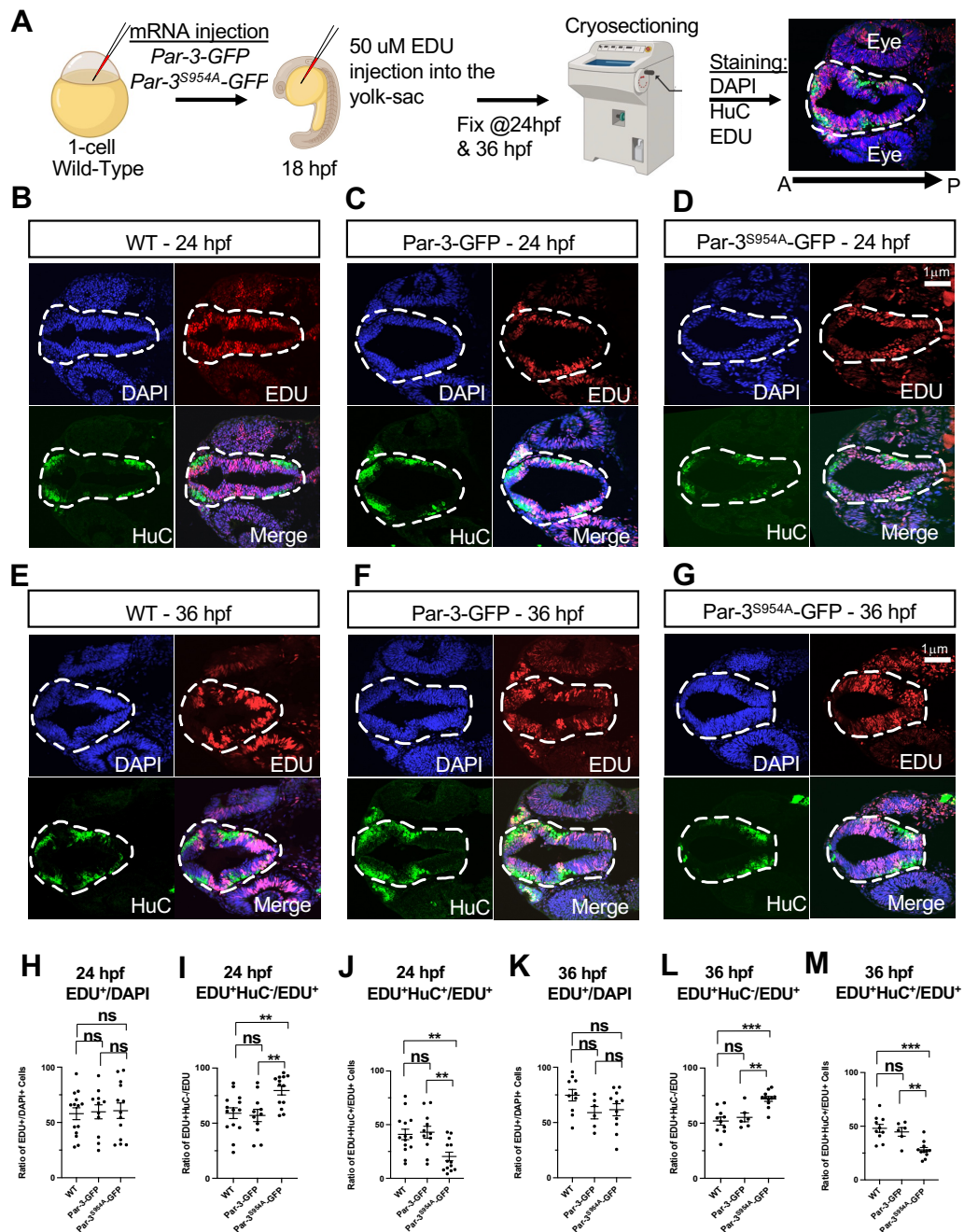


Figure 2.5 Par-3^{S954A} dominantly interferes with progenitor cell fate during active neurogenesis.

(A) Experimental schematic: one-cell injections (200 μ g) of Par-3-GFP and Par-3^{S954A}-GFP into WT embryos. Embryos are raised to 18 hpf and then injected with 50 μ Mol of EDU into yolk-sac and incubated until 24 hpf. Next, embryos are then fixed at 24 hpf and 36 hpf and prepared for cryosection and imaged on the confocal (B-D) (Figure caption continued on the next page),

(Figure caption continued from the previous page) 24 hpf Pulse condition; WT, Par-3-GFP, and Par-3S954A-GFP 24 hpf cryo-slices, images are single z-stack projection (1 μ m), and stained with Dapi, anti-HuC, and anti-EDU. The dash line is highlighting the Telencephalon, forebrain region of interest. (E-G) 36 hpf Chase condition; WT, Par-3-GFP, and Par-3S954A-GFP 36 hpf cryo-slices, images are 1 micron, and stained with Dapi, anti-HuC, and anti-EDU. (H-M) Quantification. (H) One-way ANOVA test of 24 hpf EDU+/Dapi comparing WT, Par-3-GFP, and Par-3-S954A-GFP, ns $P > 0.9506$ $R^2 = 0.002891$; WT vs Par-3-GFP, ns $P > 0.9853$, WT vs Par-3-S954A-GFP, ns $P > 0.9853$, and Par-3-GFP vs Par-3-S954A-GFP, ns $P > 0.9853$. (I) One-way ANOVA test of 24 hpf EDU+HuC-/EDU+ comparing WT, Par-3-GFP, and Par-3-S954A-GFP, $P < 0.0033$ ** $R^2 = 0.2791$; WT vs Par-3-GFP, ns $P > 0.9552$, WT vs Par-3-S954A-GFP, ** $P < 0.0097$, and Par-3-GFP vs Par-3-S954A-GFP, ** $P < 0.0076$. (J) One-way ANOVA test of 24 hpf EDU+HuC+/EDU+ comparing WT, Par-3-GFP, and Par-3-S954A-GFP, $P < 0.0033$ ** $R^2 = 0.2791$; WT vs Par-3-GFP, ns $P > 0.9552$, WT vs Par-3-S954A-GFP, ** $P < 0.0097$, and Par-3-GFP vs Par-3-S954A-GFP, ** $P < 0.0076$. (K) One-way ANOVA test of 36 hpf EDU+/Dapi comparing WT, Par-3-GFP, and Par-3-S954A-GFP, $P > 0.1229$ ns $R^2 = 0.1603$; WT vs Par-3-GFP, ns $P > 0.1800$, WT vs Par-3-S954A-GFP, ns $P > 0.1905$, and Par-3-GFP vs Par-3-S954A-GFP, ns $P > 0.9467$. (L) One-way ANOVA test of 36 hpf EDU+HuC-/EDU+ comparing WT, Par-3-GFP, and Par-3-S954A-GFP, $P < 0.0002$ *** $R^2 = 0.5087$; WT vs Par-3-GFP, ns $P > 0.7901$, WT vs Par-3-S954A-GFP, *** $P < 0.0002$, and Par-3-GFP vs Par-3-S954A-GFP, ** $P < 0.0065$. (M) One-way ANOVA test of 36 hpf EDU+HuC+/EDU+ comparing WT, Par-3-GFP, and Par-3-S954A-GFP, $P < 0.0002$ *** $R^2 = 0.5087$; WT vs Par-3-GFP, ns $P > 0.7901$, WT vs Par-3-S954A-GFP, *** $P < 0.0002$, and Par-3-GFP vs Par-3-S954A-GFP, ** $P < 0.0065$. Cryosections of 24 hpf WT, Par-3-GFP, and Par-3-S954A-GFP are from 14, 11, and 13 embryos, respectively. Cryosections of 24 hpf WT, Par-3-GFP-, and Par-3-S954A-GFP are from 10, 6, and 11 embryos, respectively. Both are from 2 repeated experiments.

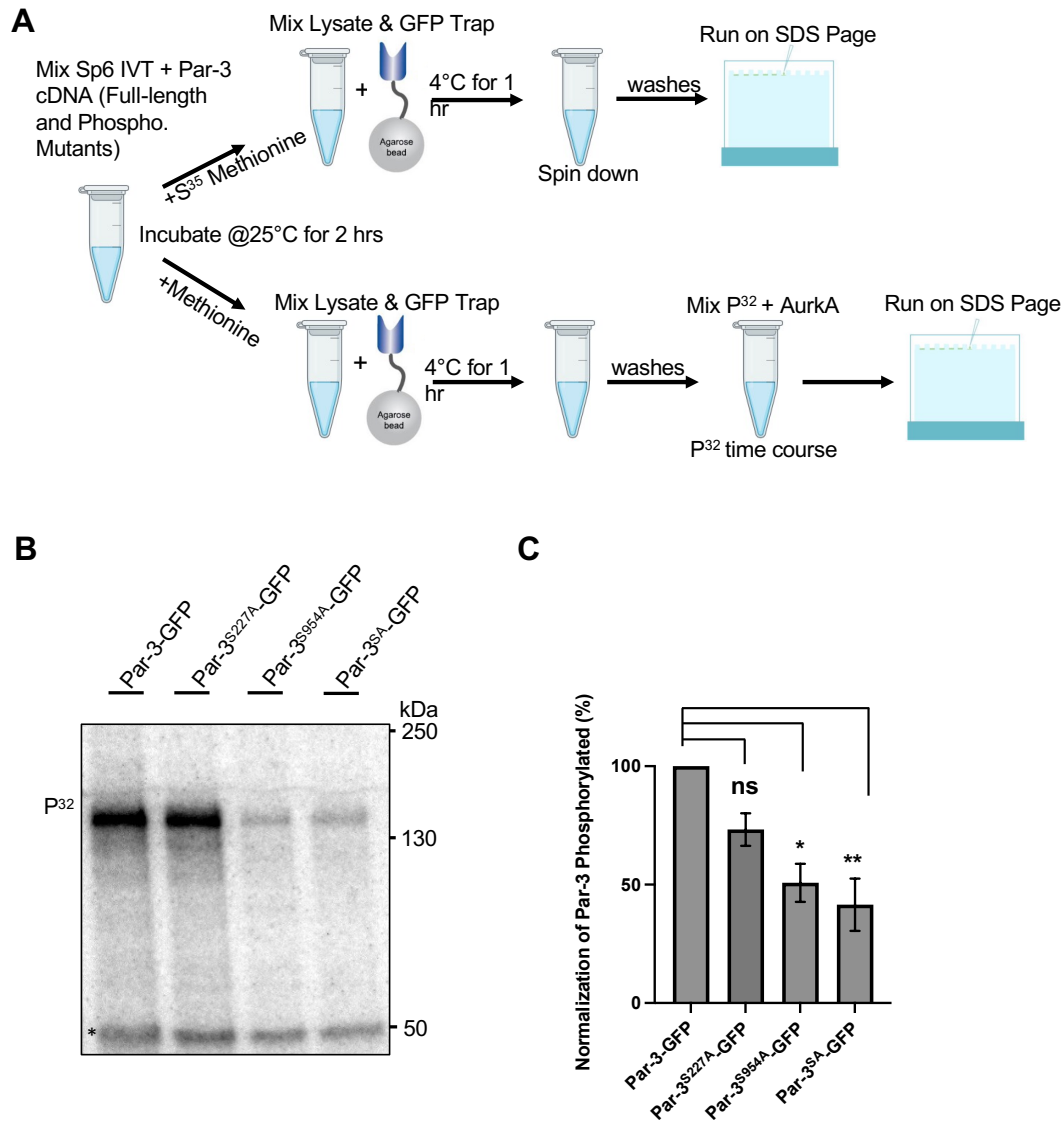


Figure 2.6 Aurora Kinase A directly phosphorylates Par-3 at Ser-954.

(A) Experimental Schematic: in vitro translated Par-3-GFP or Par-3(SA,S954A,SD,S227A)-GFP were immunoprecipitated with GFP-Trap agarose beads, and mixed with 250 nmol of Aurka and $[^{32}P]$ -ATP. Samples were analyzed by SDS-PAGE and autoradiography. (B) Unlabeled Par-3-GFP immunoprecipitates were incubated with Aurka and $[^{32}P]$ -ATP for 5 min, and reaction products were analyzed by SDS-PAGE and autoradiography. Par-3 = 150 kDa. *Aurka autophosphorylation = 50 kDa. (D) Quantification of phosphorylation, normalized to the amount of Par-3 protein. One-way ANOVA-Friedman Test with a Post-Hoc compared to Par-3-GFP, *** $P < 0.0009$, NS=0.8200 Par-3-S227A-GFP, * $P < 0.0411$ Par-3-S954A-GFP, and ** $P < 0.0078$ Par-3-SA-GFP. Results are representative of four independent experiments.

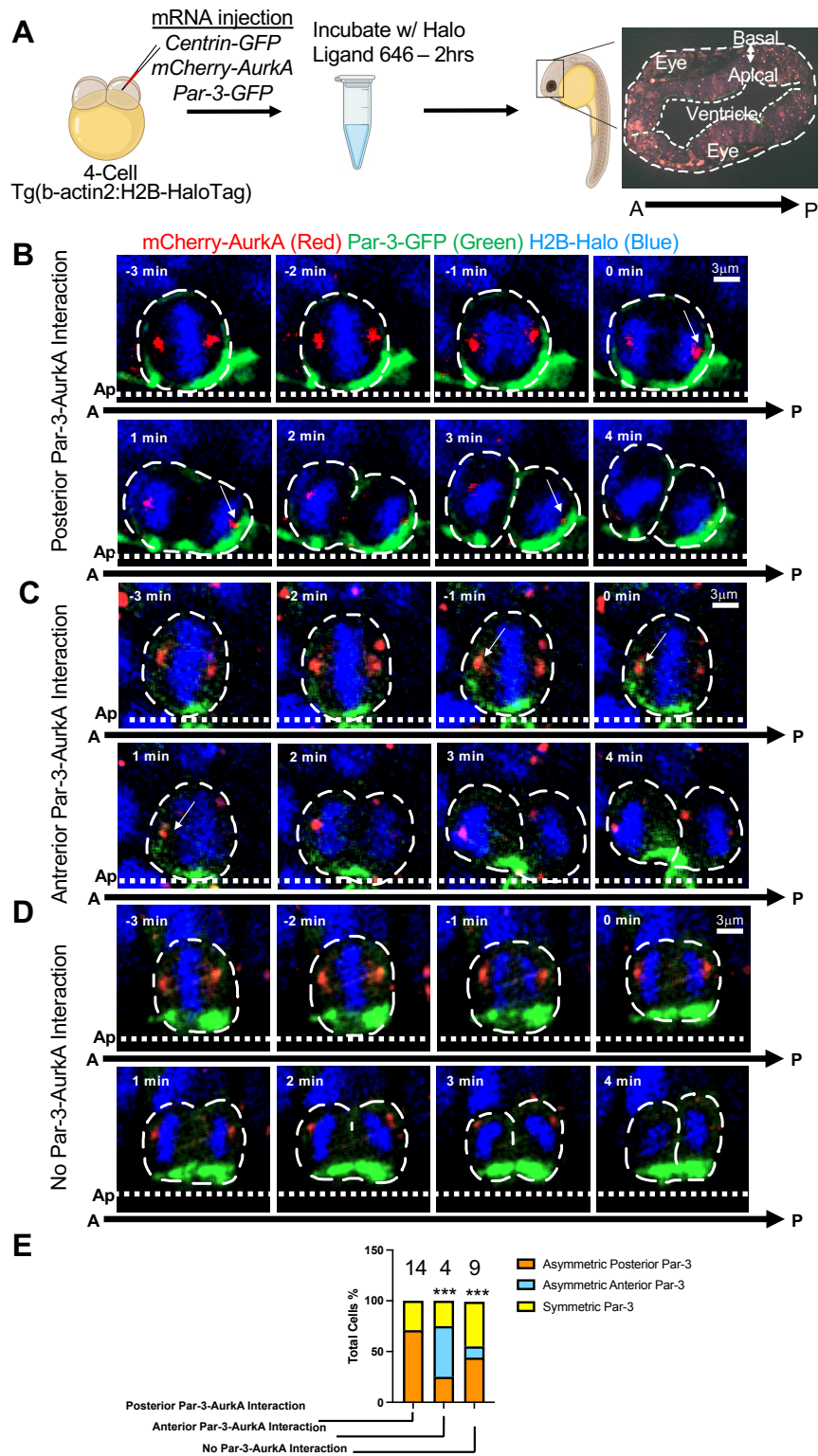


Figure 2.7 In vivo time lapse Imaging reveals cytoplasmic Par-3 in mitotic RGP.

(A) Experimental schematic: mRNA microinjections into 4 cell Tg(b-actin2:H2B-HaloTag) embryos to achieve a transient but sparse labeling. Subsequently, embryos were incubated with Halo Tag ligand-Janelia Flour 646 for two hours prior to live imaging. 24-30 hpf embryos are then mounted on a petri dish with a glass (Figure caption continued on the next page),

(Figure caption continued from the previous page) cover for live confocal imaging. Confocal image of a 40x zebrafish forebrain 28 hpf (dorsal view). The time interval between each volume of z-stacks is 20s, and the total acquisition time is 30 mins. All images shown are the maximum MIP of three confocal z-stacks (1-- μ m z-step) (B-D) In vivo time lapse imaging of Par-3-GFP (100 μ g) and mCherry-AurkA (50 μ g) in mitotic RGP. Arrows indicate AurkA dynamic movements. Par-3-GFP is asymmetrically segregated to the posterior daughter shortly after division and there is AurkA interaction toward the posterior side of the cell. (E) Quantification. Bar graph illustrates the different Par-3-AurkA interactions while Par-3 undergoes asymmetry in RGP. Posterior Par-3-AurkA interactions undergo 71% Par-3 posterior distribution and 29% undergo symmetric. Anterior Par-3-AurkA interactions undergo 25% Par-3 posterior distribution, 50% Par-3 anterior distribution, and 25% symmetric. No Par-3-AurkA interaction undergo 44% Par-3 posterior distribution, 11% Par-3 anterior distribution, and 45% symmetric. **** P<0.0001 (Chi-square 96.70, df=4) The RGP are representative of 11 embryos, 6 repeated experiments, from n=27 horizontally dividing RGP.

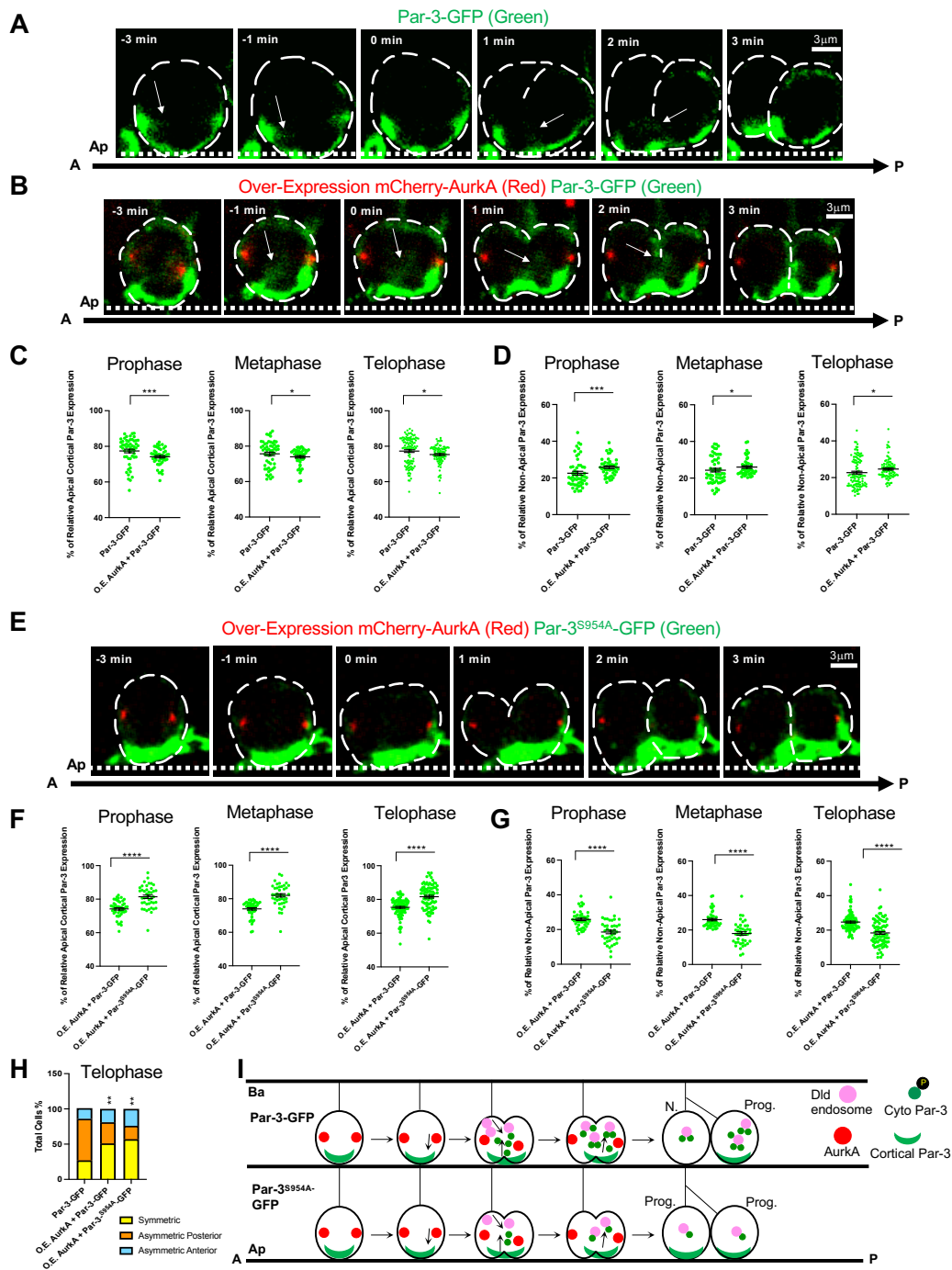


Figure 2.8 Over-expression of AurKA result an increase of Cytoplasmic Par-3 during RGPs ACD.

Time-lapse sequence of images showing of mitotic RGPs undergoing ACD. Time=3 min denotes telophase. All images shown are the maximum MIP of three confocal z-stacks (1- μ m z-step). The time interval between each volume of z-stacks is 20s, and the total acquisition time is 30 min. Images reveal AurKA dynamics during RGPs ACD. Arrows indicate non-apical Par-3 (Cytoplasmic). (A) Time-lapse sequence of images showing Par-3-GFP (GFP only, 200 pg) in mitotic RGPs. (B) Time-lapse sequence of images showing O.E. AurKA + Par-3-GFP (400 pg and 200 pg, respectively) in mitotic RGPs. (Figure caption continued on the next page),

(Figure caption continued from the previous page) (C) Quantification. Apical Cortical Par-3 expression was measured during Prophase, Metaphase, and Telophase in mitotic RGP. O.E. AurkA + Par-3-GFP (n=47 RGPs) reveals a decrease in apical cortical Par-3 expression at prophase, metaphase, and telophase compared to Par-3-GFP (n=55 RGPs). Prophase: $P < 0.0007$ *** Two-tailed Mann Whitney Test (U=759). Metaphase: $P < 0.0497$ * Two-tailed Mann Whitney Test (U=1000). Telophase: $P < 0.0074$ ** Two-tailed Mann Whitney Test (U= 4047). (D) Non-Apical Par-3 (cytoplasmic) expression was measured during Prophase, Metaphase, and Telophase. O.E. AurkA + Par-3-GFP (n=47 RGPs) reveals an increase in Non-Apical Par-3 expression at prophase, metaphase, and telophase compared to Par-3-GFP (n=55 RGPs). Prophase: $P < 0.0007$ *** Two-tailed Mann Whitney Test (U=759). Metaphase: $P < 0.0497$ * Two-tailed Mann Whitney Test (U=1000). Telophase: $P < 0.0074$ ** Two-tailed Mann Whitney Test (U=4047). (E) Time-lapse sequence of images showing O.E. AurkA + Par-3-S954A-GFP (400 pg and 200 pg, respectively) in mitotic RGPs. (F) Quantification. Apical Cortical Par-3 expression was measured during Prophase, Metaphase, and Telophase in mitotic RGP. O.E. AurkA + + Par-3-S954A-GFP (n=42 RGPs) reveals an increase in apical cortical Par-3 expression at prophase, metaphase, and telophase compared to O.E. AurkA + Par-3-GFP (n=47 RGPs). Prophase: $P < 0.0001$ **** Two-tailed Mann Whitney Test (U=366). Metaphase: $P < 0.0001$ **** Two-tailed Mann Whitney Test (U=249). Telophase: $P < 0.0001$ **** Two-tailed Mann Whitney Test (U=1946). (G) Non-Apical Par-3 (cytoplasmic) expression was measured during Prophase, Metaphase, and Telophase. O.E. AurkA + Par-3-GFP (n=47 RGPs) reveals an increase in cytoplasmic Par-3 expression at prophase, metaphase, and telophase compared to O.E. Aurka + Par-3-S954A-GFP (n=42 RGPs). Prophase: $P < 0.0001$ **** Two-tailed Mann Whitney Test (U=366). Metaphase: $P < 0.0001$ **** Two-tailed Mann Whitney Test (U=266). Telophase: $P < 0.0001$ **** Two-tailed Mann Whitney Test (U=1946). The RGPs from Par-3-GFP, O.E. AurkA + Par3-GFP, and O.E. AurkA + Par-3-S954A-GFP are from 10, 14 and 15 embryos, respectively. Additionally, from 6, 3, and 6 repeated experiments, respectively. (H) Quantification. Bar graph showing the percentage of RGPs with different patterns of Par-3. Disruption of Par-3 asymmetry compared to Full-length. Observe more Symmetric divisions. $P < 0.0001$ **** (Chi-square=36.92, df=4). (I) Proposed model. N (Neuron) Prog (Progenitor) Ap (Apical), Ba (Basal) A (anterior), and P (posterior).

2.9 SUPPLEMENTAL FIGURES

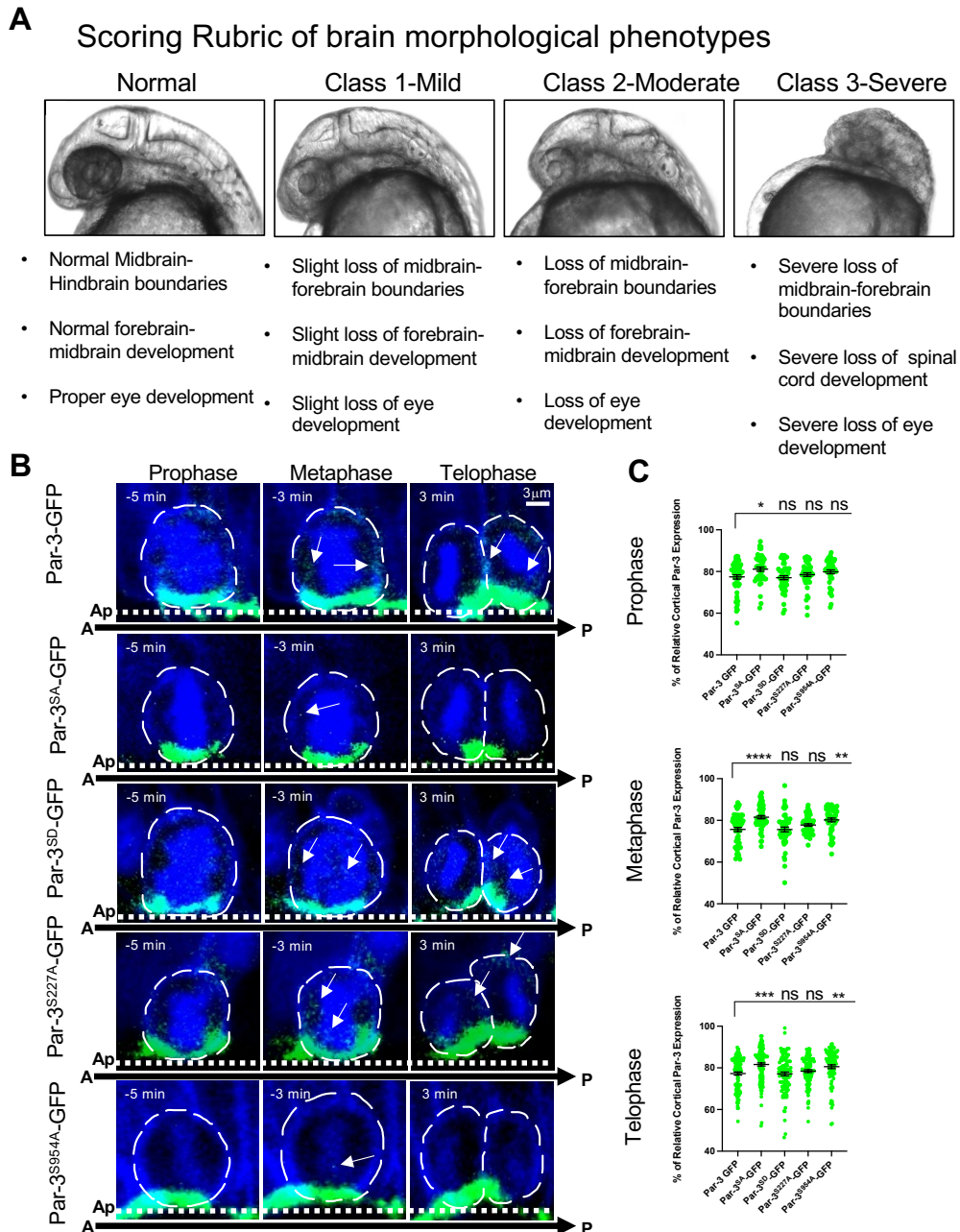


Figure S2.1 Phenotypic scoring rubric and time lapse images of Par-3 phospho-incapable mutants.

(A) Scoring rubric was designed to categorize phenotypes, ranging from Normal development to Severe abnormal development. Each range of development has specific characterizations that assist with scoring phenotypes. (B) Time-lapse sequence of images showing Par-3 and Par-3 phosphor mutants in mitotic RGPs at Prophase, Metaphase, and Telophase. All images shown are the maximum MIP of three confocal z-stacks (Figure caption continued on the next page),

(Figure caption continued from the previous page) (1- μ m z-step). The time interval between each volume of z-stacks is 20s, and the total acquisition time is 30 min. Time = 3 min denotes telophase. (C) Quantification. Relative cortical Par-3 expression was measured at prophase, metaphase, and telophase using Fiji. One way ANOVA Test with a Post-Hoc comparing to control (Par-3-GFP), Prophase: Par-3-GFP (N=54), Par-3-SA-GFP (N=45), Par-3-SD-GFP (N=49), Par-3-S227A-GFP (N=49), and Par-3-S954A-GFP (N=44). P=0.0163, *, R2: 0.04954. Par-3-SA-GFP *P<0.0247, Par-3-SD-GFP NS P>0.7778, Par-3-S227A-GFP NS P>0.6509, and Par-3-S954A-GFP NS P>0.1999. Metaphase: Par-3-GFP (N=55), Par-3-SA-GFP (N=55), Par-3-SD-GFP (N=50), Par-3-S227A-GFP (N=50), and Par-3-S954A-GFP (N=44). P=<0.0001 ****, R2: 0.1271. Par-3-SA-GFP ****P<0.0001, Par-3-SD-GFP NS P >0.9999, Par-3-S227A-GFP P>0.2780, and Par-3-S954A-GFP **P<0.0018. Telophase: Par-3-GFP (N=56), Par-3-SA-GFP (N=56), Par-3-SD-GFP (N=50), Par-3-S227A-GFP (N=50), and Par-3-S954A-GFP (N=44). P<0.0001 ****, R2: 0.04951. Par-3-SA-GFP ***P<0.0003, Par-3-SD-GFP NS P>0.9994, Par-3-S227A-GFP NS P>0.6901, and Par-3-S954A-GFP **P<0.0147. The RGs from Par-3-GFP, Par-3-SA-GFP, Par-3-S954A-GFP, Par-3-SD-GFP, and Par-3-S227A-GFP are from 16, 16, 13, 15, and 13 embryos, respectively, in 9, 9, 7, 7, and 6 repeated experiments, respectively.

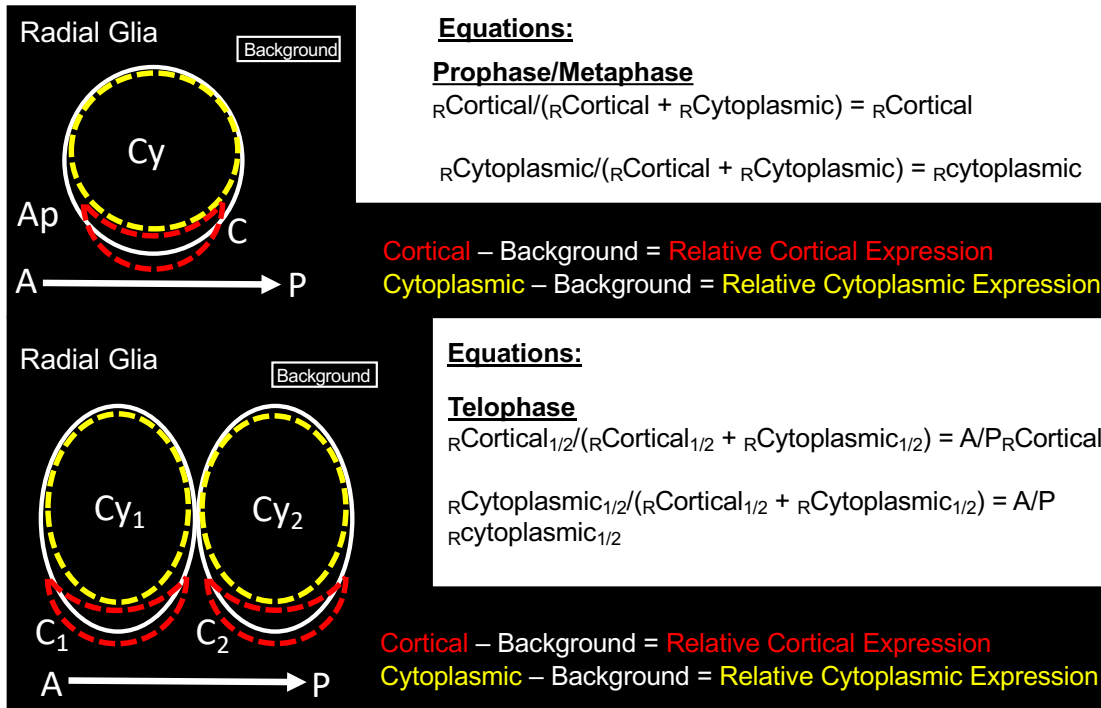


Figure S2.2 Schematic of Calculating Relative Cytoplasmic-Cortical Par-3 expression during RGP ACD.

(A) To calculate Cytoplasmic-Cortical Par-3 expression in RGPs during Prophase/Metaphase, the Par-3 apical cortex is measured (dotted red), the Par-3 cytoplasmic (dotted yellow), and the background is measured too. Next, the relative Par-3 intensity expression of both apical cortical and cytoplasmic is subtracted from the background. $R_{Cortical}$ is divided over the total $R_{Cortical} + R_{Cytoplasmic}$, which will give the $R_{Cortical}$ at prophase/metaphase. $R_{Cytoplasmic}$ is calculated the same way. Upon the completion telophase, anterior and posterior $R_{Cortical}$ and $R_{Cytoplasmic}$ are measured and calculated as described above. 1/2 denotes the two dividing pairs. R (Relative), Cy (Cytoplasmic), C (Cortical), A (Anterior), P (Posterior), Ap (Apical).

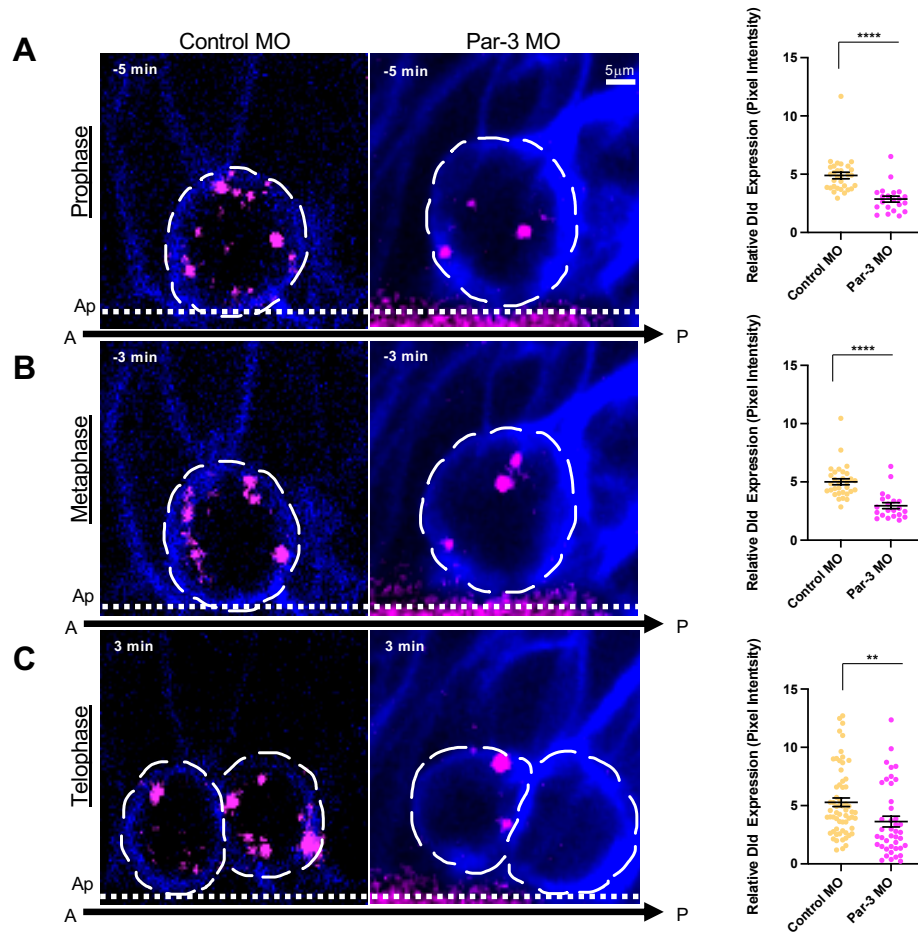


Figure S2.3 Par-3 Morphant results in reduction of Dld Expression.

One- to four-cell stage Tg[ef1a-MyrTdTTomato] embryos (pseudo-colored in blue) embryos were injected with Par-3 MO or control MO. Embryos were raised and imaged around 28 hpf. Time-lapse sequence of images showing of mitotic RGPs. Time = 3 min denotes telophase. All images shown are the maximum MIP of five confocal z-stacks (1- μ m z-step). The time interval between each volume of z-stacks is 30s, and the total acquisition time is 30 min. **(A)** Prophase: time lapse images of Control MO and Par-3 MO **(B)** Metaphase: time lapse images of Control MO and Par-3 MO. **(C)** Telophase: time lapse images of Control MO and Par-3 MO. Quantification **(A-C)**. Scatter plots reveals at prophase, metaphase, and telophase a loss of Dld expression in Par-3 MO dividing RGPs which is statistically significant compared to Control MO. Two-tailed unpaired T-test; Prophase: **** $P < 0.0001$ ($t = 5.068$, $df = 50$). Metaphase: **** $P < 0.0001$ ($t = 5.410$, $df = 50$). Telophase: ** $P < 0.0063$ ($t = 2.792$, $df = 102$). Ap (Apical), A (anterior), and P (posterior). RGPs are from 9 embryos and from 6 repeated experiments.

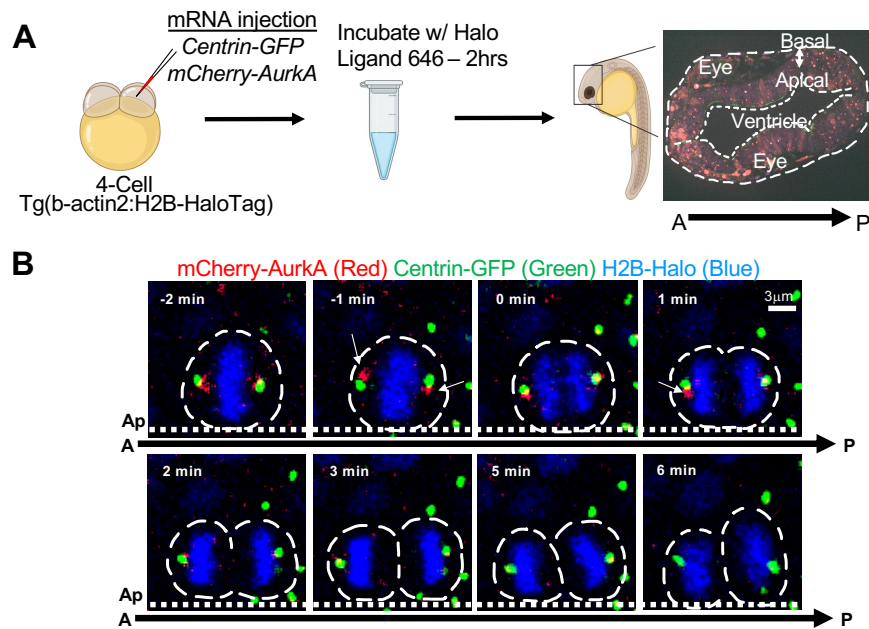


Figure S2.5 In vivo time-lapse imaging reveal Aurka in mitotic RGPs.

(A) Experimental schematic: mRNA microinjections into 4 cell Tg(b-actin2:H2B-HaloTag) embryos to achieve a transient but sparse labeling. Subsequently, embryos were incubated with Halo Tag ligand-Janelia Flour 646 for two hours prior to live imaging. 24-30 hpf embryos are then mounted on a petri dish with a glass cover for live confocal imaging. Confocal image of a 40x zebrafish forebrain 28 hpf (dorsal view). The time interval between each volume of z-stacks is 20s, and the total acquisition time is 30 mins. All images shown are the maximum MIP of three confocal z-stacks (1-- μ m z-step) (B) In vivo time lapse imaging of Centrin-GFP (100 pg) and mCherry-Aurka (50 pg) in mitotic RGPs. Ap (Apical), A (anterior), and P (posterior). RGPs are from 9 embryos and from 6 repeated experiments. Arrows indicate co-localization.

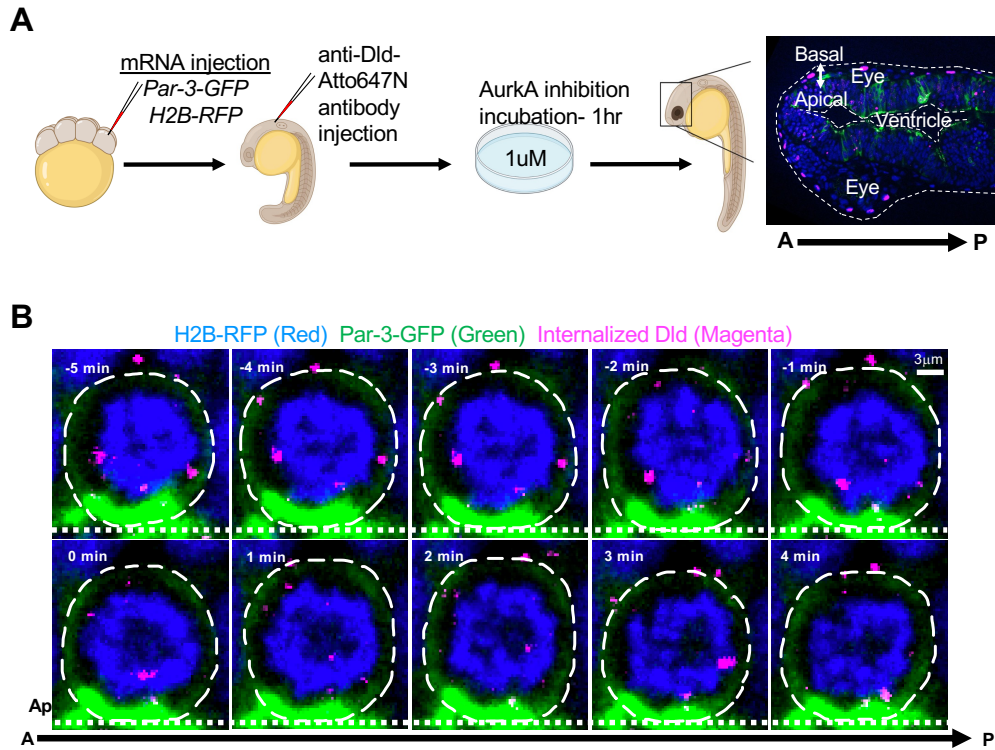


Figure S2.6 1uM inhibition of AurkA during RGP ACD prevents cell cycle progression.

(A) Experimental schematic; mRNA injections (200 pg) at 16/32-cell to achieve sparse labeling of Par-3 and H2B. Embryos are then incubated until 20 hpf, which Dld antibody uptake assay is performed in the hindbrain. Embryos are then incubated until 1 hour prior to imaging, which then embryos are transferred to a small petri dish containing 1uM of MK-5108, AurkA inhibitor. 24-30 hpf zebrafish forebrain region is imaged. A zoomed in Confocal image of a 40x zebrafish forebrain 28 hpf (Dorsal-view). (B) Time-lapse sequence of confocal images showing of mitotic RGPs. Time=3 min denotes telophase, but RGPs are unable to divide, due to AurkA inhibitor. All images shown are the maximum MIP of three confocal z-stacks (1-µm z-step). Ap (Apical), A (anterior), and P (posterior). The RGPs are representative of 5 embryos, 2 experiments.

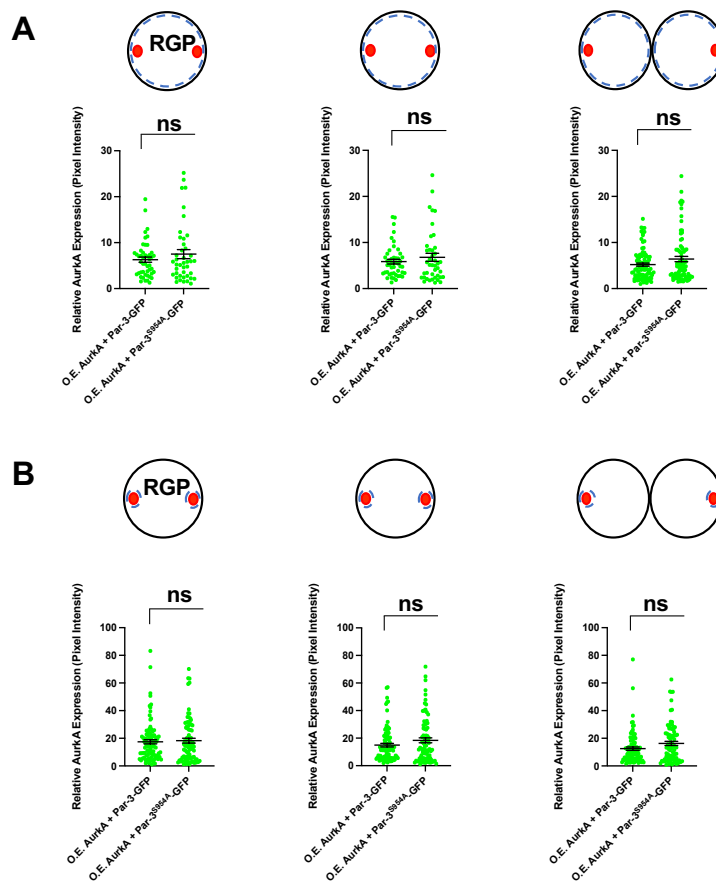


Figure S2.7 Normalization and validation of Over-expression of AurkA.

To validate and normalize the over-expression of AurkA between conditions, two modes of measurement were conducted (A) AurkA expression intensity was measured in RGP cells at prophase, metaphase, and telophase by measuring the entire cell. Two-tailed unpaired T-test; Prophase: O.E. AurkA + Par-3-GFP vs O.E. AurkA + Par-3-S954A-GFP, NS $P > 0.2842$ ($t = 1.078$, $df = 87$). Two-tailed unpaired T-test; Metaphase: O.E. AurkA + Par-3-GFP vs O.E. AurkA + Par-3-S954A-GFP, NS $P > 0.3401$ ($t = 0.9592$, $df = 87$). Two-tailed unpaired T-test; Telophase: O.E. AurkA + Par-3-GFP vs O.E. AurkA + Par-3-S954A-GFP, NS $P > 0.0612$ ($t = 1.884$, $df = 176$). (B) AurkA expression intensity was measured in RGP cells at prophase, metaphase, and telophase by measuring the AurkA expression within the cell. Two-tailed unpaired T-test; Prophase: O.E. AurkA + Par-3-GFP vs O.E. AurkA + Par-3-S954A-GFP, NS $P > 0.7089$ ($t = 0.3739$, $df = 176$). Two-tailed unpaired T-test; Metaphase: O.E. AurkA + Par-3-GFP vs O.E. AurkA + Par-3-S954A-GFP, NS $P > 0.1133$ ($t = 1.591$, $df = 176$). Two-tailed unpaired T-test; Telophase: O.E. AurkA + Par-3-GFP vs O.E. AurkA + Par-3-S954A-GFP, NS $P > 0.1356$ ($t = 1.972$, $df = 176$).

2.8 REFERENCES

1. Knoblich, J.A. (2010). Asymmetric cell division: recent developments and their implications for tumour biology. *Nat Rev Mol Cell Biol* 11. 10.1038/nrm3010.
2. Yong, K.J., and Yan, B. (2011). The relevance of symmetric and asymmetric cell divisions to human central nervous system diseases. Preprint, 10.1016/j.jocn.2010.08.023 10.1016/j.jocn.2010.08.023.
3. Li, Z., Zhang, Y.Y., Zhang, H., Yang, J., Chen, Y., and Lu, H. (2022). Asymmetric Cell Division and Tumor Heterogeneity. Preprint at Frontiers Media S.A., 10.3389/fcell.2022.938685 10.3389/fcell.2022.938685.
4. Florian, M.C., and Geiger, H. (2010). Concise review: Polarity in stem cells, disease, and aging. Preprint, 10.1002/stem.481 10.1002/stem.481.
5. Aranda, V., Nolan, M.E., and Muthuswamy, S.K. (2008). Par complex in cancer: a regulator of normal cell polarity joins the dark side. *Oncogene* 27. 10.1038/onc.2008.340.
6. Etemad-Moghadam, B., Guo, S., and Kemphues, K.J. (1995). Asymmetrically distributed PAR-3 protein contributes to cell polarity and spindle alignment in early *C. elegans* embryos. *Cell* 83. 10.1016/0092-8674(95)90187-6.
7. Guo, S., and Kemphues, K.J. (1996). Molecular genetics of asymmetric cleavage in the early *Caenorhabditis elegans* embryo. *Curr Opin Genet Dev* 6. 10.1016/S0959-437X(96)80061-X.
8. Guo, S., and Kemphues, K.J. (1995). *par-1* a Gene Required for Establishing Polarity in

C. elegans Embryos, Encodes a Putative Ser/Thr Kinase That Is Asymmetrically Distributed.

9. Rose, L.S., and Kemphues, K.J. (1998). EARLY PATTERNING OF THE *C. ELEGANS* EMBRYO.
10. von Trotha, J.W., Campos-Ortega, J.A., and Reugels, A.M. (2006). Apical localization of ASIP/PAR-3:EGFP in zebrafish neuroepithelial cells involves the oligomerization domain CR1, the PDZ domains, and the C-terminal portion of the protein. *Developmental Dynamics* 235. 10.1002/dvdy.20715.
11. Tawk, M., Araya, C., Lyons, D.A., Reugels, A.M., Girdler, G.C., Bayley, P.R., Hyde, D.R., Tada, M., and Clarke, J.D.W. (2007). A mirror-symmetric cell division that orchestrates neuroepithelial morphogenesis. *Nature* 446. 10.1038/nature05722.
12. Alexandre, P., Reugels, A.M., Barker, D., Blanc, E., and Clarke, J.D.W. (2010). Neurons derive from the more apical daughter in asymmetric divisions in the zebrafish neural tube. *Nat Neurosci* 13. 10.1038/nn.2547.
13. Bultje, R.S., Castaneda-Castellanos, D.R., Jan, L.Y., Jan, Y.-N., Kriegstein, A.R., and Shi, S.-H. (2009). Mammalian Par3 Regulates Progenitor Cell Asymmetric Division via Notch Signaling in the Developing Neocortex. *Neuron* 63. 10.1016/j.neuron.2009.07.004.
14. Dong, Z., Yang, N., Yeo, S.-Y., Chitnis, A., and Guo, S. (2012). Intralineage Directional Notch Signaling Regulates Self-Renewal and Differentiation of Asymmetrically Dividing Radial Glia. *Neuron* 74. 10.1016/j.neuron.2012.01.031.
15. Kressmann, S., Campos, C., Castanon, I., Fürthauer, M., and González-Gaitán, M. (2015). Directional Notch trafficking in Sara endosomes during asymmetric cell division

- in the spinal cord. *Nat Cell Biol* 17, 333–339. 10.1038/ncb3119.
16. Mizutani, K.I., Yoon, K., Dang, L., Tokunaga, A., and Gaiano, N. (2007). Differential Notch signalling distinguishes neural stem cells from intermediate progenitors. *Nature* 449, 351–355. 10.1038/nature06090.
 17. Williams, S.E., Beronja, S., Pasolli, H.A., and Fuchs, E. (2011). Asymmetric cell divisions promote Notch-dependent epidermal differentiation. *Nature* 470, 353–358. 10.1038/nature09793.
 18. Artavanis-Tsakonas, S., Rand, M.D., and Lake, R.J. (1999). Notch Signaling: Cell Fate Control and Signal Integration in Development.
 19. Gaiano, N., and Fishell, G. (2002). The role of Notch in promoting glial and neural stem cell fates. Preprint, 10.1146/annurev.neuro.25.030702.130823
10.1146/annurev.neuro.25.030702.130823.
 20. Halaoui, R., and McCaffrey, L. (2015). Rewiring cell polarity signaling in cancer. *Oncogene* 34. 10.1038/onc.2014.59.
 21. Taylor, M.D., Poppleton, H., Fuller, C., Su, X., Liu, Y., Jensen, P., Magdaleno, S., Dalton, J., Calabrese, C., Board, J., et al. (2005). Radial glia cells are candidate stem cells of ependymoma. *Cancer Cell* 8. 10.1016/j.ccr.2005.09.001.
 22. Liu, W.A., Chen, S., Li, Z., Lee, C.H., Mirzaa, G., Dobyns, W.B., Ross, M.E., Zhang, J., and Shi, S.H. (2018). PARD3 dysfunction in conjunction with dynamic HIPPO signaling drives cortical enlargement with massive heterotopia. *Genes Dev* 32, 763–780. 10.1101/gad.313171.118.

23. Xiang Zhao, Jason Q. Garcia, and Kai Tong, Xingye Chen, Bin Yang, Qi Li, Zhipeng Dai, Xiaoyu Shi, Ian B. Seiple, Bo Huang, S.G. (2021). Polarized endosome dynamics engage cytosolic Par-3 and dynein during asymmetric division. *Sci Adv*.
24. Coumailleau, F., Fürthauer, M., Knoblich, J.A., and González-Gaitán, M. (2009). Directional Delta and Notch trafficking in Sara endosomes during asymmetric cell division. *Nature* 458, 1051–1055. 10.1038/nature07854.
25. Li, B., Kim, H., Beers, M., and Kemphues, K. (2010). Different domains of *C. elegans* PAR-3 are required at different times in development. *Dev Biol* 344, 745–757. 10.1016/j.ydbio.2010.05.506.
26. Derivery, E., Seum, C., Daeden, A., Loubéry, S., Holtzer, L., Jülicher, F., and Gonzalez-Gaitan, M. (2015). Polarized endosome dynamics by spindle asymmetry during asymmetric cell division. *Nature* 528, 280–285. 10.1038/nature16443.
27. Holly, R.W., and Prehoda, K.E. (2019). Phosphorylation of Par-3 by Atypical Protein Kinase C and Competition between Its Substrates. Preprint at Cell Press, 10.1016/j.devcel.2019.05.002 10.1016/j.devcel.2019.05.002.
28. Holly, R.W., Jones, K., and Prehoda, K.E. (2020). A Conserved PDZ-Binding Motif in aPKC Interacts with Par-3 and Mediates Cortical Polarity. *Current Biology* 30, 893-898.e5. 10.1016/j.cub.2019.12.055.
29. Lin, D., Edwards, A.S., Fawcett, J.P., Mbamalu, G., Scott, J.D., and Pawson, T. (2000). A mammalian PAR-3-PAR-6 complex implicated in Cdc42/Rac1 and aPKC signalling and cell polarity.
30. Morais-de-Sá, E., Mirouse, V., and St Johnston, D. (2010). aPKC Phosphorylation of

- Bazooka Defines the Apical/Lateral Border in *Drosophila* Epithelial Cells. *Cell* 141, 509–523. 10.1016/j.cell.2010.02.040.10.1523/JNEUROSCI.2216-12.2012.
31. Motegi, F., Zonies, S., Hao, Y., Cuenca, A.A., Griffin, E., and Seydoux, G. (2011). Microtubules induce self-organization of polarized PAR domains in *Caenorhabditis elegans* zygotes. *Nat Cell Biol* 13, 1361–1367. 10.1038/ncb2354.
 32. Dickinson, D.J., Schwager, F., Pintard, L., Gotta, M., and Goldstein, B. (2017). A Single-Cell Biochemistry Approach Reveals PAR Complex Dynamics during Cell Polarization. *Dev Cell* 42, 416-434.e11. 10.1016/j.devcel.2017.07.024.
 33. Jeon, H.-Y., and Lee, H. (2013). Depletion of Aurora-A in zebrafish causes growth retardation due to mitotic delay and p53-dependent cell death. *FEBS Journal* 280. 10.1111/febs.12153.
 34. Wirtz-Peitz, F., Nishimura, T., and Knoblich, J.A. (2008). Linking Cell Cycle to Asymmetric Division: Aurora-A Phosphorylates the Par Complex to Regulate Numb Localization. *Cell* 135, 161–173. 10.1016/j.cell.2008.07.049.
 35. Khazaei, M.R., and Püschel, A.W. (2009). Phosphorylation of the Par Polarity Complex Protein Par3 at Serine 962 Is Mediated by Aurora A and Regulates Its Function in Neuronal Polarity. *Journal of Biological Chemistry* 284. 10.1074/jbc.M109.055897.
 36. Zhao, X., Garcia, J., Royer, L.A., and Guo, S. (2022). Colocalization Analysis for Cryosectioned and Immunostained Tissue Samples with or without Label Retention Expansion Microscopy (LR-ExM) by JACoP. *Bio Protoc* 12. 10.21769/BioProtoc.4336.
 37. Tong, K., Wagle, M., and Guo, S. (2019). Antibody uptake assay in the embryonic zebrafish forebrain to study notch signaling dynamics in neural progenitor cells in vivo. In

Methods in Molecular Biology (Humana Press Inc.), pp. 273–281.
10.1007/7651_2017_22.

38. Zhao, X., and Guo, S. (2023). Antibody Uptake Assay for Tracking Notch/Delta Endocytosis During the Asymmetric Division of Zebrafish Radial Glia Progenitors. *Journal of Visualized Experiments* 2023. 10.3791/65030.
39. Petri, K., Zhang, W., Ma, J., Schmidts, A., Lee, H., Horng, J.E., Kim, D.Y., Kurt, I.C., Clement, K., Hsu, J.Y., et al. (2022). CRISPR prime editing with ribonucleoprotein complexes in zebrafish and primary human cells. *Nat Biotechnol* 40, 189–193. 10.1038/s41587-021-00901-y.
40. Yang, N., Dong, Z., and Guo, S. (2012). Fezf2 regulates multilineage neuronal differentiation through activating basic helix-loop-helix and homeodomain genes in the zebrafish ventral forebrain. *Journal of Neuroscience* 32, 10940–10948. 10.1523/JNEUROSCI.2216-12.2012.
41. Leontovich, A.A., Salisbury, J.L., Veroux, M., Tallarita, T., Billadeau, D., McCubrey, J., Ingle, J., Galanis, E., and D'Assoro, A.B. (2013). Inhibition of Cdk2 activity decreases Aurora-A kinase centrosomal localization and prevents centrosome amplification in breast cancer cells. *Oncol Rep* 29, 1785–1788. 10.3892/or.2013.2313.
42. Dagher, J., Dugay, F., Rioux-Leclercq, N., Verhoest, G., Oger, E., Bensalah, K., Cabillic, F., Jouan, F., Kammerer-Jacquet, S.F., Fergelot, P., et al. (2014). Cytoplasmic PAR-3 protein expression is associated with adverse prognostic factors in clear cell renal cell carcinoma and independently impacts survival. *Hum Pathol* 45, 1639–1646. 10.1016/j.humpath.2014.03.018.

43. Kimmel, C.B., Ballard, W.W., Kimmel, S.R., Ullmann, B., and Schilling, T.F. (1995). Stages of embryonic development of the zebrafish. *Developmental Dynamics* 203, 253–310. 10.1002/aja.1002030302.
44. Wan, Y., Wei, Z., Looger, L.L., Koyama, M., Druckmann, S., and Keller, P.J. (2019). Single-Cell Reconstruction of Emerging Population Activity in an Entire Developing Circuit. *Cell* 179, 355-372.e23. 10.1016/j.cell.2019.08.039.
45. Wei, X., Cheng, Y., Luo, Y., Shi, X., Nelson, S., and Hyde, D.R. (2004). The zebrafish *Pard3* ortholog is required for separation of the eye fields and retinal lamination. *Dev Biol* 269, 286–301. 10.1016/j.ydbio.2004.01.017.
46. Dong, Z., Wagle, M., and Guo, S. (2011). Time-lapse live imaging of clonally related neural progenitor cells in the developing zebrafish forebrain. *Journal of Visualized Experiments*. 10.3791/2594.
47. Zolessi, F.R., Poggi, L., Wilkinson, C.J. et al. Polarization and orientation of retinal ganglion cells in vivo. *Neural Dev* 1, 2 (2006). <https://doi.org/10.1186/1749-8104-1-2>

**CHAPTER 3: Creating Inclusive Research Laboratory Environments:
Findings from the DE-SILO Intervention**

3.1 INTRODUCTION

Diversity is crucial to scientific innovation: research demonstrates underrepresented investigators produce more novel research, generate more innovative solutions to problems, and publish more influential scientific papers than majority researchers (1,2). Despite this, persistent and systemic racial and ethnic stratification within the academic science has been well-documented, and the innovations of underrepresented researchers are less likely to earn them academic positions (1). These challenges for entry and retention occur at all levels of scientific training, beginning with science, technology, engineering and mathematics (STEM) education (3). For early career researchers, researchers of color are more likely to be saddled with service work that is undervalued in promotion and tenure review, and they earn less than their white colleagues (4,5,6). In the wake of ongoing injustices and disparities in the COVID-19 pandemic and continued extrajudicial killings by police in the US during 2020, many academic science communities began to have widespread discussions about system racism, how scientific fields were implicated, and how to strengthen diversity, equity, and inclusion (DEI) programming. Across the US, academic institutions, funding agencies, and scientific journals released statements on systemic racism and launched diversity and inclusion initiatives that promised to address longstanding disparities and institutional harms (7,8,9). Commentaries were published in high profile science journals (10,11) and higher education outlets (12), and many field specific journals launched special issues on related topics (13). This moment prompted discussions about longstanding issues, and the particular paradox that emerges around diversity and inclusion and, specifically, racism, in academic science. That is, while underrepresented researchers are understood to be integral to scientific innovation, it is these same researchers who face obstacles to participation in the scientific enterprise and experience ongoing harm in institutional settings (3).

While attention to diversity efforts seemed to surge in 2020, the issues that were being discussed were not new issues. For decades, there have been efforts to increase representation and inclusion among STEM researchers and in the scientific workforce more generally, and scholars have long documented disparities and institutional racism in university science (14).

As initiatives have been adopted over the last several decades, they have become understood as essential for promoting workplace environments that value and respect workers from diverse backgrounds. Importantly, although “diversity” can signal a range of characteristics (and their intersections), such as race and ethnicity, gender, living with disabilities, neurodivergence, sexual orientation, and socioeconomic status, it is often used narrowly to signal race and ethnic diversity (15).

Diversity, equity and inclusion (DEI) work typically involves identifying and addressing the barriers in a given workplace that prevent underrepresented individuals from fully participating and feeling included in an organization. DEI efforts typically include things like administering workplace climate surveys, requiring bias trainings for current employees, or establishing affinity groups that strive to improve workplace culture. Recent estimates suggest that nearly all US companies have some type of diversity program, such as specific recruitment programs, bias trainings, or professional development or affinity groups (16).

Indeed, particularly in the wake of 2020, DEI training has also become a valuable industry: a 2022 industry report valued the DEI industry at \$9.4 billion (Global Industry organizational outcomes (e.g., innovation or productivity in the workplace) rather than how, in popular discourse, attention to diversity often takes on the form of multicultural Analysts, 2023). Diversity has been branded as a universal good; it is “good for organizations, good for profits, good for learning, and even good for white people” (15).

While such initiatives have become ubiquitous, whether and how they create meaningful change in the day-to-day experiences of organization members remains an open empirical question. In part, such trainings and activities can make harms seem like exceptions, rather than every day, micro-occurrences that compound over time. Or, trainings are “recommended” but not “required,” and thus only those who already care about such issues are inclined to participate. Moreover, sociological research demonstrates that the reasons for valuing diversity matter for taking action: when organization members only value diversity as a way of improving explicitly addressing inequality, members of the organization are less likely to act in accordance with this belief (16). This mirrors earlier research that shows how, in popular discourse, attention to diversity often takes on the form of multicultural celebration and “happy talk.” Put simply, when discussed in the abstract, people value diversity; yet people avoid acknowledging and addressing inequality (17). They show how diversity becomes “happy talk” that promotes the positives of diversity in the abstract but evades discussion of inequality or specific action to rectify disparities (17).

In effect, a happy talk approach to DEI initiatives may look good at a superficial level, but do little to change the daily experiences of those participating in a given organization. This background helps to contextualize the complex terrain upon which DEI efforts operate, and illuminate the challenges to achieving meaningful impact in institutional settings. In academic science specifically, this is compounded by another cultural norm: social concerns are largely bracketed from scientific work in the laboratory. Science and technology studies (STS) scholars have articulated the boundary work that divides science from society, leading to the exclusion of “the social” in scientific spaces. Boundaries between the kinds of concerns that are discussed in laboratory meetings and in the professional setting, and those that are relegated to personal and social concerns, often makes it hard for laboratory workers to voice workplace and interpersonal concerns (18). ii This is a particularly important consideration when it comes to

DEI efforts, because it requires that academic scientists acknowledge that the social structures that shape broader society also exist within and shape the scientific setting and the people conducting the scientific work. This complicates deeply held notions of meritocracy that are pervasive in STEM fields (19). As academic researchers in multiple fields and at disparate institutions, we each observed this current moment in which academic science as an institution was grappling systemic racism and the response of academic science from different vantage points: as postdoctoral researchers and graduate students in laboratories, a sociologist and laboratory ethnographer, and as a DEI administrator. Witnessing this context and discontented with the lack of sustained engagement on discussions of racism, diversity, and inclusion in the aftermath of 2020, we developed an initiative to bring these conversations into everyday practice, leveraging the sociological and STS scholarship to create a toolkit for STEM researchers to support sustained engagement. We titled this The DE-SILO Project (Diversity, Equity, and Sociology training in Laboratory Organizations). In this article, we discuss our experiences piloting DE-SILO in four labs at research intensive institutions (R1s) in the United States. We explain the DE-SILO Project concept and method, discuss lessons learned through implementation, and finally turn to future directions and recommendations for researchers attempting similar efforts.

3.2 THE DE-SILO PROJECT: MATERIALS AND METHODS

The premise of the DE-SILO Project was simple: to prepare a toolkit that laboratory groups could use in order to engage in sustained DEI discussions that would lower the “burden of entry” to these conversations. The DE-SILO Project includes course modules, facilitation guides, and a resource repository for participating laboratories. The course modules focus on educational and community building content (see Table 1). The four core curriculum modules were designed

with the objective of facilitating group understanding of DEI topics and how STEM fields are involved in and impacted by them. They lay an empirical foundation for understanding the depth and breadth of these concerns, with the intent of (1) convincing laboratory groups that diversity, racism, and inclusion are important social issues, (2) that they have been empirically researched and are topics in which expert knowledge exists in abundance, and (3) that they are relevant to the lab's field. In addition to the core curriculum modules, three community building modules were designed with the objective to bring in personal experience of lab members and to attend to the specific institutional environment of the lab. Each of the community building modules encourage specific action to be taken in the community (lab) context. Simply put, the community building modules link the core curriculum modules with specific activities and interventions that bring what might be considered as "abstract" problems into a tangible context. We developed these modules to be implemented on a monthly basis, but timing could be adapted at the lab's discretion. Module content was primarily developed by the sociologist on the team, with feedback from all team members. Each module included a brief, digestible one-page document that outlined the issue being addressed in the module. The one-pager included suggested material for advance preparation, such as a reading, podcast, or short video produced by leading scholars on the topic of interest. Each one-pager also included a reference list for suggested readings for lab members who may be interested in learning more about a given topic. iii Facilitation guides were provided to the facilitators of each lab, who were either postdoctoral researchers or graduate students working in the lab. It was an intentional choice to have a lab member, and not the Principal Investigator (PI) of the lab take the lead on implementing DE-SILO. Given working dynamics, our team thought that having the lab leader, who is in a position of power in the group, lead the discussions might discourage authentic engagement from group members and further reinforce power dynamics. As we later discuss, this decision posed some challenges for implementation and warrants further consideration. A

group discussion guide was provided for facilitators. This guide included open-ended questions to encourage group discussion, and to offer prompts for facilitators in the event that discussion stalled. Facilitators were instructed to use these as a starting point, and to actively listen during group discussion in order to ask follow-up questions inspired by the group discussion. In advance of each DE-SILO module, facilitators emailed the group with an introduction to the module, any required readings or media to the group. Following the completion of the module, facilitators sent out the post-module completion survey. Additionally, to evaluate progress, we asked all facilitators to keep notes on their lab's ongoing process, and we had DE- SILO group meetings quarterly. The sociologist on our team analyzed survey data and conducted semi-structured interviews with facilitators throughout the implementation period.

3.3 IMPLEMENTATION SETTING

Through a pre-implementation survey, lab group members were asked a series of questions about how their labs current level of engagement in DEI efforts, the importance of DEI in their work and day-to-day scientific settings, and about the culture of their lab. In the pre-implementation survey, 70% of respondents reported that they felt DEI issues were important in their scientific work. However, only 50% reported that this was something they thought about on a regular basis. Similarly, the majority of respondents reported that they felt that their labs and institutions valued DEI and that they generally felt comfortable bringing up issues related to DEI that occurred in lab (e.g., microaggressions). All four labs where DE-SILO was piloted had previous exposure to, at a minimum, infrequent DEI discussions. One of the labs had launched a journal club style discussion series, another was in the process of doing so, and the others held previously held optional DEI meetings on an ad hoc basis. Implementation across the four labs was met with varied success. In the following sections, we present major themes from our

experience implementing DE-SILO in lab groups, drawing on data collected through module completion surveys and interviews with facilitators.

3.4 LESSONS LEARNED THROUGH IMPLEMENTATION

3.4.1 Lab leadership shapes the environment and sets the tone.

In laboratory settings, the principal investigator (PI) leads the lab group, and the group is composed of research staff (e.g., staff scientists, technicians) and trainees (e.g., postdoctoral researchers, graduate students, and undergraduate students). As PIs progress in their career, they are not typically in the lab regularly, for instance, on a daily basis performing bench work. PIs typically meet with their lab group on a weekly basis and convene sub-group and individual meetings with lab group members. DE-SILO modules were implemented as part of these lab group meetings, where a portion of the lab meeting was allocated to module discussion or were implemented at specific additional lab meetings. Thus, leadership support for DEI efforts, and DE-SILO specifically, was integral to having lab members attend and participate, and ultimately to its success or failure. One facilitator put it simply, saying “one-hundred percent—you just need PI buy-in.” PI’s support for implementation was just one dimension, however. How a lab’s PI engaged in discussion and set the tone in the lab more generally was also critical to implementation success. One facilitator explained;

For example, as part of our lab diversity statement, I was really interested addressing what action items can we accomplish as a lab? And I was really interested in having it so that our lab participates and helps the public-school community around the university by bringing our expertise, doing basically science outreach. [Our PI] was really for that, and saying that they could also provide funding to let us go to these events and buy materials and supplies to actually do the outreach activities and stuff like that. They’ve been very on board in terms of actually creating this type of environment.

In this case, the PI's commitment to crafting a lab diversity statement and enthusiasm for community outreach signaled to lab group members that he was actively in support of creating a particular kind of lab environment. Of course, this outward signaling did not mean that there were never tensions in the group about lab decisions. The facilitator continued:

There are sometimes where there does seem to be a bit of a disagreement on how best to proceed from a PI perspective versus a postdoc or grad student perspective. Yeah. Um, and I wouldn't really say that's a barrier or a challenge because I feel like that is part of the goal. Like the discussion is to kind of voice each other's opinions and then you know, help each other, see the other side of things. So, I think that was actually a good thing, but in the moment it does feel awkward and a little hard to navigate.

While this facilitator thought surfacing such tensions were "part of the goal," for others such tensions were less productive. For instance, one facilitator felt that their PI's engagement with DEI efforts were superficial. They explained:

My PI [has] never stood in the way of me or anyone else implementing DEI conversations. I appreciate that. It feels [...] performative because he can say that he's having DEI journal clubs or whatever. Of course, I would take this [situation] over, you know, a PI who's like adamantly refusing to take lab time to talk about these things. For sure. But I don't think he feels comfortable like facilitating conversations about it.

While their PI did not outwardly discourage engagement on the topics, and explicitly supported the group to have these discussions, when the DE-SILO discussions occurred, this facilitator often felt that the PI was uncomfortable during the conversations. Similarly, responding to a question about "challenges during the group discussion," one survey respondent reported:

I get the sense that for at least half of the lab, it's already 'revolutionary' to be having DEI discussions in lab meeting, and things don't tend to go beyond that. Because in our lab, there is a strong sense of some of the lab members needing [to] teach the PI about DEI (to varying degrees of success), if we don't get buy-in from the PI on specific actionable changes, it will not happen. Our PI seems to still believe in the myth of "meritocracy" and will frequently pose questions like "where do we draw the line between scientific rigor and performative DEI?" We tend to spend most of our energy addressing these false dichotomies that our PI poses.

In such cases, these efforts veered away from the intent of the discussion, or a discussion that felt meaningful to group members altogether. Another issue emerged around how PIs participated in the conversation. One facilitator explained that while their PI makes a point to engage in these conversations, sometimes it discourages other lab members' participation:

[My PI] has been very supportive. Because it's during lab meeting, he's always there and he's always engaged and actually participated in the conversation, which has been really great. One challenge was sometimes I think my PI was really trying to participate, but it actually became just a conversation between the PI and the presenter. I don't think he was really realizing this, but there's still some level of a power dynamic. Yeah. People don't feel as comfortable countering. Because it's only 15 minutes [of our lab meeting] to get things going quickly, he would often jump in first. And so, I think one kind of challenge is remembering to set the stage and so that it is an inclusive discussion that's, you know, um, a place where everyone can voice their opinion. I think as the meetings have gone on, people have gotten more and more comfortable. So that was, that was more of an issue in the beginning.

Perhaps most challenging, one facilitator felt that their PI's participation in the group discussion undermined the goals of the discussion. They explained:

I didn't feel like it was really a very safe place, which made it seem like it probably wasn't going to be that productive of a discussion. Then also like little incidents kept happening outside of the lab that made it increasingly feel like that. One of the issues that I felt like we faced in the second community building module ["DEI at Our Institution"] was like my PI taking credit for a lot of the DEI initiatives [at the institution]. Which made it hard to talk about like what was needed or what, you know, what was wrong with them or whatever is, you know, like [they were] taking a lot of like pride in, in those and also kind of crediting themselves with doing them even some that my understanding were student led or trainee led. So that was one of the things too that made me feel like, you know, it was just, um, not a productive conversation.

Here we see how power dynamics in the lab can create challenges for the goals of a given module. Without a doubt, support from lab leaders is crucial. Without it, dedicated time in lab meetings (or other scheduled times) would not happen; to be mandatory, it needs to come from leadership. However, this was complicated by these very same power dynamics. How a PI

engaged during conversation shaped the authenticity of them, how and whether group members felt comfortable participating, and the overall productivity and utility of the module discussions. We return to this issue in the discussion.

3.4.2 Routine engagement is key for sustained practice

Studies show that routine engagement is critical to behavioral change in a variety of contexts.^v Hence, when we developed DE-SILO, we envisioned that modules would be completed on a regular basis (monthly or bi-monthly) in order to establish routine practice. For our pilot labs, this consistency helped lab members to both expect it as a routine lab activity, as well as to elevate its importance and ensure that the discussion happened, rather than being treated as secondary to the science. One facilitator explained:

Having a time that's set aside specifically for this is important, whether it's the first 15 minutes of lab meeting or setting aside several lab meetings to do it, or setting aside a separate scheduled time to do it. Whenever we try to do [it] at the end of meetings or if there's a slot that's not filled [in group meeting] or something that's not as specific, then I think it's tough. Because people can always talk for so long about data [...] Specifically setting a time aside for it is important or it won't happen. I think that we've definitely gotten comfortable talking about things like [this] when we set it up as like a time to talk about something.”

Similarly, another facilitator explained:

One thing that was really important is having this be more of like a continuous conversation was really nice. Because it's easier to get into the discussions when this is something that we know is like a standard thing that happens every single week. Yeah, yep. Well, not necessarily every week, but like every other week or once per month.

The frequent nature of these discussions helped not only for lab members to expect it, but also

to enact part of the DE-SILO objective: for lab members to see diversity and inclusion issues as integral parts of and relevant to scientific life. Critically, one facilitator also that it was important in their lab for DEI discussions to “be at the same level of significance” as a lab meeting “focused on the science.” They explained that their lab members struggled with pre-work, expressing that this was a challenging balance to strike:

Also, for our lab, I think making it something short where there's no like pre-work required, but still having it be at the same level of significance as like a lab meeting would be focused on the science [was important]. So it's not just an optional thing that some people come to once a month, but like we're all gonna be there for lab meeting. We're, you know, there's a pretty high expectation to come to lab meeting. And so you're going to be part of these conversations too.

Similarly, other facilitators felt it was important for DE-SILO to not be optional, but rather be an expected part of lab participation. Another explained:

It is important to set the expectations a little bit in the beginning and making it clear that yes, you're going to be there, but you don't have to participate. I think just laying down [...] the ground rules for discussion is good.

Critically, this facilitator emphasized presence for the discussions, not necessarily participation. They recognized that participation was more difficult for some than others, and that there may also be group dynamics that challenge certain group members from active participation.

3.3.3 Meaningful equity and inclusion requires, equitably distributed labor

The final key lesson learned through implementation underscored the well-documented inequities in distribution of DEI labor. Facilitators spoke at length about who takes on this “service” labor, and the challenges of getting lab mates and PIs to sustain engagement with DEI efforts in the lab. One facilitator explained the distribution of “invisible labor” in their lab. They

recollected,

Our lab in general has a problem with like invisible labor and the same people organizing social things, miscellaneous [events for the lab]. It's me and this person who usually do all of it. After we ran [one of the] community modules, I said, "listen, y'all I cannot run these all the time. We don't have to do this if people aren't interested." I can't keep reminding us that we should do these. If no one else is interested in like taking initiative on it then, and like it's not full lab participation. But then our PI said, "no, I think it's important. We should keep doing them." Which I don't know if he just wants to keep saying that we're doing it or like what, but we decided that we'll rotate who [facilitates].

When asked to expand on why labor was distributed this way in the lab, and the resistance of other lab members to leading discussion, the facilitator continued,

I think it still intimidates a lot of people to like, to like take leadership on these conversations because they don't feel like they're like qualified to be leading these conversations. And I think our PI is kind of in that category. No one is [against] having these conversations in this lab and my PI isn't [against] having these conversations. But I guess it's just, like the negative effects of people in general, including my PI feeling like, "oh, I shouldn't, maybe I shouldn't be leading." Then it falls on the person who they think is the expert who is usually a [Black, Indigenous, People of Color] BIPOC person. So, yeah. Generally speaking, I haven't gotten a lot of resistance in having these conversations. It's just more that I wish the labor was more even distributed. And even though I keep like telling everyone "you don't have to be an expert... like I'm not an expert." I think it's still a little bit difficult for people to feel comfortable with like feeling like they can lead a conversation.

As this facilitator explained, group members often felt uncomfortable leading these conversations because they did not consider themselves experts on the topic. Yet this serves to place the burden of leading this work on a small group of lab members, who are often themselves in marginalized positions. This positionality, as the facilitator points out, did not make them "experts" either, or necessarily that they would have the skills training to facilitate such discussions. Similarly, another facilitator explained how learning how to facilitate was a considerable but rewarding challenge for them:

The experience of facilitating is a really interesting experience that we don't get any practice with in STEM. Like we don't even take courses that are very like discussion based, as might be common in, like the humanities. And so going from like leading a

journal discussion or a scientific discussion to one of these is really different and really hard at first. My original concern, or fear essentially was like, how do I even lead one of these discussions? And I think it's been really, really good. Just get practice trying it and seeing what works and what doesn't and like being again in a community where I know it's okay, if I do it terribly. [...] And so if nothing else, regardless of what's being discussed, it's a super good skill that we should have training in.

Equally challenging was that sustained labor—to both participate and prepare materials in advance—proved to be an obstacle to DE-SILO implementation. Facilitators and survey respondents reported that when pre-work was required, such as reading a short article or watching a video, lab members were generally unprepared for module discussions. When asked about particular challenges to module implemented in the post-module survey, multiple respondents noted that their “group was unprepared” which “made conversation more difficult.” While we anticipated this in the DE-SILO, and thus assigned limited pre-work for each module, lack of preparedness certainly placed a higher workload on facilitators to synthesize module material and carry the conversation. Moreover, this changed with time: while lab members and PIs were enthusiastic and supportive of DE-SILO implementation at the outset, this support faded with time.

One facilitator explained, “the lack of support from the PI was an issue. I was backed initially but the PI did not seem to care after one or two discussions, and it was hard to get future modules scheduled.” This facilitator also noted that after the two modules were implemented, with strong lab engagement, that it then became a challenge to get lab members to complete the module pre-work. They continued:

My lab mates seemed excited initially about DE-SILO and its objective but became uninterested after reading was required, no one read it. This became a recurring theme after module 1, majority of my lab mates would come unprepared, meaning not ready to participate or have a discussion. What I gathered from this was that if there is more work to be done, they weren't interested.

It is not surprising that we experienced resistance to sustained engagement, as this very phenomenon was part of what we were attempting to address with the DE-SILO Project. Nonetheless, findings from our pilot show that even when lab groups commit to a program like this, maintaining momentum and engagement from module to module is difficult.

3.4 CONCLUDING REMARKS AND FUTURE CONSIDERATIONS

We learned critical lessons from the DE-SILO Project pilot year that will shape future iterations of the DE-SILO Project. Above all else is the obstacle of adoption and the likelihood that lab groups might implement programming like DE-SILO at all. Given the extant literature, it is reasonable to suspect that only lab groups who are already interested in and committed to DEI issues will be likely to implement this kind of programming, and within those, only those who value diversity explicitly on grounds of addressing inequality will act in accordance (16). As one facilitator put it,

[facilitating] is a lot to ask of somebody in the lab and basically like the problem is that the worse, the worse the situation the lab is, then in the harder it'll be to implement. And the labs that need it most, maybe the most unlikely to do it.

Even in cases where there is PI support, findings from our pilot year show that this is more complicated than simply that. With respect to lab leadership, we learned that consistent PI support is integral to programmatic success. PIs must support requiring engagement from lab members, making DEI discussions/programming understood as an expectation of all lab members. However, we also learned that the expectations of engagement for PIs need to be better articulated. Each PI will have their own style of engagement and shape the group dynamic in particular ways, and it is important to be sensitive to this in implementation because it can serve to undermine the goals of a given module or the project altogether. Navigating this

situation is particularly tricky for facilitators who, in our pilot year, were lab members of the group. It is worth considering how an external facilitator might prove useful to help navigate these power dynamics.

We also learned that routine engagement is critical but requires sustained, additional labor which is both unevenly distributed and often met with resistance. Across our implementation labs, it was our experience that those willing and motivated to bring these discussions to their lab are often those directly affected by inequities. This uneven distribution of labor is not only an obstacle to successful implementation, it is deeper issue that hinders the creation of meaningfully inclusive research environments. While our pilots PIs and lab group members were initially supportive of implementing modules, with time this enthusiasm waned. This resulted in lab members failing to prepare or actively participate in the group discussion, and thus the burden of this work fell on the facilitator more heavily than intended, exacerbating this issue.

3.5 TABLES

Table 3.5.1 Modules

Table 1: Modules

Core Curriculum Module	Module Description
Representation and Diversity in STEM	This module introduces findings from empirical analyses of representation in STEM fields. Introduces lab members to demographic groups that are underrepresented in STEM fields and obstacles that members of these groups may face.
Racism and Anti-Racist Action in STEM	This module offers a discussion of racism in academic science as well as anti-racist efforts taking place in STEM fields.
Science, Technology & the Reproduction of Difference	This module introduces STS scholarship demonstrating how ideas about social difference (e.g., race, gender) are built into and reproduced through scientific knowledge and technologies.
Building Equitable and Inclusive Institutions & Lab Groups	This module offers an overview of principles from DEI scholarship on meaningful equity and inclusion practices tailored to the laboratory space.
Community Building Module	
STEM in the Spotlight	In this module, lab members select an underrepresented STEM figure that is meaningful to them and talk about their stories and the impact the figure has had on them.
DEI at Our Institution	This module encourages lab members to find out about ongoing DEI efforts at the lab's institution. Lab members share information on the goals of efforts happening at the university to increase awareness and spark discussion about their strengths and weaknesses.
Creating an Inclusive Lab Culture	This module creates space for the lab to talk as a group about how to implement some of the practices presented throughout the DE-SILO project in their lab (e.g., crafting a diversity and inclusion statement, creating a plan for sustained DEI engagement, and/or a discussion of lab culture and climate).

Table 3.5.2 Lab Characteristics

Table 2: Lab Characteristics

Lab	Field (general)	Number of Lab Group Members	Previous DEI Experience
Lab 1	Immunology	8-10	Yes
Lab 2	Molecular and Cell Biology /Neurobiology	8-10	Yes
Lab 3	Neurobiology	10-12	Yes
Lab 4	Molecular and Cell Biology	8-10	Yes

i The DEI label carries a number of variations. For instance, some refer to EDI, placing equity first. Others explicitly bring Anti-Racism into title as Inclusion, Diversity, Equity, and Anti-Racism (IDEA).

ii This is compounded by upward trends in worker burnout that were exacerbated during the COVID-19 pandemic. In recent years, STEM researchers, and doctoral students, postdoctoral, scholars, and early career researchers in particular, have documented increasing precarity, burnout, frustrations with work-life balance, and dissatisfaction with their careers and that institutional culture (18,20-22).

iii In future iterations, this will be a living document that group members can contribute to so that resources specific to fields are available.

iv Overall, this was a major limitation of the pilot study. Many lab group members did not complete module completion surveys after the first module was launched. We had a low response rate (5%), which hindered our understanding of how group members were responding to each individual module. In the future, incentives for module completion should be considered.

v In psychological research, habit formation is critical to the long-term adoption of specific behaviours. This has been taken up in health research broadly to encourage healthy dietary and physical activity. As a group we discussed at length why DEI conversations in scientific spaces felt difficult, and facilitators agreed that this was largely because it was not “normal” practice. Thus, we felt changing this—that is, making these conversations routine and habitual—would help to normalize them, and also to be seen not as “other” topics, but rather a routine part of scientific work.

3.6 REFERENCES

1. Hofstra B, Kulkarni VV, Galvez SM-N, et al. (2020) The diversity–innovation paradox in science. *Proceedings of the National Academy of Sciences* 117(17): 9284-9291.
2. AlShebli BK, Rahwan T and Woon WL (2018) The preeminence of ethnic diversity in scientific collaboration. *Nature communications* 9(1): 1-10.
3. McGee EO (2021) *Black, brown, bruised: How racialized STEM education stifles innovation*. Harvard Education Press.
4. Hoppe TA, Litovitz A, Willis KA, et al. (2019) Topic choice contributes to the lower rate of NIH awards to African-American/black scientists. *Science Advances* 5(10): eaaw7238.
5. Jimenez MF, Lavery TM, Bombaci SP, et al. (2019) Underrepresented faculty play a disproportionate role in advancing diversity and inclusion. *Nature ecology & evolution* 3(7): 1030-1033.
6. Eaton AA, Saunders JF, Jacobson RK, et al. (2020) How gender and race stereotypes impact the advancement of scholars in STEM: Professors' biased evaluations of physics and biology post-doctoral candidates. *Sex Roles* 82(3): 127-141.
7. Barber PH, Hayes TB, Johnson TL, et al. (2020) Systemic racism in higher education. *Science (New York, N.Y.)* 369(6510): 1440-1441.
8. Howard Hughes Medical Institute (2021) HHMI Launches \$2 Billion, 10-Year Investment

to Advance Diversity and Inclusion in Science.

9. Nunes L (2021) New Directions for Diversity, Equity, and Inclusion in Higher Education. Available at: <https://www.psychologicalscience.org/observer/words-to-action>.
10. Odekunle EA (2020) Dismantling systemic racism in science. *Science* (New York, N.Y.) 369(6505): 780-781.
11. Thorp HH (2020) Time to look in the mirror. *American Association for the Advancement of Science*, 1161-1161.
12. Ahmad A (2020) Equity in 2020 Requires More Than a Diversity Statement. Available at: <https://www.chronicle.com/article/equity-in-2020-requires-more-than-a-diversity-statement>.
13. Global Industry Analysts (2023) Global Diversity and inclusion (D&I) Industry. Reportno. Report Number|, Date. Place Published|: Institution|.
14. Ahmed S (2012) *On being included: Racism and diversity in institutional life*. Duke University Press.
15. Berrey E (2015) *The enigma of diversity: The language of race and the limits of racial justice*. University of Chicago Press.
16. Bowman Williams J and Cox JM (2022) *The New Principle-Practice Gap: The*

Disconnect between Diversity Beliefs and Actions in the Workplace. *Sociology of Race and Ethnicity* 8(2): 301-314.

17. Bell JM and Hartmann D (2007) Diversity in everyday discourse: The cultural ambiguities and consequences of “happy talk”. *American sociological review* 72(6): 895-914.

18. Jeske M (2022) Science Estranged: Power and Inequity in Laboratory Life during the COVID-19 Pandemic. *Science, Technology, & Human Values*. 01622439221117343.

19. Posselt JR (2020) Equity in science: Representation, culture, and the dynamics of change in graduate education. Stanford University Press.

20. Woolston C (2017) Graduate survey: A love–hurt relationship. *Nature* 550(7677): 549-552.

21. Woolston C (2020) Signs of depression and anxiety soar among US graduate students during pandemic. *Nature*. 147-148.

22. Woolston C (2022) Lab leaders wrestle with paucity of postdocs. *Nature*.

CHAPTER 4: Conclusions, Perspectives, and Future Directions

4.1 CONCLUSIONS, PERSPECTIVES, AND FUTURE DIRECTIONS

Throughout this dissertation, we examined and investigated asymmetric cell division (ACD) in the context radial glia progenitors (RGPs), which are principal neural stem cells, and explored the role of the evolutionarily conserved protein, Par-3, in regulating ACD process during active neurogenesis in the developing forebrain. Chapters 1 and 2 provided foundational insights into leveraging the zebrafish model to uncover neurobiological mechanisms, while also presenting compelling evidence regarding the multifaceted regulation, phosphorylation, and distribution of Par-3 in RGPs. In Chapter 3, we shifted focus to discuss the DEI project, DE-SILO, detailing our pilot experiment and its potential to revolutionize academic discourse by integrating DEI discussions into laboratory settings.

In Chapter 1, we employed an *in vivo* time-lapse imaging technique to reveal the heterogeneity within the RGPs population during active neurogenesis. However, a consistent convergent movement of Dld endosomes towards the posterior (subsequently basal) Notch^{hi} daughter during ACD was observed. This polarized endosome segregation critically relied on the activity of Par-3 and the dynein motor complex. Additionally, utilizing label retention expansion microscopy (LR-ExM), a novel methodology overcoming the limitations of signal loss in traditional ExM, we unexpectedly identified cytoplasmic Par-3. This cytoplasmic Par-3 was found to colocalize and be essential for mediating the association of dynein light intermediate chain 1 (Dlic1) with Dld endosomes. *In vivo* coimmunoprecipitation demonstrated the formation of protein complexes involving Par-3, Dld, and Dlic1. These findings collectively unveil the presence of cytoplasmic Par-3 and its direct involvement in localizing intracellular determinants. These exciting findings pave the way for uncovering new mechanisms underlying how cell polarity regulates ACD, particularly elucidating the roles of cortical Par-3 and cytoplasmic Par-3 in facilitating ACD within RGPs.

In Chapter 2, we delve into the dynamic relationship between cortical-Par-3 and cytoplasmic-Par-3. Utilizing in vivo time lapse imaging, we demonstrate evidence for a deployment of Par-3 from the cortex to the cytoplasm. We investigated the role of two conserved serine residues in Par-3, focusing on Ser-227 and Ser-954, potential phosphorylation sites of Aurora Kinase A (AurkA). Mutation of Ser-954, but not Ser-227, to phospho-incapable Alanine significantly disrupted embryonic brain development and suppressed neurogenesis when expressed in one-cell stage embryos. Expression of the mutated Par-3S954A in later-stage embryos led to reduced cytoplasmic Par-3, increased cortical Par-3, disturbed Par-3 cortical asymmetry, and interference with Dld distribution in mitotic RGPs. In vitro experiments confirmed AurkA's direct phosphorylation of Par-3 at serine-954. Additionally, in vivo time-lapse imaging revealed a transient interaction between AurkA and cortical Par-3, influencing Par-3 cortical asymmetry directionality. AurkA overexpression increased Par-3 cytoplasmic presence and disrupted cortical asymmetry in mitotic RGPs. Overall, our findings highlight AurkA's role in phosphorylating Par-3, thus regulating its cytoplasmic-cortical dynamics and impacting neural progenitor fate during neurogenesis. These results offer insights into the molecular mechanisms governing asymmetric cell division and neurodevelopment. Future in vivo studies will be needed to understand the complexity of the phosphorylation mechanism between Par-3 and AurkA and how that facilitates ACD in RGPs.

In Chapter 3, we narrowed in on the importance of diversity in scientific innovation, with underrepresented researchers often producing more novel research and innovative solutions. However, systemic racial and ethnic stratification within academic science persists, hindering the advancement of underrepresented researchers. These disparities exist at all levels of scientific training, affecting early career researchers who often face undervalued service work and earn less than their white counterparts. The events of 2020 prompted widespread discussions on systemic racism and diversity, equity, and inclusion (DEI) programming within

academic science. While DEI initiatives have become ubiquitous, their effectiveness in creating meaningful change remains uncertain. Societal norms often marginalize social concerns within scientific settings, complicating efforts to address issues of diversity and inclusion. In response to these challenges, The DE-SILO Project was developed to facilitate sustained engagement with discussions of racism, diversity, and inclusion in laboratory settings. The DE-SILO Project aims to address longstanding disparities and institutional harms within academic science by fostering sustained engagement with issues of diversity, equity, and inclusion. Through piloting the project in four research-intensive institutions, valuable insights have been gained regarding implementation challenges and strategies for facilitating meaningful dialogue. Moving forward, continued efforts are needed to integrate discussions of racism, diversity, and inclusion into everyday scientific practice, ensuring that underrepresented researchers are valued and supported within the scientific community.

In conclusion, this dissertation aims to shed light on the role of cell polarity during ACD in RGP. As we have shown, experiments in zebrafish are an excellent strategy for addressing this, and from our work comes several new findings that be used to explore further mechanistic properties within ACD during active neurogenesis. Moreover, these findings provide evidence that can point to how is initial polarity established, which remains largely unknown. We advocate for the utilization of our published work and techniques to bridge the gaps in our understanding of cell polarity and ACD, thereby advancing our comprehension of the fundamental regulation of neurogenesis.

Publishing Agreement

It is the policy of the University to encourage open access and broad distribution of all theses, dissertations, and manuscripts. The Graduate Division will facilitate the distribution of UCSF theses, dissertations, and manuscripts to the UCSF Library for open access and distribution. UCSF will make such theses, dissertations, and manuscripts accessible to the public and will take reasonable steps to preserve these works in perpetuity.

I hereby grant the non-exclusive, perpetual right to The Regents of the University of California to reproduce, publicly display, distribute, preserve, and publish copies of my thesis, dissertation, or manuscript in any form or media, now existing or later derived, including access online for teaching, research, and public service purposes.

DocuSigned by:

Jason Garcia

1FED70AEB2484CF...



Author Signature

5/21/2024

Date